MODELING AND MICROSCOPY STUDY OF YTTERBIUM-DOPED FIBERS

YTTERBIUM-DOPED FIBER AMPLIFIERS: COMPUTER MODELING OF AMPLIFIER SYSTEMS AND A PRELIMINARY ELETRON MICROSCOPY STUDY OF SINGLE YTTERBIUM ATOMS IN DOPED OPTICAL FIBERS

By

HAO LIU, B. Sc.

A Thesis

Submitted to the School of Graduate Studies

in Partial Fulfillment of the Requirements

for the Degree

Master of Applied Science

McMaster University

MASTER OF APPLIED SCIENCE (2011) (Engineering Physics)	McMaster Univeristy Hamilton, Ontario

TITLE:	Ytterbium-doped fiber amplifiers: Computer modeling of amplifier systems and a preliminary electron microscopy study of single ytterbium atoms in doped optical fibers
AUTHOR:	Hao Liu, B. Sc. (Sun Yat-sen University)
SUPERVISOR:	Dr. Harold K. Haugen
NUMBER OF PAGES:	xviii, 145

Abstract

Ytterbium-doped optical fibers have extensive applications in high-power fiber lasers, optical amplifiers, and amplified spontaneous emission light sources. In this thesis two sub-projects associated with ytterbium doped fibers are discussed.

Numerical simulations have been used to model high-repetition rate ultrafast ytterbium-doped fiber amplifier systems assuming continuous-wave input signals under variable situations, such as one-sided and two-sided pumping. Different system configurations are also developed, such as a single-stage amplification system, a two-stage amplification system and a separated amplification system, providing alternative choices for experiments and applications. The simulation results are compared with experimental data and the simulation results from some other software. The influence of nonlinear effects in the fiber is also very briefly discussed in this thesis.

In a second research activity, the distribution of ytterbium atoms is being investigated in a range of double-clad ytterbium-doped fibers. Using aberration-corrected electron microscopy, ytterbium atoms are directly observed from the wedge-shaped specimen, which was prepared from ytterbium-doped optical fibers by tripod polishing combined with ion milling. Challenges related to sample preparation and the interpretations of images are discussed, but the approach shows great potential to investigate the doping behaviors down to atomic scale in the fibers. The work is expected to help reveal mechanisms affecting the performance for the doped fibers, such as photodarkening which is potentially associated with clustering effects.

Acknowledgements

I would first like to thank my supervisor, Dr. Harold K. Haugen. Two years ago, Harold offered me a chance to study at McMaster University as a graduate student. Since then, I went into the world of optical physics. In the past two years, he has endlessly supported me and wouldn't let me give up on myself. For that, I am forever grateful. I have learned a great deal from him about both research and life. His attention to detail and scientific rigor are examples for me to learn. I am also extremely grateful to Harold that he gave me opportunities to attend several conferences which significantly widen my vision. He is a man who changes my life.

I would like to thank the colleagues in my group. I would like to thank Dr. Ran An for his supports in both research and life. He performed as my second supervisor. I would like to thank Eugene Hsu for the endless help. He is always patient and passionate to answer any of my questions. I would like to thank Derek Goad and Andrew T. Walker who helped me to revise this thesis. I would like to thank Bing Liu and Jasper A. Z. Brawley-Hayes for their numerous useful suggestions to the research and this thesis.

I would like to thank Dr. Andrew Budz who has provided substantial advice and encouragement on my research. His generous sharing of his technical data and programming code helped me progress fast in the research work.

I would like to thank Mojtaba Hajialamdari from the group of Dr. Donna Strickland at the University of Waterloo for his help to benchmark my simulation results by using his simulator. I also appreciate him for the many hours of technical discussions and assistance.

I would like to thank CorActive Inc. They provided all the fibers for microscopy study.

I would like to thank the Canadian Centre for Electron Microscopy (CCEM) for their collaboration. I would like to thank Dr. Gianluigi Botton, Dr. Martin Couillard, Julia Huang and Dr. Nicolas Gauquelin for their collaboration and advice. Wenhe Gong from the Brockhouse Institute for Materials Research is gratefully acknowledged for his assistance and the supervision which he provided on the preparation of the optical fiber samples for electron microscopy via the tripod polishing and ion milling technique. I would like to thank Guozhen Zhu for her help in revising my thesis.

I would like to thank Doris Stevanovic for her help in etching fibers with Hydrogen Fluoride (HF).

I would like to thank the Canadian Institute for Photonics Innovations (CIPI) and the Natural Sciences and Engineering Research Council of Canada (NSERC), for their funding support to the research.

I would also like to thank someone very special in my life, my fiancée, Yin Zhen. She has always supported me in all my endeavors. She is accompanies me in this country far away from home and gives me hopes of the future.

Finally, I would like to thank my parents, for their unconditional, selfless love and support. At any time, they always try their best to support my study. It is hard to express my appreciation to them, but I know my achievement to this degree is the best reward to them.

Contents

List of Figures

List of Tables

Chapter 1 Introduction

Ytterbium-doped fiber amplifiers (YDFAs) have a wide variety of experimental and industrial applications. Studies about YDFAs are numerous; however, two aspects of YDFAs are focused on in this thesis: the development of YDFA systems for certain applications through the simulation of dual-wavelength amplification systems and an important problem known as the photodarkening effect that occurs during the utilization of YDFAs. Although only preliminary work has been done in this thesis, some unique ideas are shown and it could be a reference for future work.

1.1 Outline

This section overviews the main ideas of each chapter of this thesis.

Chapter 1 states the literature review of the projects in this thesis, including the dual-wavelength ytterbium-doped fiber amplifier system and the electron microscopy study of single ytterbium atoms in doped fibers. Finally, this section explains the motivation behind this thesis.

Chapter 2 explains the background knowledge which is required to understand the thesis. The properties of double-clad ytterbium-doped fibers and different explanations of the mechanism behind the photodarkening effect are also discussed. Finally, the equipment used for preparing transmission electron microscopy (TEM) specimens is also introduced in detail.

Chapter 3 discusses the simulation results under different conditions and configurations. Some new uses of the prototype model to our group, such as amplification of beams of different wavelengths and the product of the powers of the two output seed beams, are developed. Some system models, such as a two-fiber amplification system and a two-stage amplification system, are discussed in detail. Finally, the thresholds of some nonlinear effects are also discussed.

Chapter 4 discusses the transmission electron microscope characterizations of ytterbium-doped optical fibers. Three different methods were attempted to reach the core of the fiber and the results of the electron microscopy studies are demonstrated in detail. Factors which may cause some inaccuracies and can be improved are also discussed.

Chapter 5 summarizes the entire work as well as discusses some future prospects which could prove valuable.

1.2 Dual-Wavelength System

The first topic of this thesis is the dual-wavelength ytterbium-doped fiber amplifier system. Dual-wavelength ultrafast optical sources with picosecond or shorter pulses could have many applications such as generating high-repetition-rate mid-infrared radiation (MIR) by difference-frequency mixing (DFM) or for two-color pump-probe experiments. The simulation scenarios for this thesis are based on semiconductor-based ultrashort-pulse lasers as seed beams, which are different from conventional ultrafast systems typically based on solid-state crystal lasers. The semiconductor-based ultrashort-pulse lasers are more attractive than conventional sources due to their higher efficiency, much lower cost, compactness and better reliability. However, the typical average output power of a short-pulse semiconductor laser is only a few milliwatts. Therefore, the semiconductor seed beam system usually needs an external amplification system. Some work involving YDFAs for developing dual-wavelength amplification systems has been reported. Hajialamdari *et al.* have recently demonstrated a dual-wavelength two stage YDFA system seeded with a two-color spectrum centered at 1035 nm and 1105 nm, in which a single-clad, single-mode YDFA is used as a preamplifier and a double-clad single-mode YDFA is used as a power amplifier [1]. Al-Kadry *et al.* showed a two-stage YDFA system to amplify signals at 1038 and 1105 nm, which is used to generate a 17.5 μm output signal by DFM [2]. Goldberg *et al.* utilized continuous-wave (CW) diode lasers and amplifiers constructed with double-cladding Yb-doped fiber followed by single-mode Er/Yb co-doped fiber, to generate signals at 1.1 μm and 1.5 μm, which are used to produce mid-infrared radiation near 3.5 μm by DFM [3]. Pan *et al.* demonstrated a high power passively Q-switched dual wavelength Yb fiber laser with two output wavelengths centered at 1040 nm and 1070 nm which are generated directly from the cladding pumped Yb doped fiber laser [4]. Romero-Alvarez *et al.* utilized a mode-locked Yb-doped fiber oscillator and a two-stage, two-color fiber amplifier to generate dual-wavelength signals for MIR by DFM [5]. D. Creeden *et al.* demonstrated the generation of a Terahertz source using DFM based on dual-wavelength amplification, in which separate YDFAs are used for pre-amplification and multistage large-mode-area YDFAs are used for power amplification [6]. In this thesis, based on the prototype experimental system which comes from Budz *et al*. [7], simulation work which acts as an extension of the prototype system is developed and a simulation of a two-stage dual-wavelength YDFA system is established in order to instruct future experimental work. This work was done under a CIPI project. This simulation work is also complementary to the experimental and computational efforts at the University of Waterloo. The work in Waterloo is aimed at the goal of mid-infrared generation using ultrashort light pulses.

1.3 Photodarkening

The second topic of this thesis is the study of the photodarkening effect in doped optical fibers. YDFAs have been increasingly used to amplify high-repetition-rate short laser pulses, due to their high efficiency and high output powers. However, along with an increase in output power, a phenomenon called the photodarkening effect restrains the high efficiency of YDFAs in situations of long term deployment. Photodarkening refers to the transmission losses resulting from absorption or scattering increasing with time [8]. It is believed that the origin of the photodarkening effect in Yb-doped fibers is due to the formation of color centers [9] [10] [11] [12]. There are a variety of factors reported that contribute to the formation of color center will be discussed in chapter 2. Photodarkening can lead to degradation in performance and lifetime limitation in the practical application of YDFAs. Although the mechanism behind photodarkening has not been fully understood yet, it has been shown to be partially and fully reversible in certain circumstances [9] [12]. Fully understanding the mechanism can help to further mitigate or perhaps even eliminate photodarkening in optical devices. Determination of the distribution of ytterbium ions in YDFAs can be important to help understand the mechanism of photodarkening. This thesis will introduce a preliminary electron microscopy study of single ytterbium atoms in doped optical fibers, which for the first time observes the distribution of ytterbium atoms directly. The following chapter will introduce some different theories published in papers which explain the mechanism of photodarkening in YDFAs from different aspects. This work of the present thesis was done under a CIPI project. It was stimulated by previous experimental work in our group on Yb-fiber amplifiers where some fibers were observed to suffer from severe photodarkening issues. It was realized that the world class facilities of the CCEM might offer a means for unique investigations of the Yb-doped fibers.

Chapter 2 Background

This chapter provides an overview of the background material about the ytterbium-doped fiber dual-wavelength amplifier system and the electron microscopy study of single ytterbium atoms in doped optical fiber. The first part of this chapter introduces basic concepts of ytterbium doped fibers. The spectral properties of Yb-doped fibers will also be discussed in detail. The second part of this chapter discusses some mechanisms which have already been published to explain the photodarkening effect. The equipment involved in sample preparation and characterization is also introduced.

2.1 External-Cavity Mode-Locked Semiconductor Lasers

As mentioned in Chapter 1, the configuration of the simulation work is based on the previous experimental work which was done by Andrew Budz [7]. The laser sources adopted in Andrew's model are external-cavity mode-locked semiconductor lasers and they are also the basis for all the simulation work in this thesis.

Figure 2-1 shows the schematic of a basic external-cavity mode-locked diode laser. The major components are a contacted absorber, a gain diode chip, two lenses and an external feedback element. By changing the external cavity length, the round-trip time is changed and then one can control the pulse repetition rate. If a diffraction grating is applied as a feedback element, one can control the operating wavelength by rotating the grating.

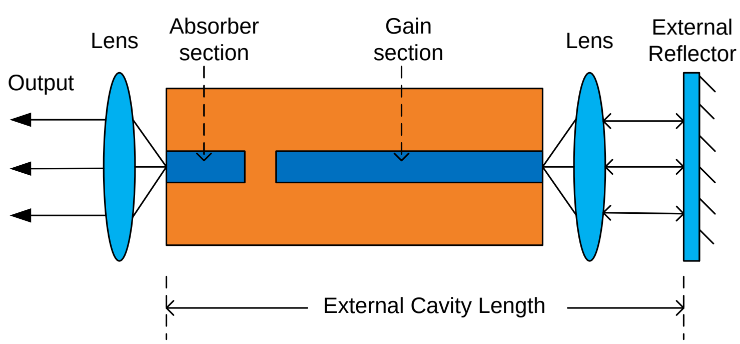

Figure 2-1 Schematic of a basic external-cavity mode-locked laser

The two mode-locked external-cavity semiconductor lasers used in the following simulation work operate at the centre wavelengths of 1040 nm and 1079 nm, with a repetition rate of 577 MHz [7], which can be considered as continuous-wave (CW) diode lasers in the simulation. The period between pulses is much smaller than the excited-state life time, so the pulse train can also be considered as a quasi-CW signal inside the amplifier.

2.2 Yb-Doped Fiber Amplifiers

The ytterbium-doped fiber is a pivotal component in a dual-wavelength amplification system in this thesis. The Yb-doped fiber provides amplification over a very broad wavelength range from ~975 to ~1200 nm and also offers high output power and excellent power conversion efficiency [13]. In this section, the properties of ytterbium-doped fibers will be discussed. The simulation model used in this thesis will be introduced to show the calculation of gain and ASE for active fibers.

2.2.1 Doped Fiber Amplifier

Doped fiber amplifiers (DFAs) are optical amplifiers where a doped optical fiber is used as a gain medium to amplify an optical signal. The mechanism of signal gain is similar to ordinary lasers. The pump light couples into the doped fiber, and then the dopant ions can be pumped from ground states to excited states. The propagating signal power in a doped-fiber amplifier can interact with the excited ions and then be coherently amplified by stimulated emission. The excited ions can also decay spontaneously (spontaneous emission) or through nonradiative processes which release phonons. These two effects reduce the efficiency of DFAs. The spontaneous emission is the main source of the background noise and will be discussed in detail in the following section.

An amplification window is an important property of DFAs. It is the range of optical wavelengths in which the amplifier can yield a usable gain. For example, erbium-doped fiber amplifiers (EDFAs) have two amplification windows, Conventional band (C-band) from 1525 to 1565 nm and Long band (L-band) from 1570 to 1610 nm [14]. The amplification window for ytterbium-doped fiber amplifiers (YDFAs) is from 975 to 1200 nm [13]. The amplification window is mainly determined by the spectroscopic properties of the dopant ions. The spectroscopic properties of ytterbium will be discussed in the following sections.

2.2.2 Amplified Spontaneous Emission (ASE)

Amplified spontaneous emission (ASE) is the dominant noise in optical fiber amplifiers which is generated by the spontaneous de-excitation of the active ions [15]. When population inversion occurs, some of the excited electrons will spontaneously return to the ground state by emitting photons which have no coherence characteristics. This process leads to a broad spectral background of photons that become amplified along with the optical signal. The spontaneous noise can be modeled as infinite short pulses distributed along the fiber, and the noise power spectrum should be flat with frequency.

The number of randomly polarized photons is given by the following equation (2-1) [16]

$$dn(\nu) = A_{21} g(\nu)\delta(\nu)\frac{\Delta\Omega}{4\pi} dV \int_s N_2(r,\theta)\bar{\psi}_s(r,\theta) r\, dr\, d\theta \qquad (2\text{-}1)$$

dn(v) is the number of photons generated at frequencies between *v* and $v+\delta v$ in the direction of positive z in an infinitesimal volume *dV*. *g(v)* is the lineshape function, which is defined as $g(v)=8\pi n^2\tau\sigma_e(v)/\lambda_s^2$, where *n* is the medium refractive index, τ is the excited state life time, $\sigma_e(v)$ is the emission cross section at frequency ν, λ_s is the wavelength. $A_{21}=1/\tau$ is the rate of spontaneous decay. $\Delta\Omega/4\pi$ is the ratio of spontaneous emission photons captured by the fiber, where the capture solid angle $\Delta\Omega= \lambda_s^2/n^2\pi\omega_s^2$ and the volume element $dV= \pi\omega_s^2 dz$. The integral term stands for the overlap between the density distribution of excited ions and the guided mode. N_2 is the excited state populations, $\psi_s(r,\theta)$ is the mode envelope, where (r,θ) represent the cylindrical transverse coordinates (*z* is the fiber longitudinal coordinate). The corresponding spontaneous emission power per unit frequency can be obtained by $dP_{SE}=hvdn(v)$. Therefore, the rate of creation of spontaneous emission power in bandwidth δv is given by [16]

$$\frac{dP_{SE}}{dz} = 2P_0\sigma_e(\nu)\int_s N_2(r,\theta)\bar{\psi}_s(r,\theta) r\, dr\, d\theta \qquad (2\text{-}2)$$

$P_0 =hvdn(v)$ is defined as the power of one spontaneous noise photon in bandwidth δv. In high gain conditions, the total ASE equals the amplification of one hypothetical input photon per mode in bandwidth δv along the fiber. Thus the term P_0 is usually called equivalent input noise.

The optical noise of fiber, amplified spontaneous emission (ASE), is generated along the fiber as long as population inversion exists, whether optical signals are input to the fiber or not. There is also counter-directional ASE generated in the fiber propagating opposite to the signal. The ASE propagating along the direction of positive z is referred to as forward ASE. Similarly, the ASE propagating along the direction of negative z is referred to as backward ASE.

2.2.3 Spectroscopic Properties of Yb-doped Fiber

The spectroscopy of Yb^{3+} is simple compared to some other rare-earth (RE) ions. Figure 2-2 shows the energy level structure of Yb^{3+} in silica glass. There are only two manifolds relevant to optical wavelengths: the $^2F_{7/2}$ ground-state

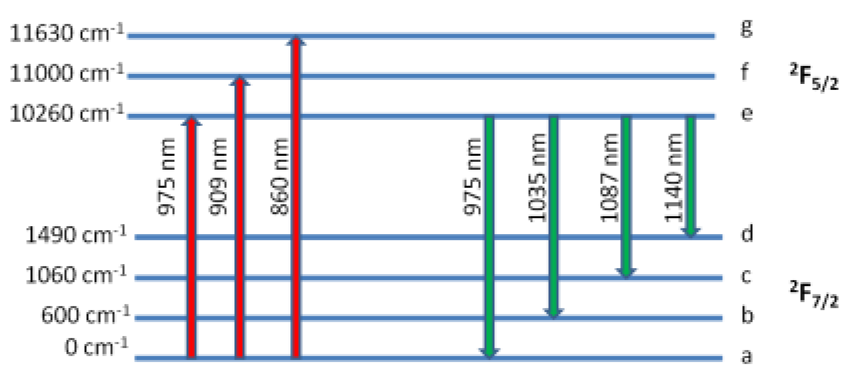

Figure 2-2 Energy level structure of Yb^{3+} [17]

manifold consisting of 4 sublevels and the $^2F_{5/2}$ excited-state manifold consisting of 3 sublevels [17].

Figure 2-3 shows the absorption and emission cross-sections of Yb^{3+} in a germanosilicate glass. There are two absorption peaks, at wavelengths of 910 nm and 975 nm, and two emission peaks, at wavelengths of 975 nm and 1030 nm. The pump wavelength should be located at the absorption peak and the amplification wavelength should be in the range of emission peaks.

The first absorption peak is located at 910 nm. It results from the transition from the lowest sublevel in the ground state, level a, to the second sublevel in the excited state, level f. Since the excited ions at level f are not stable and easily

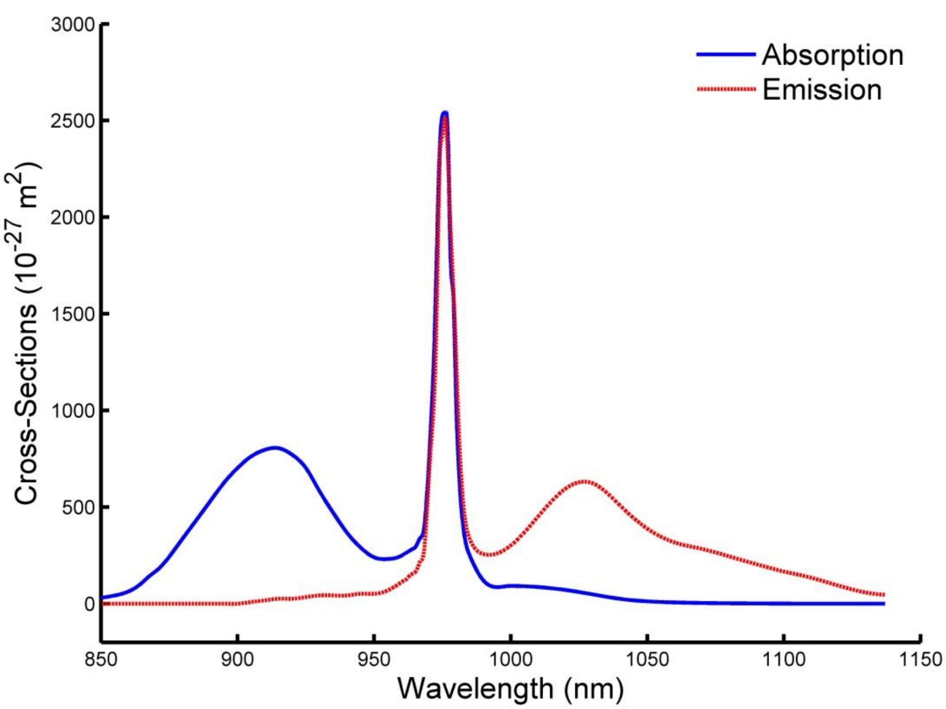

Figure 2-3 Absorption (blue) and emission (red) cross sections of Yb in germanosilicate galss [13]

decay to level e in the excited state manifold, the emission cross-section at a wavelength of 910 nm is very small. Thus it allows a substantial Yb population to be excited to the upper manifold and strong pumping at 910 nm leads to 97% upper-state population which leads to nearly the maximum possible gain per unit length [13]. The first emission cross-section peak is at 975 nm which results from the transitions from the lowest sublevel in excited state, level e, to the lowest sublevel in ground state, level a. So a very high gain can be achieved at 975 nm with pumping around 910 nm. However, the narrow amplification bandwidth around 975 nm limits the potential applications.

It is also possible to achieve amplification from 1000 to 1150 nm with a pump wavelength around 910 nm. The second emission cross-section peak with a long emission tail, results from transitions from the lowest sublevel in the excited manifold to the sublevels b,c,d of the ground manifold (Figure 2-2). Although pumping at 910 nm allows for a high population inversion, the gain at 975 nm is very strong. It means that under pumping at 910 nm, ASE around 975 nm is an issue which could reduce the efficiency significantly. One way to avoid this negative effect is to apply a double-pass configuration, in which the signal reflects back after the first pass but not the ASE. In this way, the signal could be amplified twice compared with a single-pass configuration [13]. The other way is to use another kind of doped fiber which can absorb at a wavelength of 975 nm to suppress the gain of ASE. Er-doped silica fibers happen to have an absorption peak at 975 nm and thus the problem can be solved by combining several pieces of Yb-doped fiber and Er-doped fiber together [13].

The most efficient way to get amplification between 1000 and 1150 nm, which correspond to transitions from level e in the excited state manifold to levels b and c in the ground state manifold, is to utilize pumping at 975 nm. A pump wavelength of 975 nm corresponds to the second absorption peak, which results from the transition from the lowest sublevel in the ground state, level a, to the lowest sublevel in excited state, level e. Levels a and e are lowest sublevels in their manifold, which results in a strong peak for both absorption and emission cross-section with almost the same amplitude. Thus, the upper state population could be 50% at most [13]. Since the absorption cross-section peak at 975 nm is relatively narrow, the spectra of the pump laser output pulses must be narrow.

The host glass composition also has an affect on the properties of the Yb^{3+} absorption and emission spectra [18] [19]. Co-dopants in the core of Yb-doped germanosilicate fibers, such as aluminum, germanium, and boron, can change the characteristics of the transition cross-sections by as much as 30% by modifying the concentration of co-dopants in the core, especially in the range of 990-1020 nm [13]. The fluorescence lifetime can also vary by around 30% due to the composition of the host glass. The typical fluorescence decay time is around 0.8 ms while Yb in a pure silicate glass or some phosphosilicate glass has a lifetime of around 1.5 ms.

The simple level structure of ytterbium significantly minimizes several undesirable effects such as excited state absorption and concentration quenching, which usually exist in other RE-doped fibers and reduce the efficiency of the gain medium [20]. Both of the effects are caused by energy transfer upconversion (ETU), a physical principle in which the excited active ions in the gain medium reach a higher energy level which is above the level achieved by simple absorption of the pump photons [8]. Excited state absorption indicates a single active ion makes a transition to a higher level. Concentration quenching is an ETU effect that occurs because of a clustering of ions within the host medium. Both of them are observed in Er-doped fibers [21]. Since the two-manifold structure prevents the ETU from occurring, the state absorption and concentration quenching are absent in Yb-doped fibers and thus a high doping density in the core is possible. High doping levels enable large unsaturated gains in short fiber length.

2.2.4 Double-clad Fiber Amplifiers

The fiber lasers and amplifiers which are based on single-clad single-mode doped fibers can produce diffraction-limited outputs. However, the pump sources in this system also need to achieve diffraction-limited beam quality to match the geometric size of the fiber core. It thus restricts the power of the pump beam to a low value since the high power beam focused on a small core area has an extremely high intensity and will likely damage the facet of the fiber. On the other hand, if multimode fibers are adopted, it usually (although not always) results in poor beam quality. The invention of double-clad fiber helps to solve this problem.

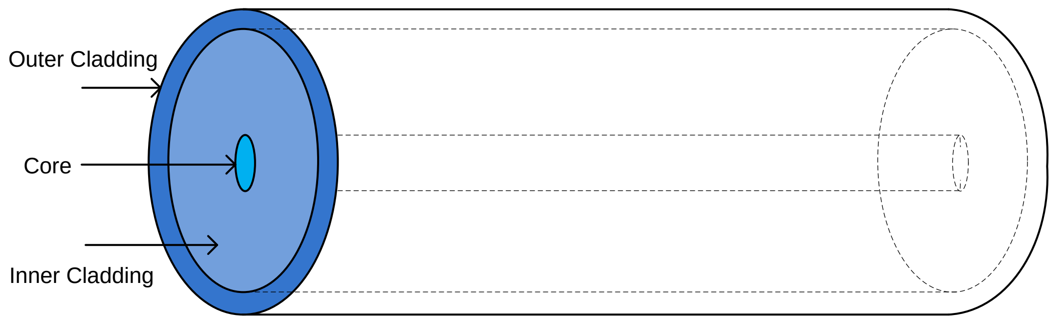

Figure 2-4 Schematic drawing of double-clad fiber

Figure 2-4 shows a schematic of a double-clad fiber, which includes an extra layer of cladding (outer cladding) outside of the inner cladding. A double-clad fiber amplifier refers to a double-clad fiber with a doped core. The signal light is coupled into and then amplified in the core of the fiber, while the pump light is launched into the inner cladding. In any given plane which is perpendicular to the direction of light propagation, only a small fraction of the pump light interacts with the dopant ions in the fiber core. The ratio *D* indicates the percentage of pump energy launched into the inner cladding that is actually used for amplification at a given position of the fiber. A_{core} is the area of the fiber core and $A_{inner\ cladding}$ is the area of inner cladding.

$$D = \frac{A_{core}}{A_{inner\ cladding}} \tag{2-3}$$

Usually, the diameter of inner cladding is greater than a hundred micrometers while the diameter of core is only a few micrometers. Thus the ratio D is very small. To get a higher effective pump power, one can largely increase the pump power launched into the inner cladding. The ratio D can be slightly changed by applying different shapes of inner cladding to increase the chance that the reflected pump light goes across the core. Figure 2-5 shows double-clad fibers with octagonal and D-shaped inner cladding. These kinds of double-clad fibers with irregular inner cladding shapes are usually called "chaotic fibers". The irregular inner cladding shapes enable the pump light to reflect in random

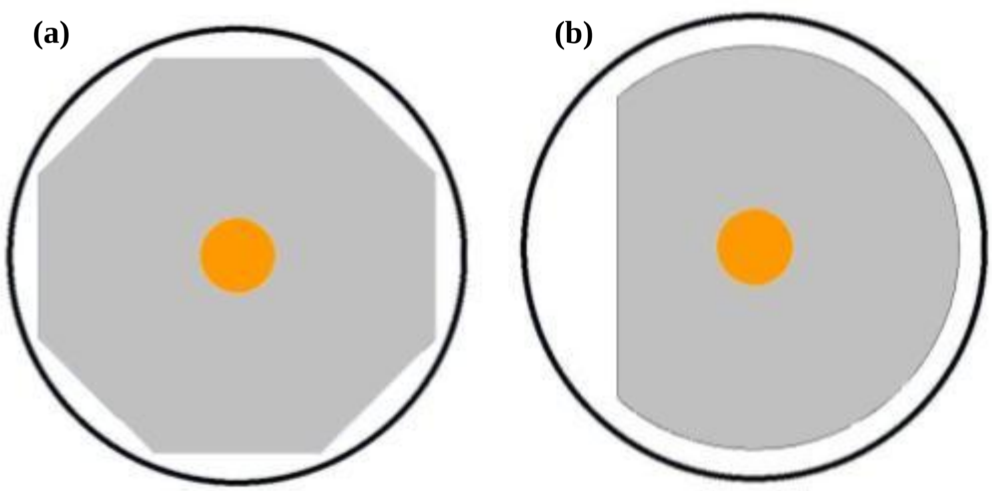

Figure 2-5 Cross-section of (a) Octagonal and (b) D-shaped double-clad fiber

directions and thus the pump light would have a greater possibility to go through the core and excite the dopant ions.

The amplified signals which are confined to the small core area could exhibit some nonlinear effects due to their high intensity. One method to reduce the nonlinear effects is increasing the core area, which can decrease the intensity of the amplified signal. Such fibers with a greater core area are called large-mode-area (LMA) fibers with typical diameters of 20 μm or more. The threshold of some nonlinear effects will be discussed in Chapter 3.

2.2.5 Rate Equations of Yb ions

Assuming that the power of a beam is P [W] in a doped fiber amplifier core, the concentrations of dopants in the ground and excited states are N_1 and N_2 [m^{-3}], and the emission and absorption cross-sections are σ_e and σ_a [m^2] respectively. When the beam with power P travels through the active medium, the amount of power absorbed by ground state atoms (which pumps them to excited states) per unit length is $\sigma_a \times P \times N_1$ [W/m], and the gain of the power per unit length is $\sigma_e \times P \times N_2$ [W/m]. In a infinitesimal distance dz, if we only consider the stimulated emission and absorption contribution, the expected change of the power should follow the equation

$$P_{x+1} = P_x + (\sigma_e N_2 - \sigma_a N_1) \times P \times dz \tag{2-4}$$

If ASE does not extract significant power, the spatially-dependent population and power-propagation rate equations are relatively simple, given by [22]

$$\begin{aligned}\frac{dN_2}{dt} = \frac{D}{hcA}\sum_{j=1}^{J}\lambda_j^p[\sigma_a(\lambda_j^p)N_1 - \sigma_e(\lambda_j^p)N_2] \times P_p(\lambda_j^p) \\ + \frac{\Gamma}{hcA}\sum_{k=1}^{K}\lambda_k^s[\sigma_a(\lambda_k^s)N_1 - \sigma_e(\lambda_k^s)N_2] \times P_s^{\pm}(\lambda_k^s) \\ - \frac{N_2}{\tau}\end{aligned} \tag{2-5}$$

$$N_1 = N_T - N_2 \tag{2-6}$$

$$\frac{dP_p(\lambda_j^p)}{dz} = D[\sigma_e(\lambda_j^p)N_2 - \sigma_a(\lambda_j^p)N_1]P_p(\lambda_j^p) - \alpha P_p(\lambda_j^p) \tag{2-7}$$

$$\frac{dP_s^{\pm}(\lambda_k^s)}{dz} = \Gamma[\sigma_e(\lambda_k^s)N_2 - \sigma_a(\lambda_k^s)N_1]P_s^{\pm}(\lambda_k^s) - \alpha P_s^{\pm}(\lambda_k^s) \tag{2-8}$$

where N_T is ytterbium doping density. The pump and signal powers are divided into separate spectral channels. $P_p(\lambda_j^p)$ is the pump power of the *j*th pump channel. $P_s^+(\lambda_k^s)$ or $P_s^-(\lambda_k^s)$ are the signal power of *k*th signal channel propagating forward or backward with respect to the pump beam. c is the speed of light in vacuum, α is the background attenuation coefficient of the fiber, τ is the florescence lifetime of the upper laser level, A is the doped effective area of the fiber, D and Γ are confinement factors of the pump and signal beams in the doped area. Equation (2-5) shows the changes of upper population density due to stimulated absorption and emission of both the pump and signal beams. Equations (2-7) and (2-8) show the evolution of pump and signal power along the fiber.

There are some simplifying assumptions used in the rate equations. The gain medium is assumed to be homogeneous, the pump and signal intensity profile over the area of inner cladding and core area are assumed to be uniform. The ytterbium population density is assumed to be uniformly distributed in the core area.

If the effect of ASE is included into the rate equations, the spatially-dependent population and power-propagation rate equations are relatively simple, given by [7]

$$\begin{aligned}\frac{dN_2}{dt} = \frac{D}{hcA}\sum_{j=1}^{J}\lambda_j^p[\sigma_a(\lambda_j^p)N_1 - \sigma_e(\lambda_j^p)N_2]\times P_p(\lambda_j^p) \\ + \frac{\Gamma}{hcA}\sum_{k=1}^{K}\lambda_k^s[\sigma_a(\lambda_k^s)N_1 - \sigma_e(\lambda_k^s)N_2]\times P_s^{\pm}(\lambda_k^s) \\ + \frac{\Gamma}{hcA}\sum_{l=1}^{L}\lambda_l^{ASE}[\sigma_a(\lambda_l^{ASE})N_1 - \sigma_e(\lambda_l^{ASE})N_2] \\ \times[P_{ASE}^{+}(\lambda_l^{ASE}) + P_{ASE}^{-}(\lambda_l^{ASE})] - \frac{N_2}{\tau}\end{aligned} \tag{2-9}$$

$$N_1 = N_T - N_2 \tag{2-10}$$

$$\frac{dP_p(\lambda_j^p)}{dz} = D[\sigma_e(\lambda_j^p)N_2 - \sigma_a(\lambda_j^p)N_1]P_p(\lambda_j^p) - \alpha P_p(\lambda_j^p) \tag{2-11}$$

$$\frac{dP_s^{\pm}(\lambda_k^s)}{dz} = \Gamma[\sigma_e(\lambda_k^s)N_2 - \sigma_a(\lambda_k^s)N_1]P_s^{\pm}(\lambda_k^s) - \alpha P_s^{\pm}(\lambda_k^s) \tag{2-12}$$

$$\frac{dP_{ASE}^{\pm}(\lambda_l^{ASE})}{dz} = \Gamma[\sigma_e(\lambda_l^{ASE})N_2 - \sigma_a(\lambda_l^{ASE})N_1]P_{ASE}^{\pm}(\lambda_l^{ASE}) - \alpha P_{ASE}^{\pm}(\lambda_l^{ASE}) + \Gamma\sigma_e(\lambda_l^{ASE})N_2\frac{2hc^2\Delta\lambda}{[\lambda_l^{ASE}]^3} \tag{2-13}$$

where $P^{+}_{ASE}\ (\lambda_l^{ASE})$ and $P^{-}_{ASE}\ (\lambda_l^{ASE})$ are the forward and backward ASE power of the lth ASE channel. $\Delta\lambda$ is the width between two ASE channels. Equation (2-9) which is modified from Equation (2-5) adds the changes in upper population density due to the stimulated absorption and emission of ASE. Equation (2-13) shows the evolution of ASE power along the fiber for both directions.

2.3 Experimental Setup

Previous experimental research on ytterbium-doped fiber amplification systems have been carried out in our lab by Andrew Budz as shown in Figure 2-6 [7]. The seed oscillators include two external-cavity, mode-locked semiconductor lasers. The tuning range is 1030-1090 nm and the minimum pulse width is about 1 ps. The pump laser operates at 975 nm and travels at counter-direction to the signal beams. Following the general approach of the existing experimental setup based on a single fiber amplifier, a dual-fiber amplifier system and a two-stage amplification system were simulated to find the optimal fiber lengths for future experimental work. Pumping from both ends is also applied in these simulation systems as well as the original pumping from one end. The details of these systems will be discussed in Chapter 3.

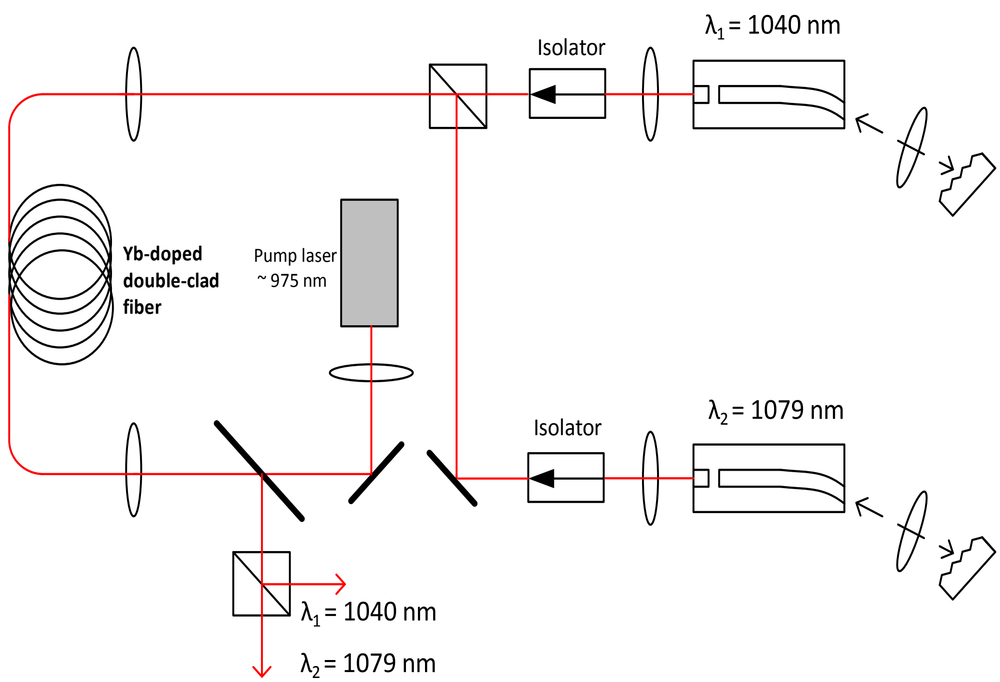

Figure 2-6 Experimental configuration used for dual-wavelength amplification of synchronized ultrashort laser pulses.

2.4 Numerical Modeling

Equations (2-9) to (2-13) can be numerically solved under steady-state conditions using the finite difference method. Figure 2-7 shows the schematic of the numerical modeling. The fiber is spatially divided into *n* segments. $N_1[n]$ and

$N_2[n]$ describe the population densities of the ground state manifold and the excited state manifold in the *n*th segment. $P[n]$ describes the power, including the pump, signal and ASE power, in the *n*th segment. The left end of the fiber is noted as $z=0$ and the right end of the fiber is $z=L$. L is the length of the entire fiber.

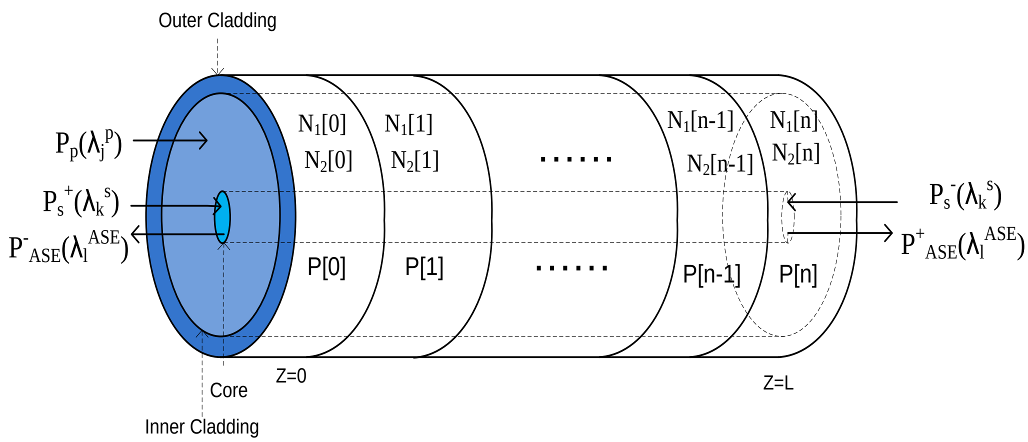

Figure 2-7 Schematic for the simulation model used in the YDFA. See the text for details.

If the pump beam and signal beam are coupled in from the left end, the initial boundary conditions used to solve the equations are the powers of the incident pump and signal energies at $z=0$. Either the pump beam or the signal can be injected from the right end, then the initial boundary conditions change to the power of the incident pump or signal energies at $z=L$. The forward and backward ASE powers grow from zero at each end of the fiber.

In the dual-wavelength YDFA system simulation work of this thesis, the pump beam is divided into five spectral channels with a channel width of about 1 nm and the signals are assumed to be monochromatic. Although it is proved that the number of ASE channels in the numerical model can be kept relatively small according to the concept of an effective ASE bandwidth [23], the ASE spectra are divided into 101 channels from 1000 to 1100 nm with a channel width of about 1 nm to ensure high accuracy. The author was using a simulator developed by A. Budz [7] before the present software is developed. The simulator of A. Budz employed fixed and limited number of channels for seed beams, pump beams and ASE. The present one can provide arbitrary number of channels, which provides the possibility to process more complex cases.

A summary of validation steps for the simulations is given in Appendix B.

2.5 Nonlinearities of Fibers

As the power density in the core of doped-fiber is increased, a point is reached at which some nonlinear effects cannot be neglected. The nonlinear effects in optical fibers can be classified into two categories. The first category of nonlinear effects is nonlinear inelastic scattering process including stimulated Raman scattering (SRS) and stimulated Brillouin scattering (SBS). The second category encompasses the intensity-dependent variations of refractive index, including self-phase modulation (SPM), cross-phase modulation (XPM) and four-wave mixing (FWM). [15]

The SRS, SBS and FWM lead to gains or losses in different wavelengths channels, which depends on the intensities of the signals. Powers are extracted from some channels to provide gains to other channels. SPM and XPM only affect the phase of signals, which introduces chirps to pulses.

2.5.1 Stimulated Raman Scattering (SRS)

Raman scattering is a process of inelastic scattering within the fiber in which the light waves interact with the vibrational modes of silica molecules [24]. Figure 2-8 shows the process of Raman scattering. When a photon with energy $h\omega_p$ is incident on a molecule, the molecule can be transferred from the ground state to a virtual state. The molecule will then make a transition back to the vibrational state and release a lower frequency photon with energy of $h\omega_s$. The molecule will relax

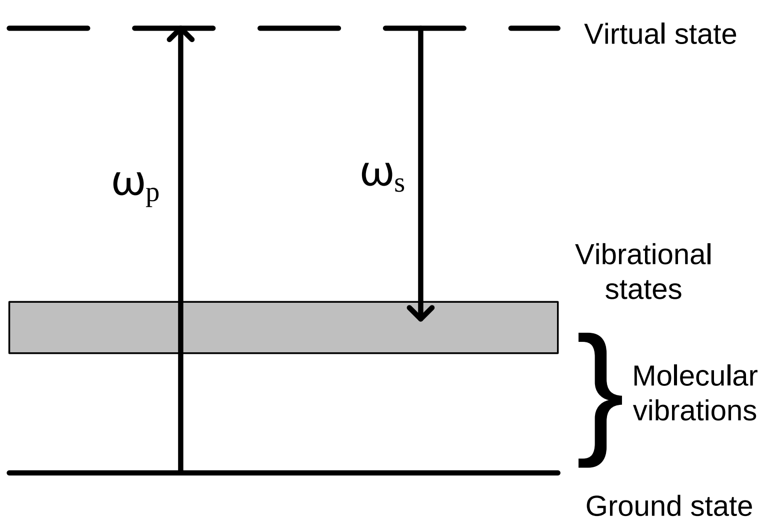

Figure 2-8 Schematic of the stimulated Raman scattering process

from the vibrational state back to the ground state by releasing a phonon. This process is called Raman scattering. Under high laser power conditions, stimulated Raman scattering (SRS) can occur [25]. The injected signal which is the source of the photons and supplies power for the generated wave is usually called *pump wave*. The generated wave dominates in the same direction to the pump wave.

If another signal is present with frequency of ω_s, the SRS light will amplify it and the original light with frequency of ω_p will decrease in power. SRS could transfer energy between two signal channels. Even one signal is able to generate new wavelengths by SRS. Therefore, SRS could greatly limit the performance of amplification system developed in this thesis. Estimating the threshold power of SRS will help to appraise the influence caused by SRS. The threshold power of SRS, defined as half of the incident power is lost at which due to SRS at the output end of a fiber of length L, is estimated by Equation (2-14) [26],

$$g_R P_{th(SRS)} L_{eff} / A_{eff} \approx 16 \tag{2-14}$$

where g_R is the Raman-gain coefficient, $P_{th(SRS)}$ is the threshold power, A_{eff} is the effective mode area, and L_{eff} is the effective interaction length, defined by [26]

$$L_{eff} = [1 - \exp(-\alpha L)] / \alpha \tag{2-15}$$

where α is the background attenuation coefficient of the fiber.

2.5.2 Stimulated Brillouin Scattering (SBS)

Stimulated Brillouin scattering (SBS) arises when light waves interact through an acoustic wave [24]. The process of SBS is similar to SRS and is relevant for high laser powers. The main difference between the two is that acoustic phonons participate in SBS while optical phonons participate in SRS [26]. The generated wave by SBS propagates principally backward relative to the pump wave.

The threshold power of SBS can be estimated similarly to the case of SRS, as shown in Equation (2-16) [26],

$$g_B P_{th(SBS)} L_{eff} / A_{eff} \approx 21 \qquad (2\text{-}16)$$

where g_B is the Brillouin gain coefficient. $P_{th(SBS)}$ is the threshold power defined as at which half of the incident power is lost to SBS at the output end of a fiber of length L. L_{eff} and A_{eff} are the effective interaction length which defined by Equation (2-15) and the effective mode cross section respectively.

2.5.3 Self-Phase Modulation (SPM) and Cross-Phase Modulation (XPM)

The refractive index n of many optical materials is dependent on the optical intensity. The refractive index can be is given by [15]

$$n = n_0 + n_2 I \tag{2-17}$$

where n_0 is the ordinary refractive index of the material, n_2 is the nonlinear index coefficient and I is the optical intensity, defined as the optical power per effective area in the fiber. This change in the refractive index of a material, which responds to an applied electric field, is called the Kerr effect.

The intensity dependence of the refractive index results in two widely studied nonlinear effects: self-phase modulation (SPM) and cross-phase modulation (XPM). SPM refers to the self-induced phase shift of an optical wave when it propagates in optical fibers. The magnitude of the phase shift of an optical wave can be obtained by [27]

$$\phi = \frac{2\pi}{\lambda} nL = \frac{2\pi}{\lambda}(n_0 + n_2 I)L = \frac{2\pi}{\lambda} n_0 L + \frac{2\pi}{\lambda} n_2 IL \tag{2-18}$$

where λ is the wavelength of the optical wave and L is the fiber length. The first item in the right hand side of Equation (2-18) represents the ordinary phase shift when the optical wave propagates in optical fibers. The second item represents the intensity-dependent nonlinear phase shift due to SPM. The maximum phase shift due to SPM is given by [27]

$$\phi_{\max(SPM)} = \gamma P_0 L_{eff} \tag{2-19}$$

where P_0 is the peak power of the incident pulse and γ is the nonlinear parameter which is an important parameter in studying of nonlinear effects. SPM can broaden the spectral of ultrashort pulses and produce optical solitons in the anomalous-dispersion regime of fibers [8].

XPM refers to the nonlinear phase shift of an optical wave induced by another optical wave which has a different wavelength, direction, or state of polarization [27]. When two optical waves with intensities I_1 and I_2 propagate simultaneously in the fiber, the phase shift for the optical wave with intensity of I_1 is given by [27]

$$\phi = \frac{2\pi}{\lambda} n_0 L + \frac{2\pi}{\lambda} n_2 I_1 L + \frac{2\pi}{\lambda} n_2 (2I_2) L \tag{2-20}$$

The first two items on the right hand side of Equation (2-20) represent the phase shift induced by the ordinary phase shift and SPM respectively. The third item represents the nonlinear phase shift due to XPM. If the intensities are the same for two optical waves with different wavelengths, the nonlinear phase shift due to XPM is twice of that due to SPM. The maximum nonlinear phase shift for one optical wave depends not only on its own power but also on the power of another optical wave. The maximum phase shift for the optical wave with power of P_1 is given by [26]

$$\phi_{\max\ (SPM\ \&\ XPM)} = \gamma L_{eff} (P_1 + 2P_2) \tag{2-21}$$

where P is the power of another optical wave. Equation (2-21) can be modified to apply to multi-channels XPM [26] [27] [28].

2.5.4 Four-wave Mixing

Four-wave mixing (FWM) is a third-order nonlinearity which can be observed when signals at different frequencies propagates through the fiber. When three optical waves with frequencies of v_i, v_j and v_k copropagate in the fiber simultaneously, a fourth wave with frequency of v_{ijk} will be generated, which is given by [28]

$$\nu_{ijk} = \nu_i \pm \nu_j \pm \nu_k \tag{2-22}$$

In principle, several frequencies will be generated because of the different combinations of plus and minus signs in Equation (2-22). However, in practice, most of the combinations are not realized [27]. The most troublesome frequency combination is $v_{ijk} = v_i + v_j - v_k$ when wavelength channels are located near the zero-dispersion point [26]. When the new frequency is located in a signal channel of the original frequencies, severe crosstalk will be caused.

The power of the new generated frequency optical wave, $P_{ijk}(L)$, at the exit of a fiber, is given by [15]

$$P_{ijk}(L) = \eta (D\kappa)^2 P_i(0) P_j(0) P_k(0) \exp(-\alpha L) \tag{2-23}$$

where the $P_i(0)$, $P_j(0)$ and $P_k(0)$ are input powers of the signals at frequencies of v_i, v_j and v_k. η is the efficiency of the four-wave mixing, D is the degeneracy factor, which has the value of 3 or 6 for two waves mixing or three waves mixing, and κ is the nonlinear interaction constant which is given by

$$\kappa = \frac{32\pi^3 \chi_{1111}}{n^2 \lambda c} (\frac{L_{eff}}{A_{eff}}) \tag{2-24}$$

where χ_{1111} is the third-order nonlinear susceptibility.

In a dual-wavelength system, the third frequency v_k in Equation (2-22) can be considered as the first frequency v_i or the second frequency v_j. In experimental scenario, Equation (2-22) can be modified to [15]

$$\nu_3 = 2\nu_1 - \nu_2 \quad \text{and} \quad \nu_4 = 2\nu_2 - \nu_1 \tag{2-25}$$

where v_3 and v_4 are the new frequencies generated by FWM in a dual-wavelength system. The powers of the new generated frequency optical waves can be modified to

$$P_3 = \eta (D\kappa)^2 P_1^2 P_2 \exp(-\alpha L) \quad \text{and} \quad P_4 = \eta (D\kappa)^2 P_1 P_2^{\,2} \exp(-\alpha L) \tag{2-26}$$

2.6 Mechanism of Photodarkening

There are numerous reports about the occurrence of the photodarkening effect in the matrices of fiber amplifiers. Although a variety of experiments and theories are presented to explain the mechanisms of photodarkening, it has not been physically verified. However, it is mainly attributed to the formation of color centers [10] [11] [29] [30]. Color centers are defects in the YDFAs which absorb both pump and signal lights in the visible and near infrared ranges [10]. This absorption of light reduces the ability of YDFAs to amplify an input signal, so that higher pump powers have to be used to compensate the reduction. However, the formation mechanisms of the color center still remain largely unexplained. In this section, some theories which contribute to the formation of color centers will be presented.

2.6.1 Photoionization

It is reported that one formation mechanism of color centers in glass is photoionization. Photoionization is a physical process in which one or more electrons are ejected from an atom, ion or molecular by injected photons. The photoionization energy for pure silica is about 8-9 eV. The energy of a single pump photon at 976 nm is about 1.35 eV. Thus the interaction among seven excited Yb ions which can provide a total energy of about 9.45 eV would be sufficient to ionize pure silica [10].

The level of population inversion in an YDFA is considered as the primary controlling parameter for the photodarkening rate [10] [31]. It has been reported that the rate of photodarkening in an YDFA is proportional to the population inversion level to a power of 7 [10] [32]. It implies that about 7 closely associated Yb ions may involve in the photodarkening process. It should be noted that a given fiber which is used in a pulsed laser will photodarken 10^5-10^7 times faster when it is operated in a C.W. laser due to the higher levels of population inversion.

2.6.2 Oxygen Deficiency Center

One theory which attempts to explain the causes behind the photodarkening effect is the formation of color centers due to the presence of Oxygen Deficiency Centers (ODCs) [11] [29]. In Yb-doped fibers, the co-dopant composition, aluminum, with tetrahedral or octahedral coordination, creates voids around oxygen atoms in the silica glass, which are then preferably occupied by doped rare-earth ions. When the number of Yb ions becomes greater than the available voids, there is a higher chance for the formation of some ill-valenced bonds such as Yb-Yb or Yb-Al ion pairs which can cause the oxygen deficiency center (ODC).

The ODCs present in a matrix release a free electron when irradiated at a resonant wavelength, which will be trapped at nearby Yb^{3+} ions and then forms a color center. The ODC theory about the formation of color centers is supported by the observation that thermal annealing in an oxygen environment (O_2 loading technique) has been shown to reduce the loss at 633nm from 3.3dB/m to 2.1dB/m

[11]. It shows that O_2 loading suppresses the generation of ODCs in the silica matrix.

2.6.3 Charge-transfer Band

It is reported by M. Engholm *et al.* that the mechanism of color center formation in YDFA is related to the presence of a charge-transfer (CT) absorption band in the ytterbium-doped silicate glass matrix [9] [30]. A CT transition indicates an electron transfers from the surrounding ligands to the central metal ion. Then a Yb^{2+} ion is formed with a delocalized hole bound to that ion, replacing a Yb^{3+} ion which has the function of amplification. These Yb^{2+} centers no longer contribute to the gain of signals. Thus it is believed that excitation into the CT-band largely accounts for the photodarkening effect.

A strong CT absorption band is found near 230 nm in aluminosilicate YDFA, the CT band is shifted to shorter wavelengths in phosphosilicate YDFA [9]. The formation of color centers in the aluminosilicate glass matrix is considered to be probably related to the hole defects while the color centers in phosphosilicate glass matrix are likely correlated to phosphorus oxygen hole centers (POHCs).

2.6.4 Yb^{3+} Ion Pairs

Another work demonstrated that the Yb^{2+} centers are formed from neighboring Yb^{3+} ions by the Yb^{3+} ion pairs capturing the Compton electron ions [12] [33]. Therefore highly doped fibers, in which the Yb ion pairs are more likely to appear, are more susceptible to photodarkening. This theory is supported by an experiment in which a H_2-annealed Yb-doped fiber was used to reduce the number of Yb^{2+} ions [12].

2.7 Numerical Model of Photodegradation

A numerical model has been developed by P. Laperle *et al.* to calculate the photodegradation in the fiber core with a time-dependent stretched-exponential function [34],

$$\alpha_E(\lambda, z, t) = \alpha_{E,\max}(\lambda)\{1 - \exp[-\nu(\lambda, z, t)t)^{\beta}]\} \tag{2-27}$$

where α_E is the photo-induced excess loss coefficient, $\alpha_{E,max}$ is the maximum excess loss which is wavelength dependent, ν is the photodarkening rate coefficient which depends on wavelength, position along the fiber and time, β is the stretch-exponent.

The numerical results showed good agreement with experimental results. It will be helpful in understanding the mechanism of photodarkening.

2.8 Equipment Used in the Microscope Study

2.8.1 Focused Ion Beam (FIB) Technology and In Situ Lift-out

The focused ion beam (FIB) approach is a technique used in semiconductor and materials science research. A FIB system has an imaging function similar to that of a scanning electron microscope (SEM) and a precision machining tool [35] [36]. Fundamentally, a FIB system generates a high-energy ionized atom stream and focuses it onto the sample for etching or milling the surface, and imaging as well. Ionized atoms of a relatively massive element are used, which enables them to easily expel the surface atoms on the sample and generate secondary electrons from the surface atoms, which can image the sample in the machining process. The FIB system also has some other functions, such as deposition and implantation.

The FIB setup used for this thesis is *Zeiss NVision 40 FIB-SEM*. The NVision 40 combines a high resolution SEM to the precision milling and nanofabrication abilities of a high resolution FIB. Ga^{+} ions are used as the ion source in this system.

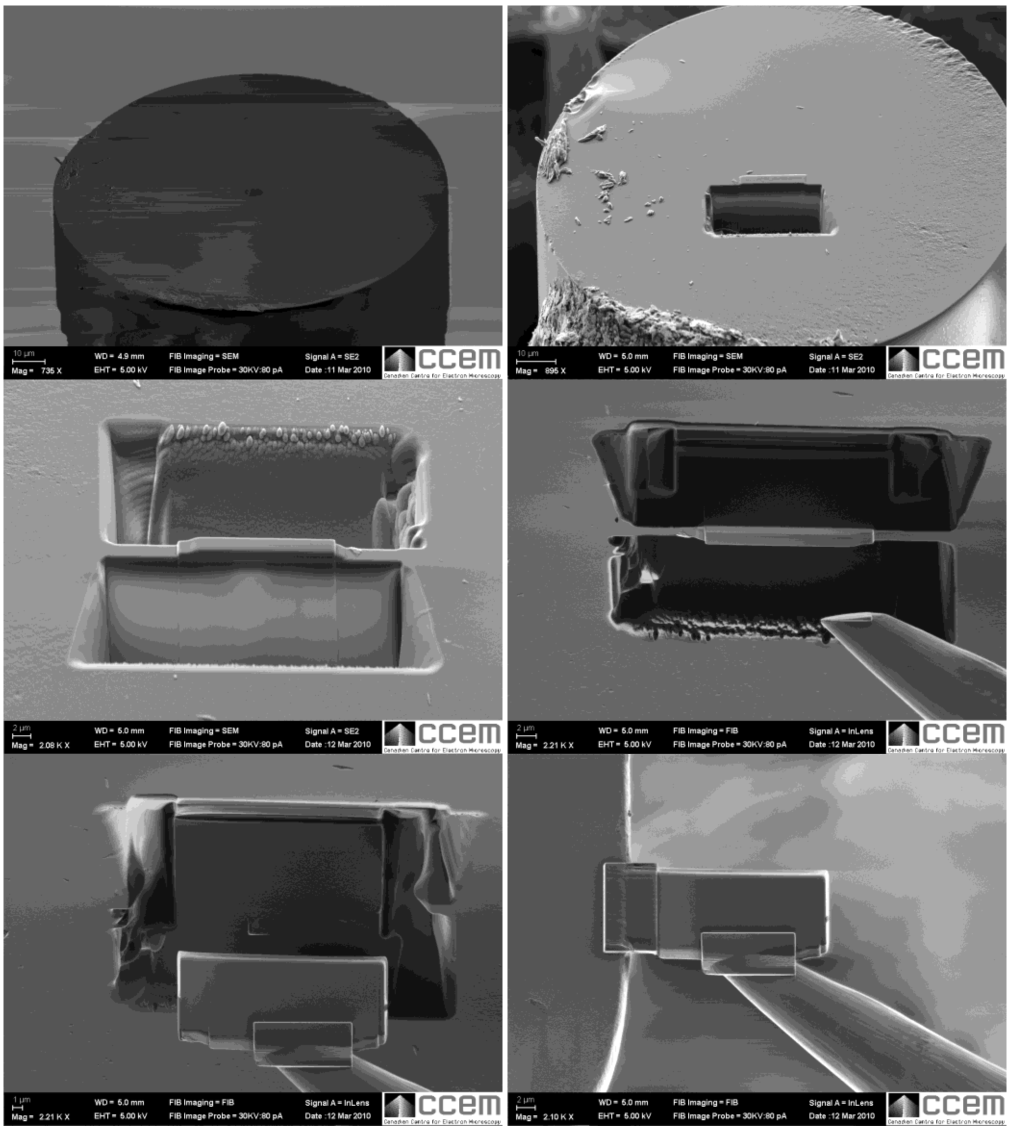

Figure 2-9 A series of SEM images showing the in situ lift-out procedure. (a) is the cross section image of a fiber. (b) and (c) show trench milling process. (d) to (f) show the thinned sample being lifted out by a glass rod and then put onto a TEM grid.

In situ lift-out is a technique developed for lifting out the thinned slice sample directly from the original bulk material [37]. The lifting out procedure used in this thesis is shown in Figure 2-9. Figure 2-9 (a) is the cross sectional image of a fiber. Figure 2-9 (b) and (c) show that both sides of the site to be characterized are trench milled. The thickness of the slice is estimated to be about 60 nm. Figure 2-9 (d) to (f) show the thinned sample is lifted out using a glass rod and then put onto a TEM grid.

2.8.2 Microtome

A microtome is a sectioning instrument used to prepare samples for observation with the optical microscope or electron microscope. It is used to cut materials into extremely thin slices for observation under transmitted light or electron radiation [38]. There are three kinds of blades used with the microtome; steel, glass, and diamond, depending on the sectioning requirements. Steel blades are used to cut animal or plant tissues, which are relatively soft, to make specimens for light microscopy histology which does not require extremely thin specimens. The steel blade is relatively cheap, very efficient and widely used in biology. Glass blades are used to cut soft materials into extremely thin sections to prepare specimens for electron microscopy, and can also be used to make light microscopy specimens whose material is not suitable to be cut by a steel blade. Finally, diamond blades are used to cut hard materials (i.e. bones, teeth). By choosing different grades of diamond knives, one can cut sections with different thicknesses. The sections which have a normal thickness can be used for light microscopy and the extremely thin sections can be used for electron microscopy.

The microtome machine referenced in this thesis is *Leica UltraCut E* Microtome. This precision instrument is designed to construct consistently high quality ultra-thin sections for electron microscopy to semi-thin sections for light microscopy. Sections of 70 nm and less are usually created with the use of special gem-quality diamond knives.

2.8.3 Mechanical Polishing

Mechanical polishing can be used to prepare TEM samples of almost all materials in bulk form [39]. Polishing is usually done on a tripod polishing machine with high resolution sandpaper. The sample is fixed to the tripod polishing machine and makes contact with the sandpaper at a certain angle while the sandpaper is rotating to polish the sample. An additional fine method, ion milling, is usually applied to perform final stage thinning after mechanical milling. Ion milling is a sputtering process that can remove very fine quantities of material. Inert gases, such as argon, are used to generate an ion beam through an electric field and then hit the surface of the sample. The energy of the ion is typically a few keV. The sample is rotated during the milling process to insure smoothness of the sample surface. The ion milling rate is in the range of tens of micrometers per hour, which insures extremely fine polishing.

The mechanical polishing machine used in this thesis is the *ALLIED MultiPrep System 15-2000* and the ion milling machine is *Gatan 691 precision ion polishing system (PIPS)*. The MultiPrep system is a precise semi-automatic TEM sample preparation machine. It enables parallel polishing, angle polishing, site-specific polishing or any combination of the above. Sometimes it can provide samples precise enough that ion milling can be avoided. The PIPS is a sophisticated low angle ion milling setup with high milling rate. The standard milling angle is 4 °. However, it can be varied between 1° and 7 ° [39].

2.8.4 Scanning transmission electron microscopy (STEM)

Scanning transmission electron microscopy (STEM) is used to characterize the distribution of single ytterbium atoms in doped optical fibers. STEM is a type of transmission electron microscopy (TEM) technique whereby a beam of electrons is transmitted through an ultra-thin specimen, interacting with the specimen when it passes through [40]. The electrons which are transmitted through the specimen will be collected by an imaging device, such as a CCD camera, a layer of photographic film, or a fluorescent screen, and then form an image which includes information about the construction or composition of the specimen. TEMs have a much higher resolution than light microscopes due to the small de Broglie wavelength of electrons. TEMs can reach a resolution where even a single column of atoms can be observed. Nowadays, TEMs are widely used in physical and biological sciences to characterize the materials. The feature of STEM which is different from conventional transmission electron microscopes is that it can focus the electron beam into a narrow spot which is scanned over the sample. In this section, some important basic concepts of general TEM and special configurations of STEM will be introduced.

When the focused electron beam interacts with the specimen, the electron can change both its amplitude and its phase. Both types of change can be reflected at the final image, namely amplitude contrast and phase contrast. In most observation situations, both types of contrast actually contribute to the final image although only one plays a dominant role. The TEM applied in this thesis is amplitude contrast. Amplitude contrast results from variations in atomic mass and specimen thickness. It is assumed in this study that the thickness of a specimen is uniform and the amplitude contrast only depends on atomic mass.

There are two basic ways to form images, bright field (BF) and dark field (DF). Figure 2-10 shows the basic concepts of both BF and DF in TEM and STEM. In TEM, the incident beam is transmitted through the specimen, splits into a direct electron beam which keeps the incident direction and a scattered electron beam which is scattered by the atoms in the sample. If all of the electrons are collected to form an image, the contrast will be poor due to many beams contributing to the image which causes the diffraction contrast to be lost. So an objective aperture is needed as shown in Figure 2-10 (a) and (b). A bright field (BF) image is formed by selecting the direct beam, and a dark field (DF) image is usually formed by selecting one of the scattered beams. In a BF imaging system, the aperture can receive electrons only when there are no atoms to scatter the incident electrons, thus bright spots represent empty spaces in BF images. Conversely, in a DF imaging system, only scattered electrons can be collected, therefore bright spots

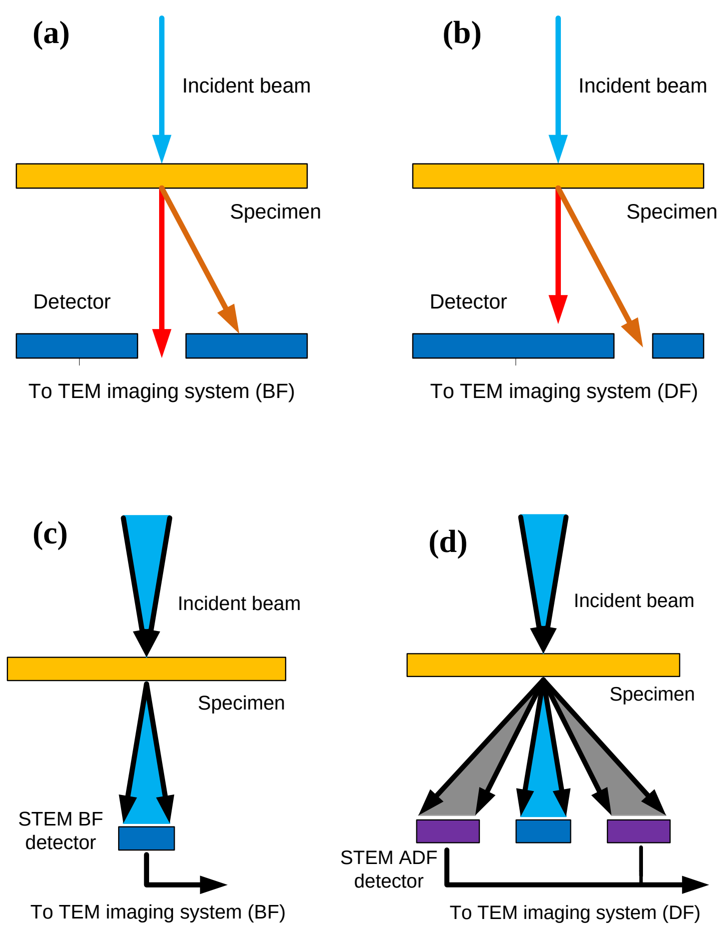

Figure 2-10 Principles of (A) BF of TEM (B) DF of TEM (C) BF of STEM (D) DF of STEM

represent materials in DF images. In a STEM system (Figure 2-10 (c) and (d)), only large-angle elastic scattered electrons will be collected by the ring-shaped detector. When the scanning beam is focused on a certain point on the specimen (the probe size of a scanning beam is at 10^{-11} m order of magnitude), the detector (either BF or DF) receives electrons and the intensity of the received electrons will be reflected in the image. A BF imaging system is usually used to characterize the periodic structure of the specimen. A DF imaging system was used for this thesis. The material of the fiber core was amorphous.

To collect the scattered electrons for DF imaging, an annular detector which surrounds the BF detector is applied. Figure 2-11 (a) shows a schematic of electron scattering by a single isolated atom. The annular detector is located on the optic axis and is empty in the middle where the BF detector sits. The electrons are scattered through an angle θ and the total solid angle of scattering is Ω. This process is called annular dark-field (ADF) imaging. However, the ADF always collects electrons not only from the Rutherford-scattering effect, but also from Bragg scattering, which is undesirable. Thus, another detector is introduced which has a larger diameter than normal ADF and picks up the electrons scattered out to higher angles (Figure 2-11 (b)). This detector is called a high-angle ADF (HAADF). The HAADF can minimize the Bragg electrons. If the HAADF detector only collects scattered electrons with an angle of >50 mrad (~3˚), Bragg scattering electrons can be avoided [40]. The high-angle electron-scattering cross-section scales roughly to the atomic number $Z^{1.7}$ which is close to the limit of

Rutherford scattering, Z^2 [41]. As a result, this image mode is usually termed 'Z-contrast' imaging [40] [41]. That means the heavier an atom is, the more electrons can be collected on the HAADF and creating a brighter point on the image.

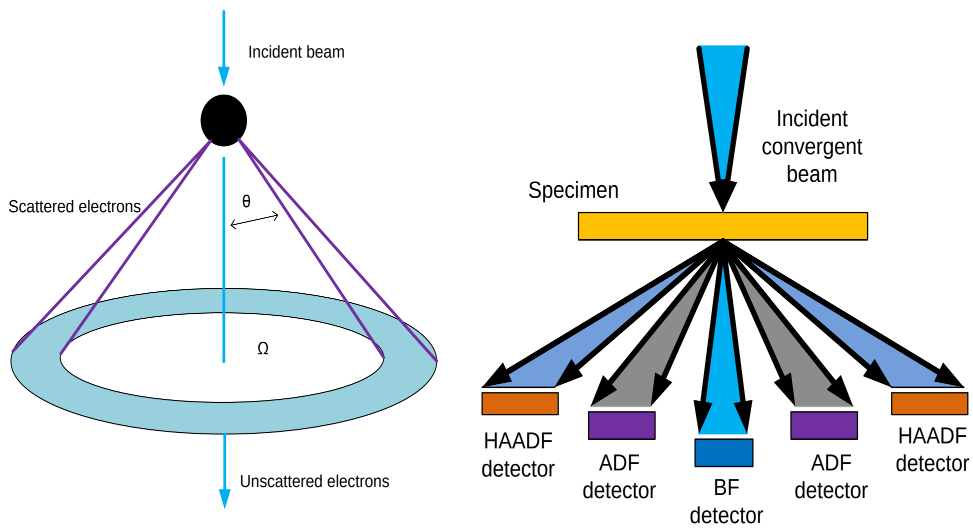

Figure 2-11 (a) Electron scattering by a single isolated atom (b) Schematic of the HAADF, conventional ADF and BF detectors in a STEM.

Figure 2-12 shows an entire view of the major components of a STEM. The electron source produces a 80-300 keV electron beam, the energy of which is sufficient to pass through a sample of 100 nm thickness without significant beam spreading [41]. Then the electron beam goes through a series of electron lenses and corrective optics which can focus the beam down to a diameter smaller than the spaces between the atoms in the sample, and finally scans across the sample. The electrons will be scattered if they encounter atoms and then be recorded by the ADF or HAADF which contributes to DF images. Otherwise, the electrons will go through the sample directly and then be recorded by the electron spectrometer which contributes to BF images. So BF images and DF images can be generated simultaneously in one process. The optimal sample thickness should be thick enough to ensure that bulk-like, but not surface, atoms dominate the signal and thin enough so that the electron probe will not greatly spread in the sample [41].

The STEM system used in this thesis is *FEI Titan 80-300 Cubed.*

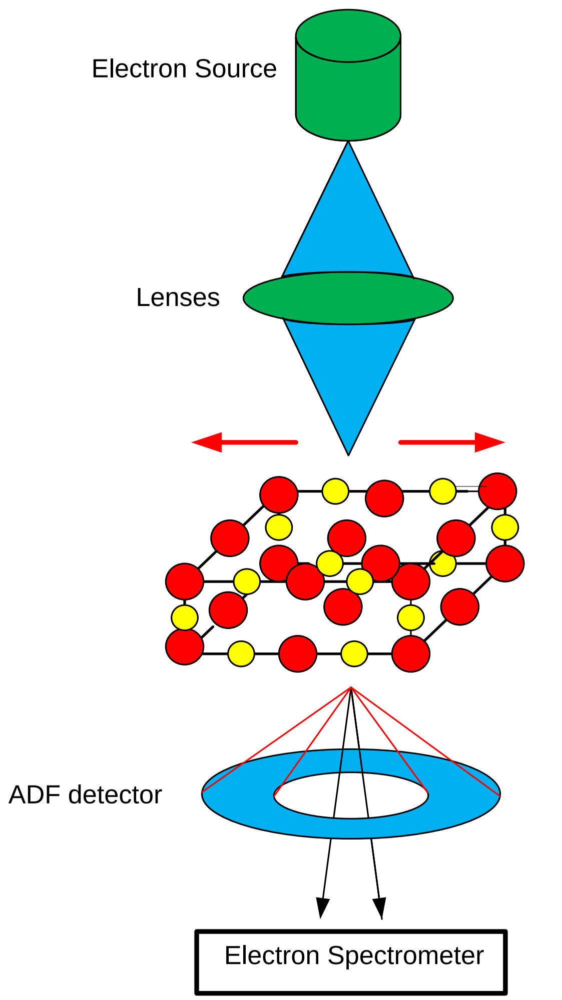

Figure 2-12 Schematic of a STEM system

Chapter 3 Simulation of Ytterbium-doped Fiber Dual-wavelength Amplifier System

Dual-wavelength light sources have potential applications such as generating high-repetition-rate mid-infrared radiation (MIR) by difference-frequency mixing (DFM) or for two-color pump-probe experiments. In this section, numerical simulations are used to model dual-wavelength high-repetition rate ultrafast ytterbium-doped fiber amplifier systems assuming continuous-wave (CW) input signals under various situations. Following the general approach of the existing experimental setup based on a single fiber amplifier, a dual-fiber amplifier system and a two-stage amplification system are simulated to find the optimal fiber lengths for future experimental work.

3.1 Single-fiber Amplifier System

3.1.1 Comparing with the Prototype

Previous experimental research on Yb-doped fiber amplification systems have been carried out by Budz *et al.* [7] as shown in Figure 2-6 (see chapter 2.3). The first step of this part of work is to compare the simulation results with the previous work to prove the validity of the simulation model. A conceptual schematic of the single-fiber amplifier system used by Budz *et al* is shown in Figure 3-1. Two seed beams with wavelengths of 1040 and 1079 nm, were coupled into a Yb-doped double-clad fiber amplifier. The pump beam, with wavelength of 975 nm, was coupled into the fiber counter-directionally. In this case, the direction of the seed beams is defined as backward (incident from z=L) while the direction of the pump beam is defined as forward (incident from z=0). This definition is used throughout this thesis.

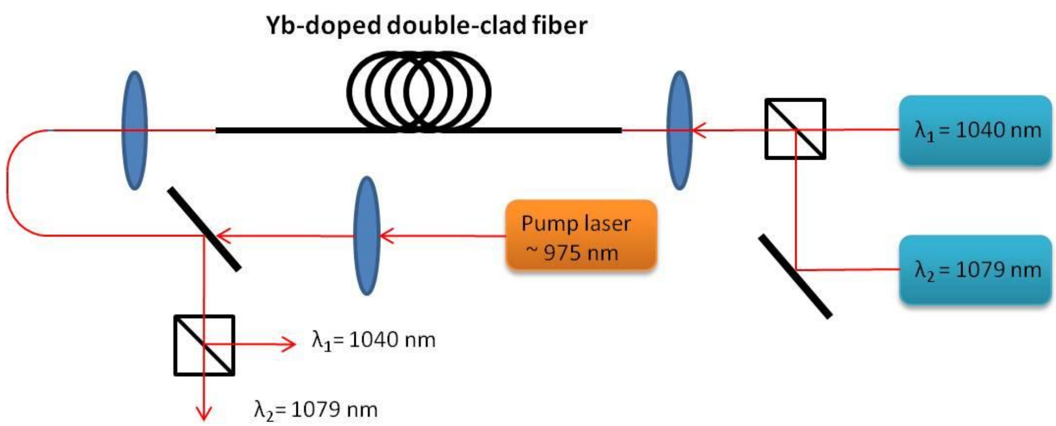

Figure 3-1 A schematic of the single fiber amplifier system

The parameters used in the numerical simulations are shown in Table 3-1. N_T is ytterbium doping density, α is the background attenuation coefficient of the fiber, τ is the florescence lifetime of the upper laser level, A is the doped effective area of the fiber, D, Γ_S and Γ_{ASE} are confinement factors of the pump, signal beams and

ASE in the core area. The range of ASE is from 1000 nm to 1100 nm, which is divided into 101 channels with a width of $\Delta\lambda$=1 nm. The parameters in Table 3-1 are used for all the double-clad fibers in this thesis.

Table 3-1 Parameters Used in the Numerical Simulations

Parameter	Value	Parameter	Value
core diameter	6 μm	λ_1(ASE)	1000 nm
cladding diameter	125 μm	λ_{101}(ASE)	1100 nm
N_T	8×10^{25} m^{-3}	$\Delta\lambda$	1 nm
α	9×10^{3} m^{-3}	Γ_s	0.87
τ	0.8 ms	Γ_{ASE}	0.87
A	2.827×10^{-11} m^2	D	2.304×10^{-3}

The power of each seed beam is 100 μW. The pump beam power used in this case is 2.109 W, which is divided into five spectral channels. The distribution of the power in five channels is shown in Table 3-2. Since the powers of the seed and pump beams indicate the powers which have already coupled into the fiber, the numerical aperture (NA) is not introduced in this model.

Table 3-2 Parameters Used in Figure 3-1

	Wavelength	Power		Wavelength	Power
Seed 1	1040 nm	100 μW	P_2	973.3 nm	0.469 W
Seed 2	1079 nm	100 μW	P_3	974.5 nm	0.703 W
Pump	~975 nm	2.109 W	P_4	975.5 nm	0.469 W
P_1	972.6 nm	0.234 W	P_5	976.3 nm	0.234 W

Figure 3-2 (a) shows the power distributions of the amplified signal beams and pump beam inside a 6.87-m-long fiber. The light blue curve, which represents the pump is injected at z=0 while the dark blue and red curves, which represent the seeds, are launched into the other end of the fiber at z=L. The pump beam is absorbed while it propagates along the fiber. The unused pump energy at the end of fiber is 8.60% of the total pump energy. The 1040 nm seed beam gains more energy by stimulated emission than the 1079 nm seed beam due to the greater emission cross-section. However, the 1040 nm seed beam also suffers a greater reabsorption which is due to the greater absorption cross-section and decreases the power. This results from the quasi-3-level electronic structure of Yb^{3+} ions. The Yb^{3+} ion exhibits a 3-level-like character at 1040 nm, with significant signal reabsorption, while it exhibits a 4-level-like character at 1079 nm, with weak reabsorption [13]. Thus the power of 1079 nm seed has an opportunity to catch up with that of 1040 nm seed at a certain fiber length. This fiber length is called the

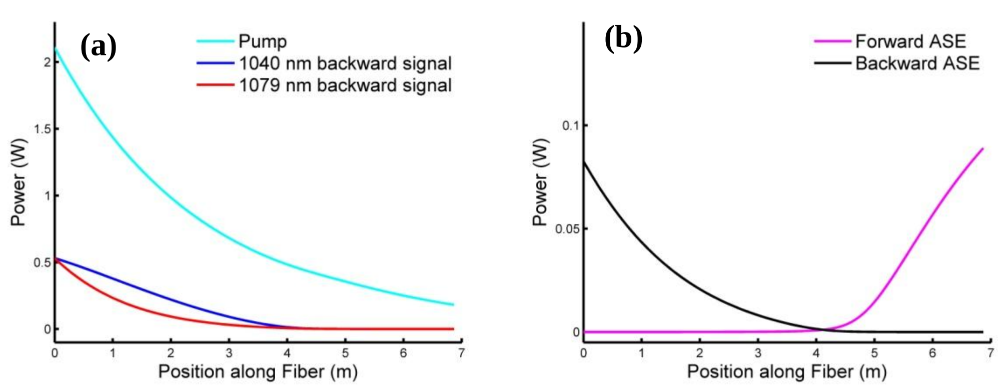

Figure 3-2 Power distribution of (a) the amplified signals and pump beams, and (b) the ASE inside a 6.87-m-long fiber amplifier. The wavelengths of seed beams are 1040 nm and 1079 nm.

optimal fiber length which can make the power of two output seed beams equal. The optimal fiber length is 6.87 m in this case.

Figure 3-2 (b) shows the power distribution of ASE along the fiber. The black curve is referred as the backward ASE which propagates along the same direction as the signals. The purple curve is referred as the forward ASE which propagates in a counter-directional sense. The power of the output seed beams and ASE are shown in Table 3-3.

Table 3-3 The output power of seed beams and ASE in Fig. 3-2

	1040 nm	1079 nm	Backward ASE	Forward ASE
Power (W)	0.531	0.531	0.0826	0.0890

This configuration with all the parameters and outputs is named as the ***prototype*** in this thesis. All the other configurations in this thesis originate from this prototype.

This simulation results agree well with the results in the report of Budz *et al.* [7]. The parameters used in that paper is the same as in the present case, except that in that paper ASE is divided into 11 channels, each with a width of 10 nm. It primarily confirms the reliability of the basic simulation software used in this thesis.

3.1.2 Different Seeding Directions

The simulation model used in this thesis can be applied in different situations. For example, the seed beams or the pump beam can be coupled from different directions. Since changing both directions of seed beams has the same effect as changing the direction of pump beam, only the directions of seed beams are discussed in this section. The configurations in which the seed beams will be coupled into the fiber from different directions will be studied in detail.

Figure 3-3 shows the power distribution of a configuration in which both of the seed beams are coupled into the fiber in the forward direction, the same direction as the pump beam. The results are shown in Table 3-4. Near the beginning part of the fiber at around 1 m length, there is a bump on the pump curve which means that the slope of that curve suddenly changes. This indicates that from that point, the absorption of pump beam grows faster than before. This feature is caused by the fast increase of the 1040 nm signal which extracts substantial energy from the excited state population. The optimal length and output powers are similar to the last case. The power of the ASE in the direction of seed beams is relatively small. Only a fraction of pump energy remains at the end of the fiber, which suppresses the ASE power compared with the last configuration. Thus the signal to noise ratio (SNR) of this configuration is better than the previous one.

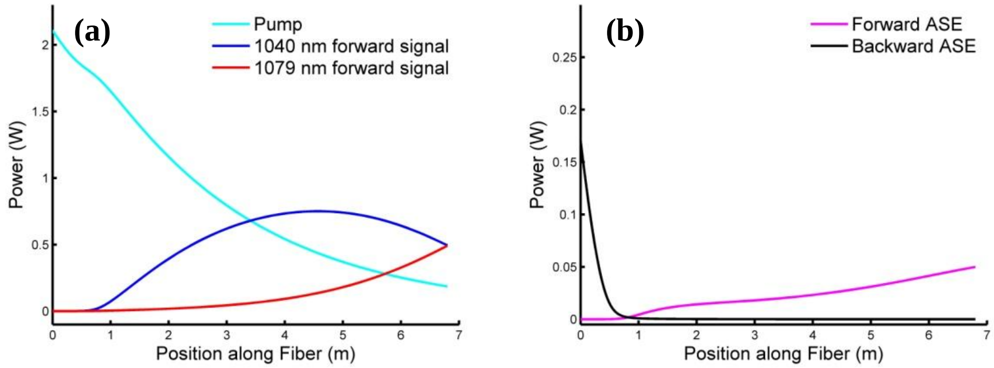

Figure 3-3 Power distribution of (a) the amplified signals and pump beams, and (b) the ASE in a fiber where both 1040 nm and 1079 nm signals propagate forward.

Figure 3-4 shows the power distribution of a configuration in which the 1040 nm signal propagates forward while the 1079 nm signal propagates backward. There is also a bump on the pump curve, around the fiber length of 2 m, which is caused by the rather sudden increase in power of both 1040 nm and 1079 nm signals. The optimal length and output powers are similar to the prototype (see Table 3-4). However, as the output signal comes from different

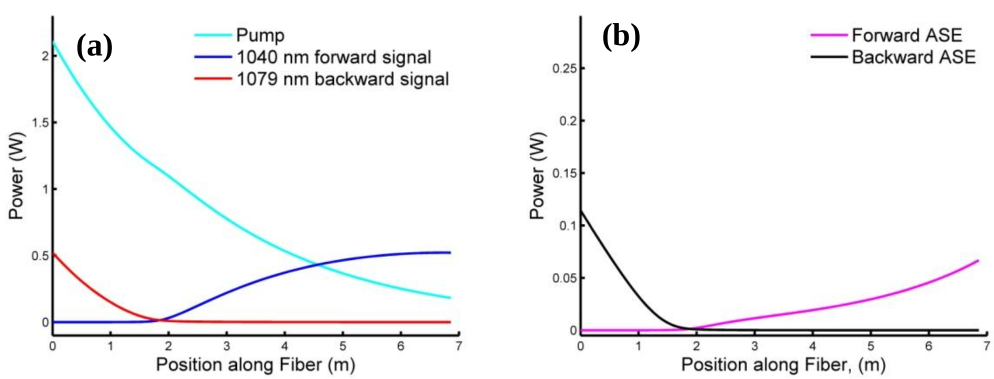

Figure 3-4 Power distribution of (a) the amplified signals and pump beams, and (b) the ASE in a fiber where the 1040 nm signal beam propagates forward while the 1079 nm signal beam propagates backward.

ends, both directions of the ASE power are received with the signals. Thus the SNR is reduced significantly.

Figure 3-5 shows the power distribution of a configuration in which the 1040 nm signal beam propagates backward while the 1079 nm signal beam propagates forward. The forward ASE power decreases toward the end of the fiber. Due to the small emission cross-section, the 1079 nm signal could not grow so fast as the 1040 nm signal in last configuration. Thus the forward ASE plays a greater role around the middle part of the fiber. However, unlike the 1040 nm signal which could be greatly reabsorbed, the 1079 nm signal grows steadily along the fiber and thus suppresses the ASE at the end of the fiber.

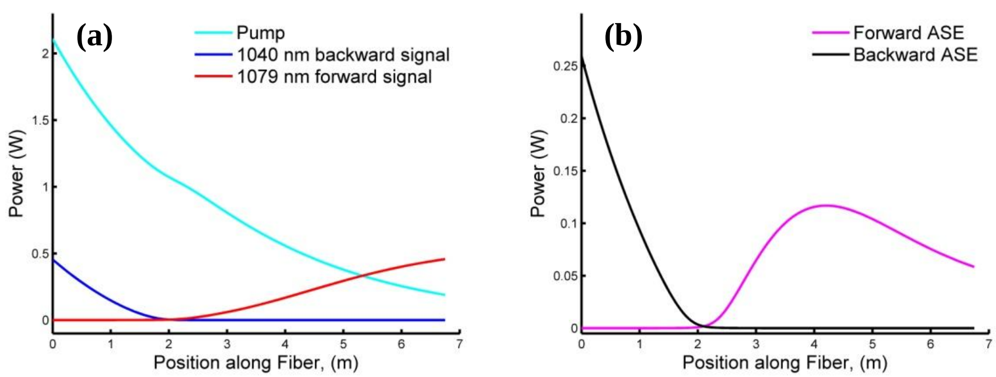

Figure 3-5 Power distribution of (a) the amplified signals and pump, and (b) the ASE in a fiber where the 1040 nm signal propagates backward while the 1079 nm signal propagates forward.

Table 3-4 shows the simulation results for all of the four configurations discussed above. The fiber lengths in the table indicate the conditions for equal output signal powers. The signal to noise ratio (SNR) for the first two configurations in the table is the ratio of the total seed beam output power (the summed powers of the two signals) and the ASE with the same direction, and for the last two is the ratio of each seed beam output power and the ASE in each direction. The energy of ASE is the total energy of 101 channels as described in Table 3-1. These results agree well with the results reported by Budz *et al.* [7]. The backward/backward configuration has the best output power and the forward/forward configuration has the best SNR. The remaining two exhibit no notable benefits. However, as it is reported in [7], except in the first configuration, the signal beams must pass through the same lens which is used to couple the pump beam into the inner cladding. This process requires additional lenses which will further complicate the system. Therefore, the first configuration has the greatest value to instruct future experiments and thus will be used as a prototype model in the following sections.

Table 3-4 Simulation Results for Different Seeding Directions

Signal Direction		Fiber Length (m)	Output signal power (W) (each)	ASE (W) (forward)	ASE (W) (backward)	Signal to noise ratio (SNR)
1040 nm	1079 nm					
Backward	Backward	6.87	0.53	0.0890	0.0826	12.83
Forward	Forward	6.80	0.49	0.0499	0.1709	19.64
Forward	Backward	6.86	0.52	0.0667	0.1143	7.80/4.55
Backward	Forward	6.75	0.45	0.0584	0.2592	1.74/7.71

3.1.3 The Product of the Output Seed Beam Powers

The product of the powers of the two output seed beams in the one-fiber amplifier system is an important parameter in the nonlinear optical applications, such as difference-frequency mixing (DFM). The relationship between the products of the output seed beam powers and the fiber length for different wavelengths of seed beams is studied in this section.

Figure 3-6 (a) shows the output power of each seed beam versus fiber length for the single-fiber amplifier system with the seed beam at wavelengths of 1040 nm and 1079 nm. The configuration and parameters used in this model are the same as in Figure 3-2 (prototype). The red curve indicates the ASE power which propagates in the same direction of seed beams. The 1040 nm signal with a greater emission cross-section grows faster than the 1079 nm signal at the beginning due to the reabsorption effect being relatively small when the fiber is short. However, the power of 1040 nm signal starts to decrease after its peak power at the fiber length of about 4 m due to its stronger reabsorption while the power of 1079 nm signal increases with longer fiber lengths. At the fiber length of 6.87 m, the two seed beams yield equal output powers, which corresponds to Figure 3-2. These results agree well with the results shown by Budz *et al.* [7]. It confirms the simulation software works properly. The results are also confirmed by a simulator developed by M. Hajialamdari [42]. Using their simulator with the same parameters as in the present case, the results are fairly close to Figure 3-6 (a).

At the fiber lengths which make the powers of two output signals equal in two simulators, the difference of the fiber lengths is 2% and the difference of output signal powers is 8%. The differences are in a reasonable range. The differences between the results may be caused by algorithm differences and the different values of absorption and emission cross-sections. The values of cross-sections in both simulators are from Figure 1 in [13]. However, slightly different values may be obtained by extracting values from the figure, which could affect the final results. The two wavelengths competition is very sensitive to the values of cross-sections [43]. Therefore, one can conclude that the results from two simulators agree well with each other within reasonable errors. Figure 3-6 (b) shows the product of two output seed beams versus fiber length. The intensity product has a peak at the fiber length of 6.88 m.

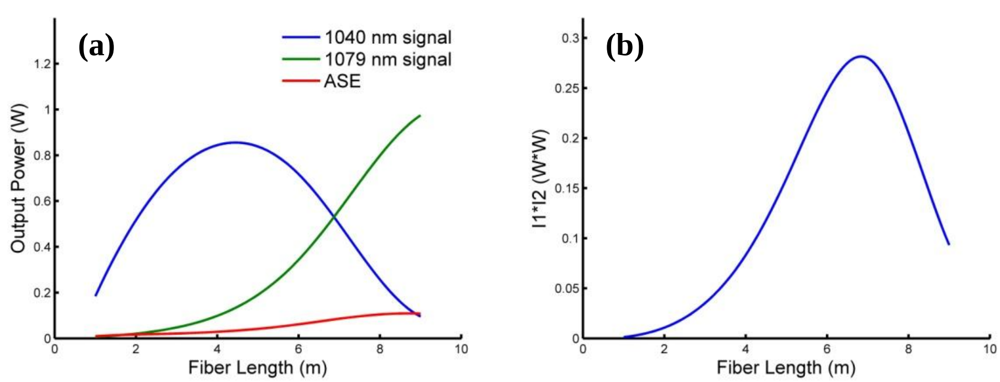

Figure 3-6 (a) The output power of each seed beam versus fiber length and (b) the product of two output seed beam intensities versus fiber length for the seed beams at wavelengths of 1040 nm and 1079 nm.

Seed beams with other wavelengths are also studied to give more guidance for future DFM experiments. Figure 3-7 shows the power distribution of the amplified signals, pump beam and ASE for the seed beams at wavelengths of 1040 nm and 1090 nm. The parameters of the fiber used in this case are from Table 3-2. The input powers and wavelengths of seed beams and the pump beam are shown in Table 3-5. The power of each seed beam is the same as that of the prototype model while the wavelength of seed beam 2 changes to 1090 nm. The pump beam with the same power is also divided into five spectral channels as in the prototype model.

Table 3-5 Parameters used in the numerical simulations in Fig 3-7

	Wavelength	Power
Input seed beam 1	1040 nm	100 μW
Input seed beam 2	1090 nm	100 μW
Pump beam	~975 nm	2.109 W

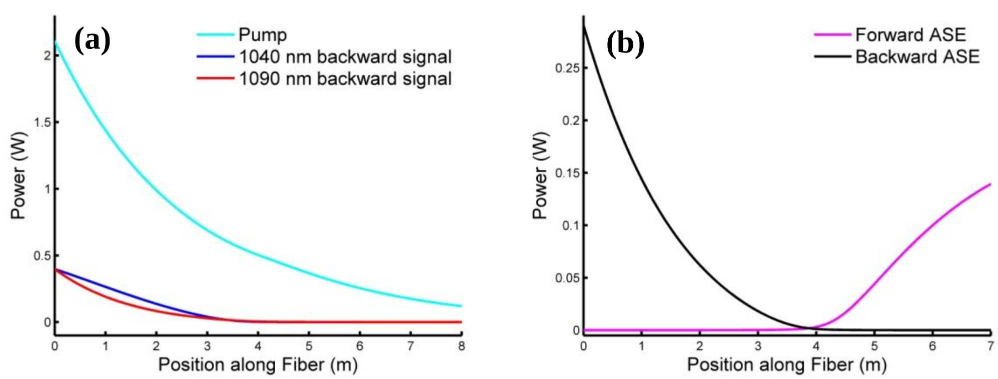

Figure 3-7 Power distribution of (a) the amplified signals and pump, and (b) the ASE inside a 8.814-m-long fiber amplifier for the seed beams at wavelengths of 1040 nm and 1090 nm.

Since the emission cross-section at 1090 nm is smaller than that at 1079 nm, the equality of the 1090 nm and the 1040 nm signal beams is achieved at a longer fiber length. The optimal length for this case is 8.814 m which leads to the two output seed beams having equal powers of 0.397 W. The powers of backward and forward ASE which are shown in Table 3-6 are much greater than those in the prototype model. This is due to the longer fiber length used in this case which can result in more ASE and the smaller power of output seed beams.

Table 3-6 The output power of seed beams and ASE for Fig. 3-7

	1040 nm	1090 nm	Backward ASE	Forward ASE
Power (W)	0.397	0.397	0.2906	0.1755

Figure 3-8 (a) shows the output power of each seed beam versus fiber length for the above system. The trend is similar to the 1040 nm/1079 nm system. The production curve in Figure 3-8 (b) shows the peak of the intensity product is located at 8.03 m.

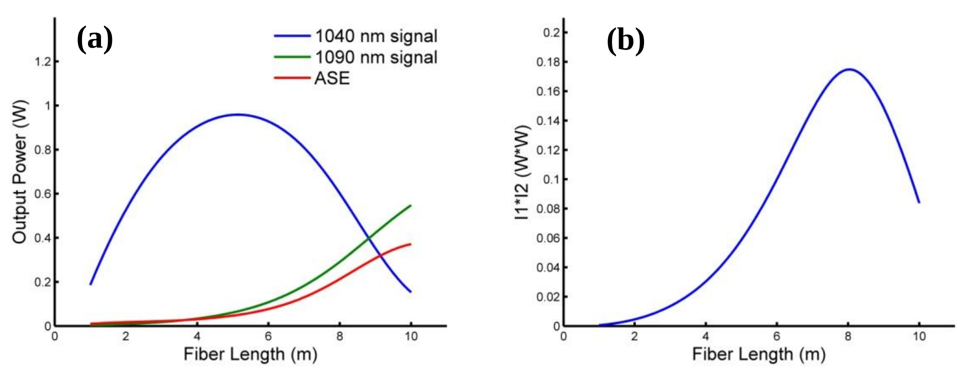

Figure 3-8 (a) The output power of each seed beam versus fiber length and (b) the product of two output seed beam intensities versus fiber length for the seed beams at wavelengths of 1040 nm and 1090 nm.

Figure 3-9 shows the power distribution of the amplified signals, pump beam and ASE for the seed beams at wavelengths of 1035 nm and 1085 nm. The parameters of the fiber used in this case are the same as those of prototype. The input powers and wavelengths of seed beams and pump beams are the same as in Table 3-5, except the wavelengths of seed beams are different.

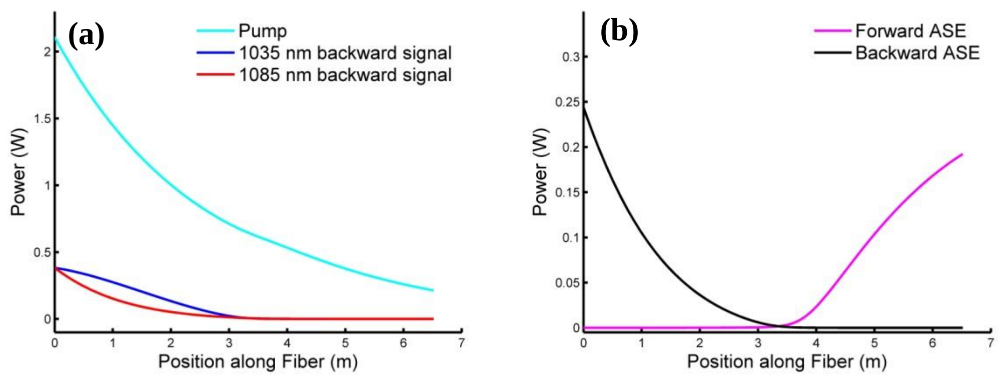

Figure 3-9 Power distribution of (a) the amplified signals and pump, and (b) the ASE inside a 6.517-m-long fiber amplifier for the seed beams at wavelengths of 1035 nm and 1085 nm.

The output power of seed beams and ASE are shown in Table 3-7. The optimal length is 6.57 m. The ASE powers are similar with those of the 1040 nm/1090 nm system but are greater than the prototype model. Although a shorter fiber length is used here, the relatively small power of output seed beams leads to a greater ASE power.

Table 3-7 The output power of seed beams and ASE for Fig. 3-9

	1040 nm	1079 nm	Backward ASE	Forward ASE
Power (W)	0.382	0.382	0.2439	0.1923

Figure 3-10 (a) shows the output power of each seed beam versus fiber length for the 1035 nm/1085 nm system. The trend is similar to the 1040 nm/1079 nm and 1040 nm/1090 nm systems. The peak of the intensity product is located at the fiber length of 6.05 m in Figure 3-10 (b).

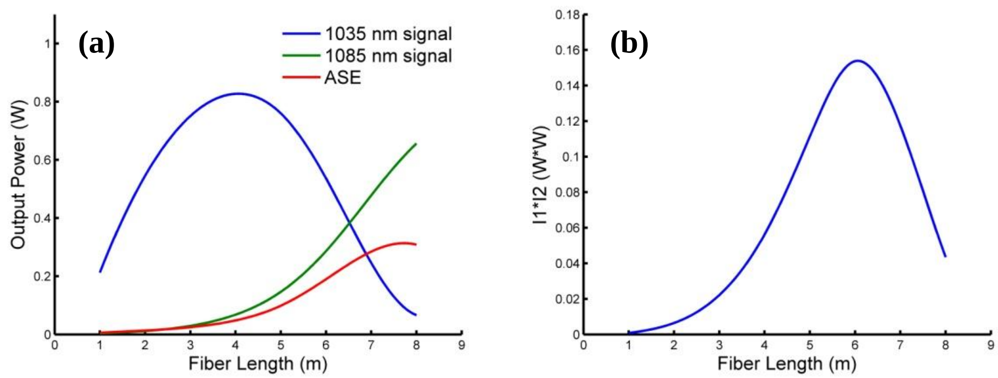

Figure 3-10 (a) The output power of each seed beam versus fiber length and (b) the product of two output seed beam intensities versus fiber length for the seed beams at wavelengths of 1035 nm and 1085 nm.

Figure 3-11 shows the power distribution of the amplified signals, pump beam and ASE for the seed beams at wavelengths of 1035 nm and 1095 nm. The parameters of the fiber used in this case are also from Table 3-2. The input powers and wavelengths of seed beams and pump beams are the same as those of the prototype in Table 3-5, except the wavelengths of the seed beams are different.

Since the 1095 nm wavelength has the smallest emission cross-section among all the seed beam wavelengths used above, the 1095 nm signal grows slowest among all the signals. Therefore the output power of the seed beams at optimal fiber length is the smallest among all the cases (see Table 3-8). The ASE power is relatively large compared with other cases above due to the small power of output seed beams which cannot suppress the ASE.

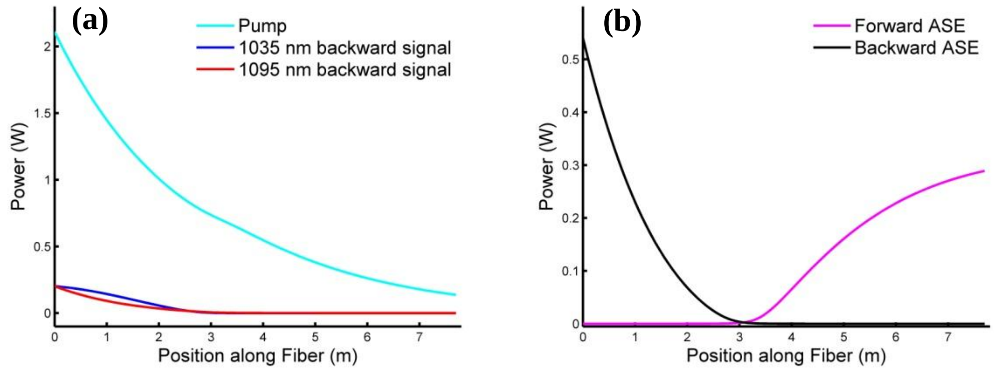

Figure 3-11 Power distribution of (a) the amplified signals and pump, and (b) the ASE inside a 7.699 -m-long fiber amplifier for the seed beams at wavelengths of 1035 nm and 1095 nm.

Table 3-8 The output power of seed beams and ASE for Fig. 3-11

	1035 nm	1095 nm	Backward ASE	Forward ASE
Power (W)	0.202	0.202	0.5404	0.2891

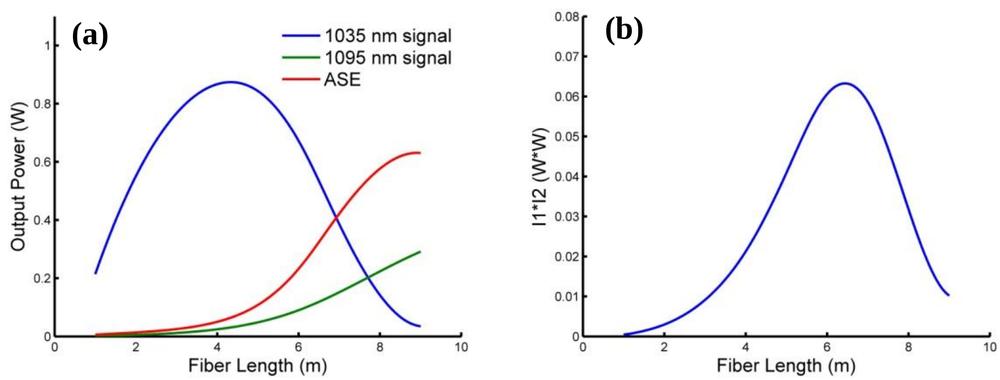

Figure 3-12 (a) The output power of each seed beam versus fiber length and (b) the product of two output seed beam intensities versus fiber length for the seed beams at wavelengths of 1035 nm and 1095 nm.

Figure 3-12 (a) shows the output power of each seed beam versus fiber length for the 1035 nm/1095 nm system, the trend of which is similar to the 1040 nm/1079 nm, 1040 nm/1090 nm and 1035 nm/1085 nm system. The peak of the product of the intensities is located at the fiber length of 6.46 m in Figure 3-12 (b).

3.1.4 Two-sided Pumping

Seeding from both directions of the fiber is discussed above. The pump beam can be also coupled into the fiber from both directions. In this section, a two-sided pumping simulation software is developed. The conceptual figure of a two-sided pumping configuration is shown as Figure 3-13. The same seed beams, pump beams and Yb-doped double-clad fiber as the prototype are adopted in this case. The different part from the prototype is that two pump sources are applied from both ends of the fiber. The input parameters used for this case are shown in Table 3-9.

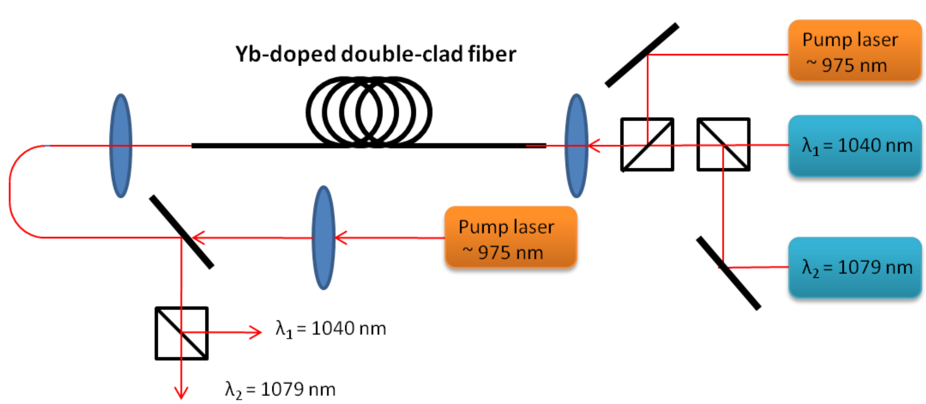

Figure 3-13 A schematic of the single fiber amplifier system pumped from both ends

Table 3-9 Parameters used in the numerical simulations in Fig 3-13

	Wavelength	Power
Seed beam 1 (backward)	1040 nm	100 μW
Seed beam 2 (backward)	1079 nm	100 μW
Pump beam 1 (forward)	~975 nm	2.109 W
Pump beam 2 (backward)	~975 nm	2.109 W

The power distributions of the amplified signals pump beam and ASE in the two-sided pumping configuration is shown in Figure 3-14. The bump on the pump curve is caused by the rather sudden change of the 1040 nm signal power versus position along the fiber, which is similar to that in Figure 3-3. The power of the output seed beams and ASE are shown in Table 3-10. The optimal fiber length is 7.48 m and the output power of seeds is 1.139 W for each, which is nearly doubled compared with the prototype.

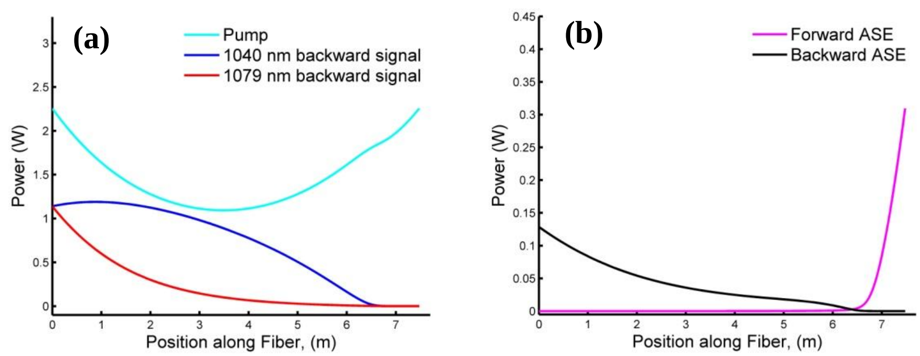

Figure 3-14 Power distribution of (a) the amplified signals and pump, and (b) the ASE inside a 7.48 -m-long fiber amplifier for the seed beams at wavelengths of 1040 nm and 1079 nm in a two-sided pumping configuration.

Table 3-10 The output power of seed beams and ASE for Fig. 3-14

	1040 nm	1079 nm	Backward ASE	Forward ASE
Power (W)	1.139	1.139	0.1286	0.3096

The verification of the simulation software is achieved through two methods. First, one of the pump beams in this two-sided pump configuration is systematically decreased to zero. It shows that if the pump beam which propagates in the same direction as the seed beams is decreased to zero (only counter-directional pump beam is left), the results are exactly the same as Figure 3-2, which shows the results of the one-sided counter-directional pumping configuration. If the counter-directional (to the seed beams) pump beam is decreased to zero, the results are the same as Figure 3-3 which shows the results for which the pump and seed beams propagate in the same direction. Second, the results are also verified by the simulator developed by M. Hajialamdari [42]. The same parameters as in this case are used in that simulator and the results which come out from the two respective simulators agree well within reasonable errors. In Figure 3-14 at the fiber lengths which make the powers of two output signals equal in the two simulators, the difference of the fiber lengths is 0.8% and the difference of output signal powers is 7%.

A configuration in which two pump beams are coupled into the fiber simultaneously from two different directions is developed. Figure 3-15 shows the schematic of a single fiber amplifier system in which the pump beam is split into two parts and then coupled into the fiber from both ends respectively. The parameters of the fiber are same as the prototype (Table 3-2). Table 3-11 shows the input energy and wavelengths of the seed and pump beams. The total energy of the pump beam is 2.109 W, x percent of which is coupled in forward while (1-x)

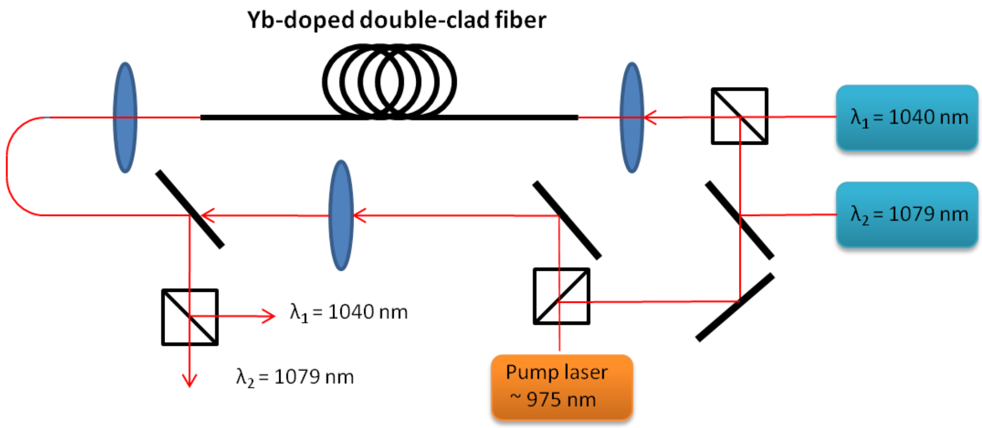

Figure 3-15 A schematic of the single fiber amplifier system pumped from both ends

Table 3-11 Input seed and pump beams for two-end pumping

	Wavelength	Power
Seed beam 1 (backward)	1040 nm	100 μW
Seed beam 2 (backward)	1079 nm	100 μW
Pump beam 1 (x% forward)	~975 nm	2.109 × x W
Pump beam 2 ((1-x)% backward)	~975 nm	2.109 × (1-x) W

Table 3-12 The distribution of pump energy and the corresponding output power

Pump beam 1 (W) (forward)	Pump beam 2 (W) (backward)	Fiber Length (m)	Output signal power (W) (each)	ASE (forward) (W)	ASE (backward) (W)	Signal to noise ratio (SNR)
0 (0%)	2.109 (100%)	6.80	0.492	0.1714	0.0499	19.64
0.211 (10%)	1.898 (90%)	6.82	0.498	0.1624	0.0509	19.57
0.422 (20%)	1.687 (80%)	6.82	0.503	0.1529	0.0517	19.46
0.633 (30%)	1.476 (70%)	6.83	0.509	0.1438	0.0528	19.28
0.844 (40%)	1.265 (60%)	6.84	0.514	0.1349	0.0539	19.07
1.054 (50%)	1.054 (50%)	6.85	0.520	0.1262	0.0553	18.81
1.265 (60%)	0.844 (40%)	6.86	0.524	0.1178	0.0570	18.39
1.476 (70%)	0.633 (30%)	6.87	0.528	0.1099	0.0594	17.78
1.687 (80%)	0.422 (20%)	6.87	0.532	0.1023	0.0629	16.92
1.898 (90%)	0.211 (10%)	6.88	0.533	0.0954	0.0694	15.36
2.109(100%)	0 (0%)	6.87	0.530	0.0890	0.0826	12.83

percent of which is coupled in backward. The pump beam is also divided into five spectral channels as in the prototype.

Table 3-12 shows the different distribution of pump energy and the corresponding output seed beam power, ASE and the signal to noise ratio (SNR). The SNR in this case is the ratio of the total power of output seed beams and the ASE power which propagates in the same direction as the seed beams (backward ASE here). When 100% of pump energy is contained in the forward pump beam (the last scenario in Table 3-12), it corresponds to the prototype model (Figure 3-2, pumping counter-directional to the seed beams). The first scenario in Table 3-12 corresponds to Figure 3-3 (pumping equidirectional to the seed beams). These two special scenarios also verified the validity of the software. Figure 3-16 is the corresponding figure of Table 3-12. The power of the output seed beams has a peak value with the arrangement where 90% of the pump beam propagates forward, which is very close to the prototype model. The power of ASE is

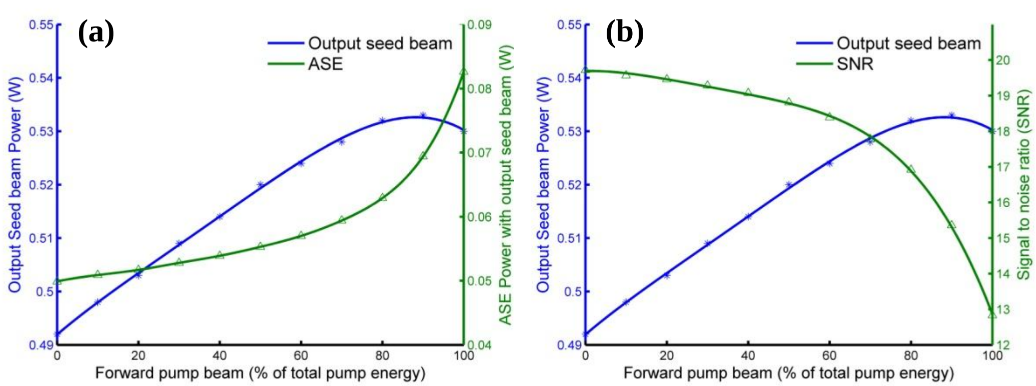

Figure 3-16 The output seed beam power and (a) ASE, and (b) SNR versus the forward pump beam given in terms of the % of total pump energy

monotonically increasing as the percentage of forward pump beam increases. Therefore, although the power of output seed beams increases, the SNR of the system decreases as the pump distribution changes.

3.2 Two-fiber Amplifier System

In the last section, the single-fiber amplifier system was discussed from various aspects. In this section, a two-fiber amplifier system which consists with two separated fiber amplifiers is developed, as shown in Figure 3-17. Seed beams are coupled into the fiber backward while the pump beam is injected in the forward direction. This configuration could provide a more flexible amplification range than the single-fiber amplifier system, which is required by the experiments of mid-IR generation. The disadvantage is that additional devices are needed to synchronize the output seed beams. Although difficulties may be encountered in

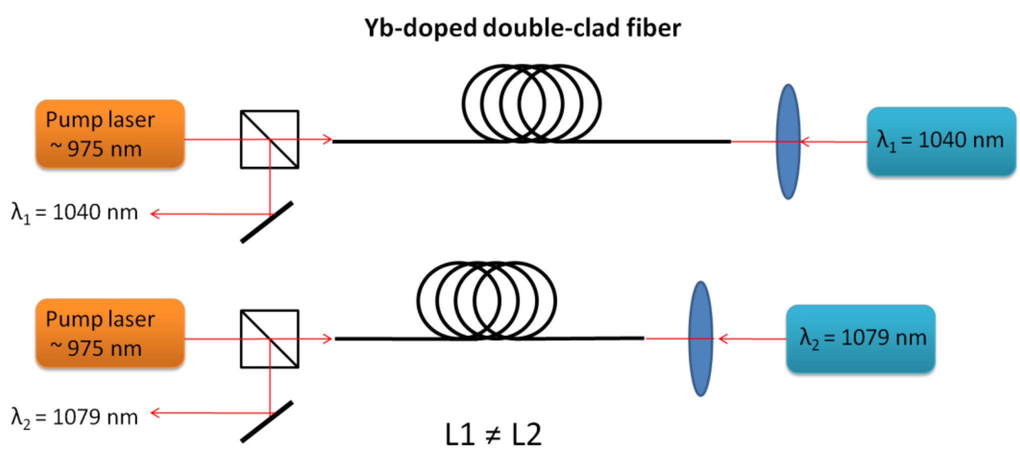

Figure 3-17 A schematic of the two-fiber amplifier system

the future experimental work, the simulation work could provide a first estimation of the value of the system.

The parameters of the fiber used in this section are same as those of prototype (Table 3-2). The input powers and wavelengths of seed beams and pump beams are shown in Table 3-13.

Table 3-13 Parameters used in the numerical simulations in Fig 16

	Wavelength	Power
Input seed beam 1	1040 nm	100 μW
Pump beam 1	~975 nm	2.109 W
Input seed beam 2	1079 nm	100 μW
Pump beam 2	~975 nm	2.109 W

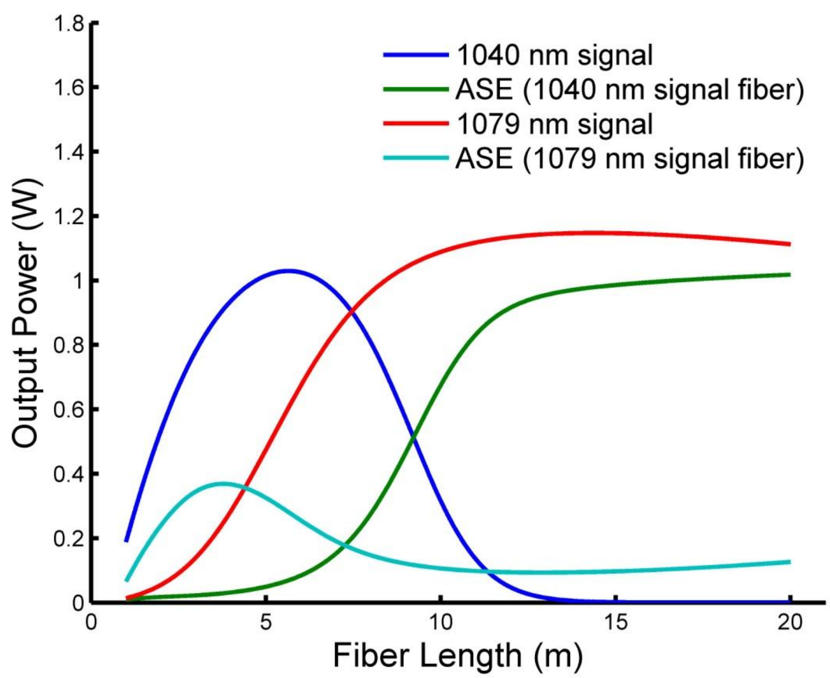

Figure 3-18 Signal output powers and ASE powers of both fibers versus fiber length for the seed beams at wavelengths of 1040 nm and 1079 nm.

Figure 3-18 shows the signal output powers and ASE powers of both fibers at different fiber lengths with seeding wavelengths of 1040 nm and 1079 nm. The dark blue curve represents the power of 1040 nm signal. The 1040 nm signal increases quickly with the length of the fiber when the fiber is short due to the large emission cross-section value and the small reabsorption. As the length of the fiber gets longer, the reabsorption effect becomes significant which make the output power of 1040 nm signal decrease. The green curve is the power of ASE in the 1040 nm signal fiber with the same direction as the signal. The counter-directional ASE is not included here. The ASE begins to rise when the signal power goes down. The red curve represents the power of the 1079 nm signal and the light blue curve is the ASE propagating in the same direction as the signal. The peak value of each signal and the corresponding ASE power is shown in Table 3-14. One can obtain an arbitrary output power in the available range. The maximum value of the intensity product of two seed beams is the product of two peak values of each signal power, which is 1.18 (W^2).

Table 3-14 Peak value of each signal and the corresponding ASE power of 1040 nm/1079 nm system

	1040 nm	1079 nm
Peak Value	1.03 W	1.15 W
Fiber Length	5.7 m	14.3 m
ASE	0.0842 W	0.0944 W

This software to simulate the two-fiber amplifier system is verified by two methods. First, one of the seed beams in the prototype is systematically decreased to zero. The results agree well with those in Figure 3-18. Second, the results are also verified by the simulator developed by M. Hajialamdari [42]. For the peak value of 1040 nm signal, the difference in the fiber lengths is 8% and the difference in the powers is 6%.

To obtain an equal output power of two seed beams, the maximum value in this case is shown in Table 3-15, which is the peak value of the 1040 nm signal power. The SNR in the table is the ratio of output power and the ASE. The length of the 1079 nm signal fiber at the output power of 1.03 W should have two values (the other is located at the other side of the peak value point). However, the longer length which has a same function as the shorter one is not discussed here.

Table 3-15 The maximum value of equal output seed beam powers in Fig 3-18

	1040 nm	1079 nm
Output power	1.03 W	1.03 W
Fiber Length	5.7 m	8.8 m
ASE	0.0842 W	0.125 W
SNR	12.23	8.24

To explore the values to the two-fiber amplifier system, a comparison with a single-fiber amplifier system of same total pump energy is made here. Figure 3-19 (a) shows the output power of each seed beam and the equidirectional ASE versus fiber length for the single-fiber amplifier system with the seed beams at wavelengths of 1040 nm and 1079 nm. The total pump power is 4.218 W, the same as the total pump power used in the two-fiber amplifier system. The optimal length is 7.51 m and the output powers at optimal length are shown in Table 3-16. The SNR in the table is the ratio of total output power of the seed beams and the backward ASE which propagates in the same direction as the seed beams. Figure 3-19 (b) shows the intensity product of the two output seed beams versus fiber length. The peak value is 1.36 (W^2) obtained at the fiber length of 7.4 m.

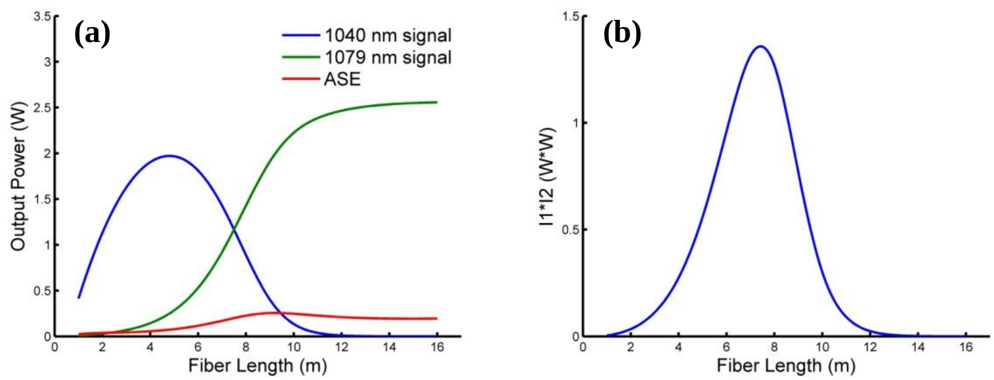

Figure 3-19 (a) The output power of each seed beam versus fiber length and (b) the product of two output seed beam intensities versus fiber length for the seed beams at wavelengths of 1040 nm and 1079 nm. The total pump power is 4.218 W.

Table 3-16 The output power of seed beams and ASE at optimal length (7.51 m)

	1040 nm	1079 nm	Backward ASE	Forward ASE
Power (W)	1.17	1.17	0.1999	0.2152
SNR	11.71	11.71	N/A	N/A

Comparing Table 3-15 with Table 3-16, one can conclude that the two-fiber amplifier system has no advantage in either the power of the output seed beams, the SNR or the intensity product of the two seed beams. However, the two-fiber amplifier system can provide arbitrary equal output powers under the maximum value, while the single-amplifier system can only obtain equal powers at the optimal length.

3.3 Two-stage Amplification System

In view of the potential difficulties of employing a two-fiber amplifier system for ultrafast difference frequency applications, a two-stage amplification system is introduced here to achieve a synchronized dual-wavelength laser source, in which the two output seed beams have equal powers. Al-Kadry *et al.* have used two 150 mW (before coupling) diode lasers operating at 976 nm as the pump sources at both fiber ends for preamplification and one 4 W (before coupling) diode laser operating at 975 nm for the second stage pump beam. A single clad YDFA is used for the preamplification and a double clad YDFA is used for the second stage amplification [2]. Hajialamdari *et al.* have recently used a two-stage amplification system using 1035 nm and 1105 nm seed signals with powers of 1.5 mW each. Each signal power is amplified to 5.75 mW and 11.5 mW for one-sided and two-sided pumping schemes respectively in the preamplification stage. The pump source is a diode laser operating at 976 nm with a power of 45 mW (after coupling) [1]. Both of their works seek an optimal length of the preamplifier, which makes the power of two output seed beams equal. Output seed beams with different energies were only briefly mentioned in their papers. In this thesis, using numerical simulation, the author reveals that the optimal length of the preamplifier should not be the length which makes the powers of the two output seed beams equal after the preamplification. Since the goal of this configuration is to obtain two equal output seed beams after the second stage, the optimal length of the preamplifier should maximize the final output powers but not aim to achieve equal output powers after the preamplification. The relationship between the length of the preamplifier and the final output seed beam powers, ASE, SNR will be discussed in detail.

The conceptual schematic of a two-stage amplification system is shown in Figure 3-20. The seed beams used here are 1040 nm and 1079 nm signals, which are the same as those in the prototype. The pump laser for the preamplifier has the

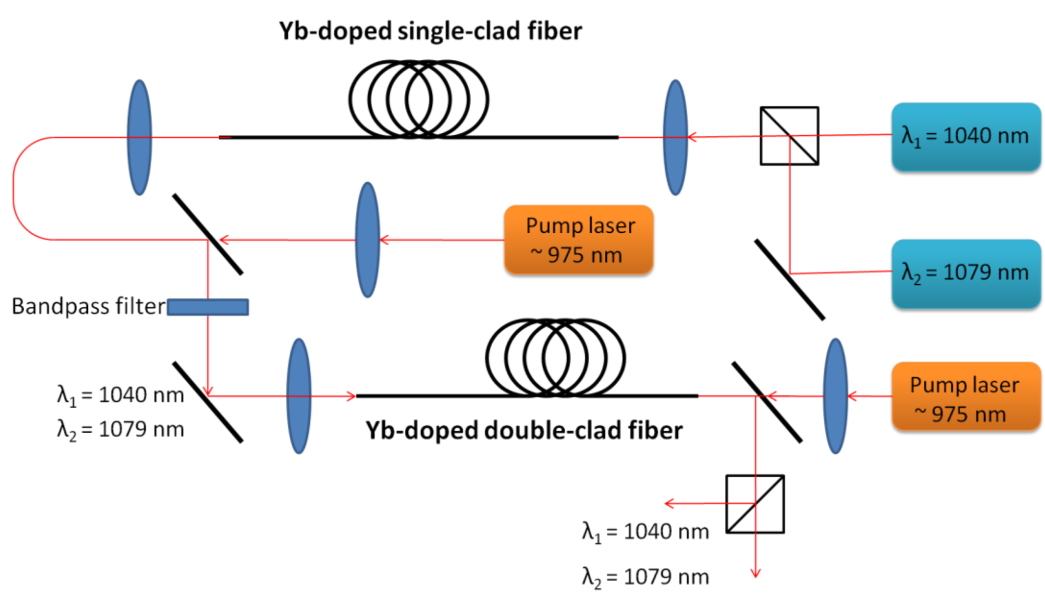

Figure 3-20 A schematic of the two-stage amplification system with one-sided pumping for both preamplifier and second stage amplifier

Table 3-17 Parameters used for the preamplification

	Wavelength	Power		Wavelengt	Power
Seed 1	1040 nm	100 μW	P_2	973.3 nm	11.1 mW
Seed 2	1079 nm	100 μW	P_3	974.5 nm	16.6 mW
Pump (total)	~975 nm	50 mW	P_4	975.5 nm	11.1 mW
P_1	972.6 nm	5.6 mW	P_5	976.3 nm	5.6 mW

Table 3-18 Parameters of single clad fibers used in the numerical simulations

Parameter	Value	Parameter	Value
core diameter	6 μm	λ_1(ASE)	1000 nm
cladding diameter	125 μm	λ_{101}(ASE)	1100 nm
N_T	8×10^{25} m^{-3}	$\Delta\lambda$	1 nm
α	9×10^{3} m^{-3}	Γ_s	0.87
τ	0.8 ms	Γ_{ASE}	0.87
A	2.827×10^{-11} m^2	D	0.87

same operating wavelength as the one in the prototype while the power coupled into the preamplifier is 50 mW (see Table 3-17). The preamplifier is a single clad YDFA. The parameters used for numerical simulation is shown in Table 3-18.

After being amplified by the preamplifier, the seed beams will pass through a bandpass filter (also called notch filter). The bandpass filter helps to eliminate some ASE but preserves the signal. A bandpass filter can be custom-made by many companies with a specified rejection band. In this thesis, the bandpass filter is assumed to have a rejection band between 1045 nm and 1075 nm. This rejection band can filter out a large amount of ASE while not affecting the signals.

The second stage of the configuration is the same as the prototype, except that the seed beams come from the output of the preamplification stage. Here, a fact that must be noted is that once the length of the preamplifier is fixed, the length of the second stage fiber must only be a certain value. This is due to the fact that a fixed length of the preamplifier can provide certain outputs of the seed beams, and then there must only be a specific length of the second stage in order to obtain equal final outputs with the preamplified beams inputs.

The pump power in Figure 3-20 could be variable. Therefore, Figure 3-20 can be considered as a conceptual configuration. It is named *Configuration (a).* Two-sided pumping can be applied to both the preamplification stage and the second amplification stage. If the two-sided pumping is used in the preamplification stage but not the second amplification stage, the configuration is named *Configuration (b),* as shown in Figure 3-21. If the two-sided pumping is used in the second amplification stage but not the preamplification stage, the configuration is named *Configuration (c),* as shown in Figure 3-22. If the two-sided pumping is used in both the preamplification stage and the second amplification stage, the configuration is named *Configuration (d),* as shown in Figure 3-23. The length of the preamplifier is referred to as L1 and the length of the second stage amplifier is referred to as L2. The powers of 1040 nm and 1079 nm signals are referred to as b1 and b2 respectively.

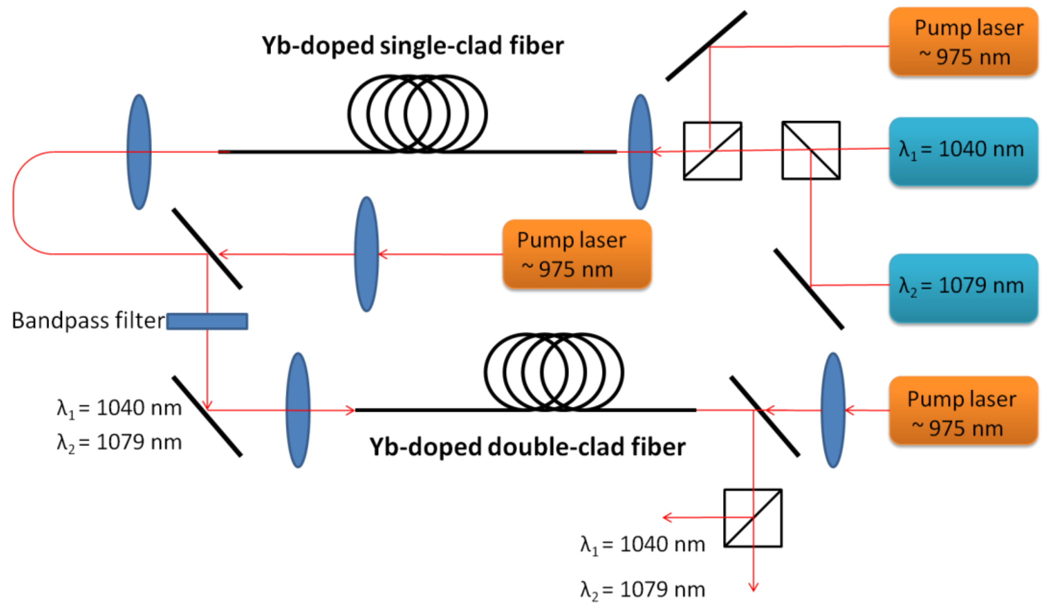

Figure 3-21 A schematic of the two-stage amplification system with two-sided pumping for preamplifier and one-sided pumping for second stage amplifier

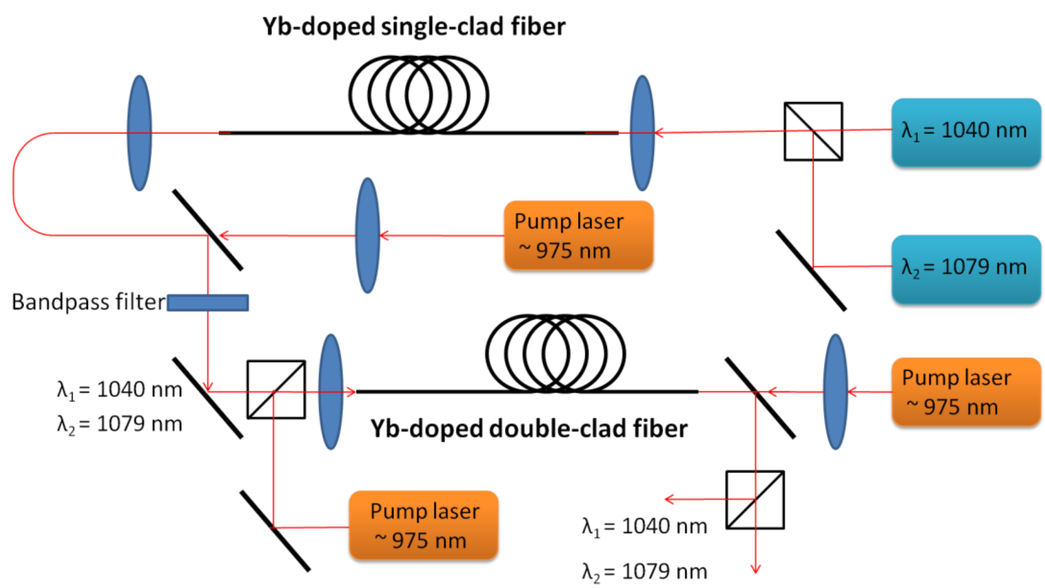

Figure 3-22 A schematic of the two-stage amplification system with one-sided pumping for preamplifier and two-sided pumping for second stage amplifier

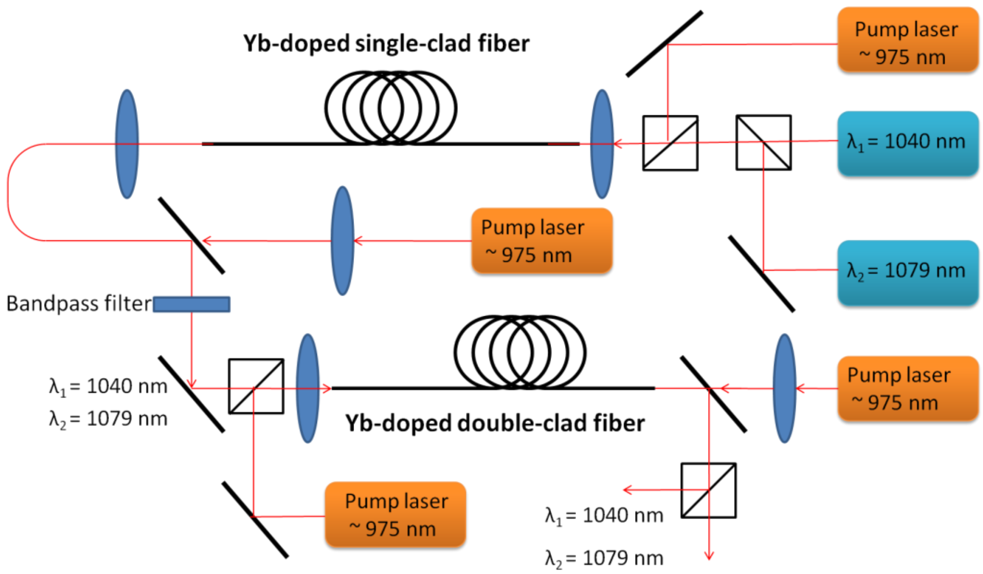

Figure 3-23 A schematic of the two-stage amplification system with two-sided pumping for both preamplifier and second stage amplifier

3.3.1 Verification of the Simulator for Single-clad Fiber

In this two-stage amplification system, the single-clad and double-clad fiber amplifiers are involved in the preamplification stage and second stage respectively. The simulator of double-clad fiber was verified by different methods as discussed earlier. The simulator for the single-clad fiber will be verified here. M. Hajialamdari *et al.* showed simulation results of the gain profile of an Yb-doped single-clad fiber amplifier versus the fiber length, with two input seed beams at wavelengths of 1035 nm and 1105 nm [1]. The simulation results in that paper agreed well with their experimental results. Figure 3-24 shows the results obtained by the simulator used in this thesis with the same parameters used in [1] with 3 mW input total seed power (both colors), which agrees well with the Figure 2 (c) shown in that paper. M. Hajialamdari *et al.* showed via simulation results that the 1035 nm and 1105 nm signal beams obtain equal output powers of 5.75 mW for each signal (in their single-clad fiber) at a fiber length of 1.4 m for one-sided pumping, and equal output powers of 11.5 mW for each signal at a fiber length of 2.7 m for two-sided pumping. The simulator used in this thesis gives a result of a 1.66 m length for one-sided pumping and an output signal power of 5.70 mW, and a 2.74 m length for two-sided pumping and an output signal power of 14 mW. Therefore, the simulator of single-clad fiber used in this thesis agrees well with the independent work of M. Hajialamdari *et al.* The small difference between the two figures could be caused by the spectra of input seed beams and the values of the absorption and emission cross-sections. The spectra of input signals in [1] were extracted from their experimental work. The spectra of two

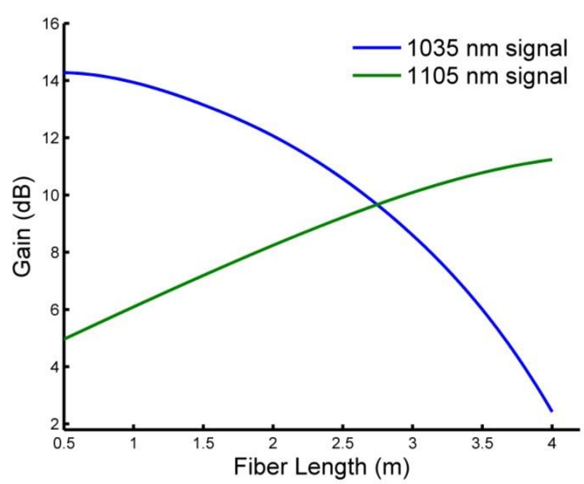

Figure 3-24 Simulation of gain profile of the preamplifier versus fiber length with seed beams at wavelengths of 1035 nm and 1105 nm.

seed beams extended from 1020 nm to 1042 nm and from 1101 nm to 1118 nm, with central wavelengths at 1035 nm and 1105 nm, respectively. The spectra of input signals used in this thesis are taken as monochromatic as in the previous work.

3.3.2 Results of the Two-stage Amplification System

Using all the simulators, one can reveal the relationship between the length of the preamplifier, the pump power and the final output power. In this section, nine cases are studied. For clarity, the nine cases are labelled A to I as shown in Table 3-19. The pump power with a single value in the table (e.g. 50 mW, 2.109 W) means only one-sided pumping is applied and the pump beam propagates counter-directionally to the seed beams. The pump power consisting of two values in the table (e.g. 50 mW+50 mW, 2.109 W+2.109 W) means two-sided pumping is applied. Cases A, B and C are all one-sided pumped at the preamplifier stage while the second stage pumping arrangements are different. The 2.109 W+2.109 W two-sided pumping has a same total pump power as the 4.218 W one sided pumping. All the powers indicate the values that are actually coupled into the fiber. For all the configurations, equal output powers of two seed beams are expected after the second stage amplification.

Table 3-19 Pump powers used in all the cases

Cases	Preamplifier pump power (mW)	Amplifier pump power (W)	Corresponding configuration
A	50	2.109	(a)
B	50	2.109+2.109	(c)
C	50	4.218	(a)
D	50+50	2.109	(b)
E	50+50	2.109+2.109	(d)
F	50+50	4.218	(b)
G	100	2.109	(a)
H	100	2.109+2.109	(c)
I	100	4.218	(a)

Case A is studied in detail here. Figure 3-25 shows the power distribution of the amplified signals, pump beam and ASE in a 1.19 m-long-preamplifier (single-clad fiber) which leads to the two output signals having equal powers. The pump beam with a power of 50 mW, is one-sided, and propagates counter-directional to the seed beams. As seen in Figure 3-25 (a), the pump beam is rapidly absorbed at the beginning and is almost zero after 0.2 m. This is due to the high absorption exhibited by the single-clad fiber, which is very different from double-clad fiber. Thus the population inversion contributed by the pump beam after 0.2 m is almost zero. From the zoomed-in figure (b), one can tell that the signals are decreasing before they reach the 0.2 m point, from which the fiber provides signal gain. The

ASE with the same direction as the signals also rises from the 0.2 m point. Therefore, reducing the preamplifier length could improve the efficiency of the whole system and use less fiber. Figure 3-25 (b) indicates that the 1040 nm signal loses power faster along the fiber length than the 1079 nm signal when there is no gain but it grows faster in the pumped region of the fiber. The mechanism behind this phenomenon is discussed in section 3.1.

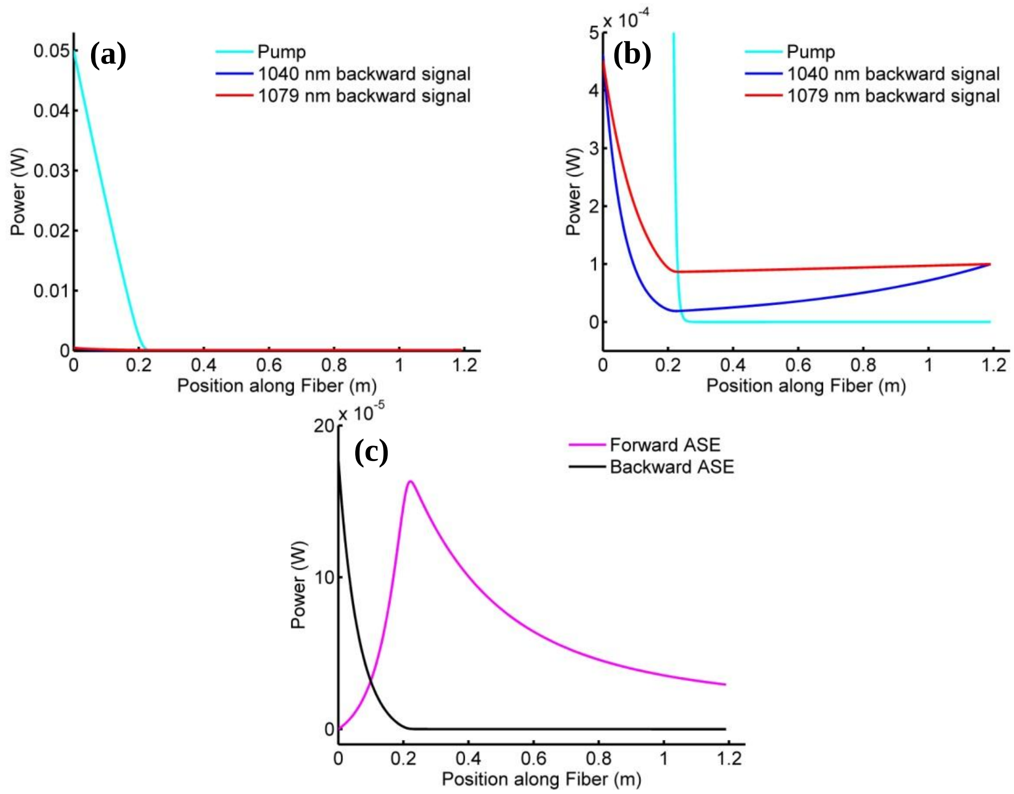

Figure 3-25 Power distribution of (a) the amplified signals and pump, (b) zoomed-in figure for the seed beams in (a), and (c) the ASE in the preamplifier inside a preamplifier (single-clad fiber) with a length of 1.19 m. The pump power is 50 mW.

Figure 3-26 shows the powers of signal beams and ASE at different preamplifier lengths. The power of the 1040 nm signal increases when the fiber length is shorter, which means that less energy lost for 1040 nm signal before it is amplified. The output power of the 1079 nm signal is rather stable when the fiber length changes. It is in good agreement with Figure 3-25, which shows almost no energy being lost before the amplification section. The power of the 1040 nm signal reaches a peak value at the fiber length of 0.2 m. If the fiber length is less than 0.2 m, the pump energy will not be sufficiently absorbed and thus will not result in an efficient amplification.

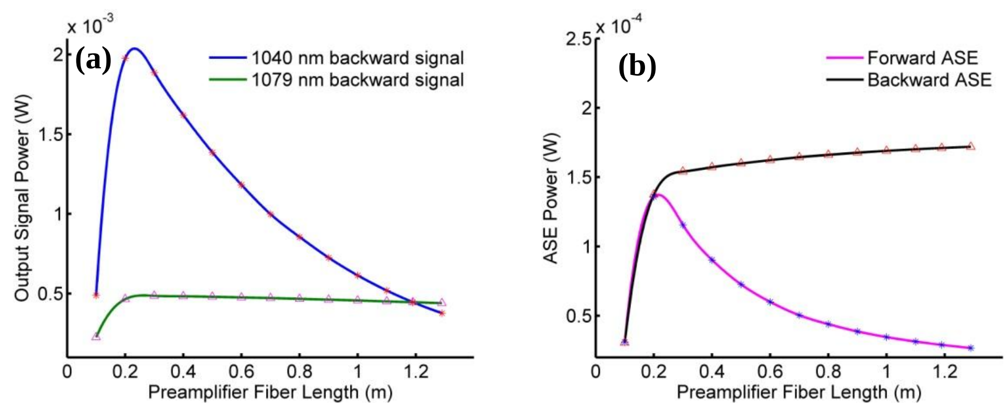

Figure 3-26 Signal output powers and ASE powers of both fibers versus preamplifier length for the one-sided pumping with a power of 50 mW.

Figure 3-27 shows the relationship between the preamplifier length and the power of the output seed beam, ASE, SNR, and the length of second stage fiber amplifier for case A. The input seed powers of the second stage are the preamplified signals from the preamplifier. Since the final output seed beams have equal powers after the second stage amplification, the blue curve in the figure indicates the output power of only one signal (the other one has the same power). The ASE curve indicates the ASE which propagates in the same direction as the signals. The SNR is the ratio of the total seed beam output power (the total power of two signals) and the ASE. The power of the ASE has an opposite trend to the power of the output seed beam while the SNR follows a similar trend. The SNR also reaches a peak value at the fiber length of 0.2 m. Figure 3-27 (c) shows that the length of the preamplifier and the second stage amplifier exhibit roughly a linear relationship. When the length of preamplifier is shortened, the length of the second stage amplifier is extended as a kind of compensation.

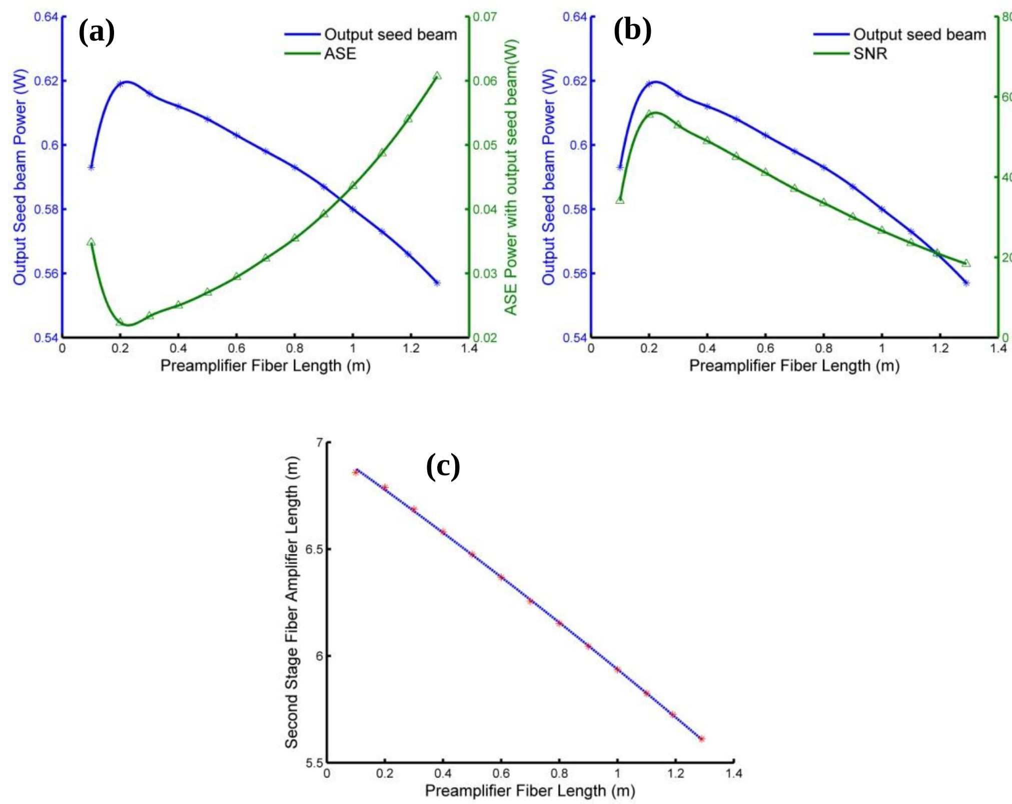

Figure 3-27 In case A, the relationship between the preamplifier length and (a) the power of output seed beam and ASE (b) output seed beam power and SNR, and (c) the length of second stage fiber amplifier. The output seed beam power is the seed beam power after second stage amplifier.

Table 3-20 shows all of the data at two benchmark points. When the length of preamplifier is 1.19 m, the output powers of the two signals after the preamplifier are equal. When the length of the preamplifier is 0.20 m, the final signal output powers reach the maximum value and the largest SNR is achieved.

Table 3-20 Data for the preamplifier lengths of 1.19 and 0.20 m in case A

Single-clad YDFA L1 (m)	Double-clad YDFA L2 (m)	Output seed beam power (W) (each)	ASE (backward) (W)	Signal to noise ratio (SNR)
1.19 (b1=b2)	5.726	0.566	0.0540	20.96
0.20	6.789	0.619	0.0223	55.52

The SNR indicates the ratio of the total output signal powers and the ASE power. Since the wavelength range of the ASE is from 1000 nm to 1100 nm, some wavelengths of ASE can be easily removed by a filter. Therefore, a new parameter is defined here, "Modified Signal to Noise Ratio (MSNR)". In this configuration, only two bands of noise remain in the 1035-1045 nm and 1075-1085 nm wavelength ranges. The signals can pass through the filter without attenuation and thus the output signal power remains the same. The residual ASE power is named the "Modified Amplified Spontaneous Emission (MASE)". Figure 3-28 (a) and (b) shows the relationship between the length of the preamplifier and the power of the output seed beam, MASE and MSNR. Figure 3-28 (c) and (d) clearly shows that a bandpass filter considerably improves the ASE and SNR. Table 3-21 provides the data for the ASE, MASE, SNR and MSNR at the preamplifier lengths of 1.19 m and 0.20 m.

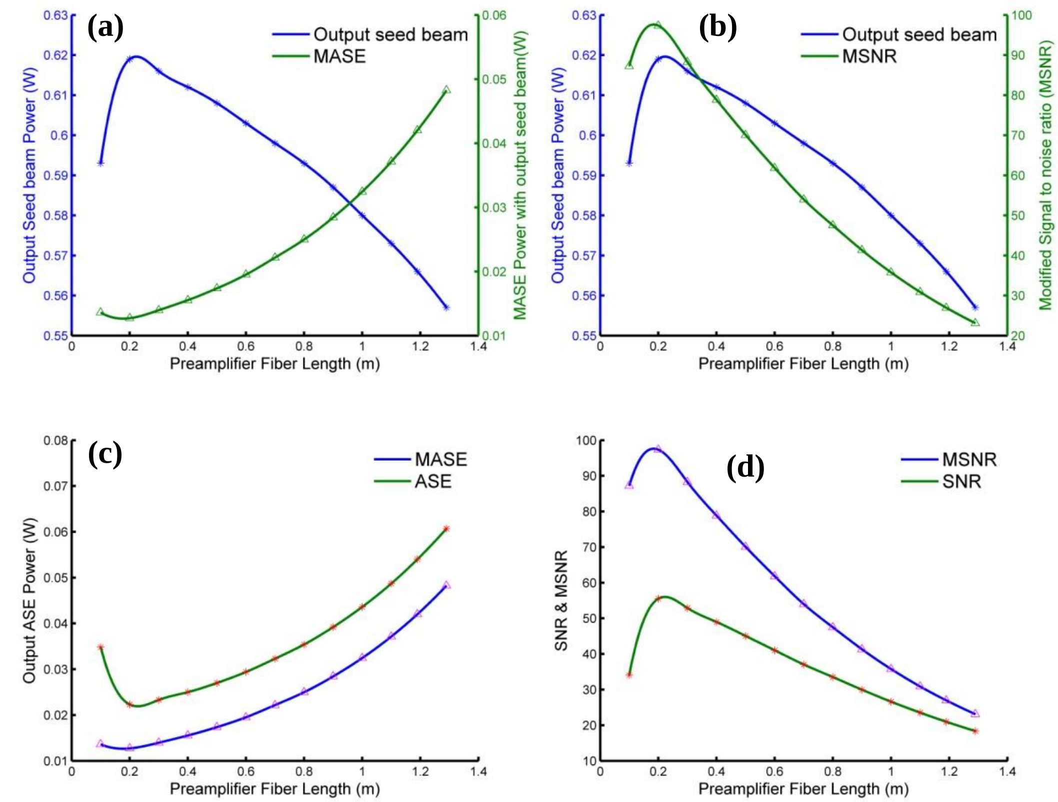

Figure 3-28 In case A, the relationship between the preamplifier length and (a) the power of output seed beam and MASE (b) output seed beam power and MSNR (c) ASE and MASE, and (d) MSNR and SNR

Table 3-21 Data for the preamplifier lengths of 1.19 m and 0.20 m in case A

Single-clad YDFA L1 (m)	ASE (backward) (W)	MASE (backward) (W)	Signal to noise ratio (SNR)	MSNR
1.19 (b1=b2)	0.0540	0.0420	20.96	26.95
0.20	0.0223	0.0127	55.52	97.33

For cases B to I, the trends of the preamplifier fiber length versus the power of output seed beam, ASE, MASE, SNR and MSNR are similar to case A, except that the values vary depending on the pump powers. The relationship between the length of preamplifier (L1) and the length of second stage amplifier (L2) stays linear from case B to I, the same as case A. Table 3-22 shows the data for cases A to I. The first preamplifier length for each case makes the output powers of two signals equal after the preamplification stage. The second preamplifier length for each case makes the whole system obtain maximum output signal powers after the second amplification stage.

Table 3-22 Comparison of cases A to I. The first preamplifier length for each case makes the output powers of the two signals equal after the preamplification stage. The second preamplifier length for each case makes the whole system obtain maximum output signal powers after the second amplification stage.

Case No.	Preamplifier Length (m)	Final Output Power (W) (each)	SNR	MSNR
A	1.19	0.566	20.96	26.95
	0.20	0.619	55.52	97.33
B	1.19	1.233	21.78	27.48
	0.20	1.331	60.23	101.22
C	1.19	1.255	21.04	27.07
	0.20	1.353	56.14	98.69
D	1.86	0.570	43.02	55.07
	0.30	0.637	71.17	100.39
E	1.86	1.253	44.43	55.93
	0.30	1.359	75.29	102.14
F	1.86	1.268	43.57	55.46
	0.30	1.379	72.77	101.32
G	2.26	0.494	6.285	6.871
	0.40	0.645	72.07	93.48
H	2.26	1.095	6.47	6.88
	0.40	1.368	74.96	94.70
I	2.26	1.105	6.47	6.88
	0.40	1.388	73.44	94.26

3.3.3 Conclusion

From all the simulation results demonstrated in section 3.3.2, some conclusions can be made.

First, the preamplifier fiber length which leads to the two seed beams obtaining equal output powers after the preamplification stage is not the optimal length for the two-stage system in terms of achieving a maximum final equal output power. The optimal length to obtain a maximum final equal output power is approximately equal to the length which can fully absorb the pump beam (e.g. the optimal length for 50 mW pre-pump system in this thesis is about 0.20 m, the optimal length for 50+50 mW and 100 mW pre-pump system is about 0.30-0.40 m). Table 3-22 shows their comparisons of final output power, SNR and MSNR.

Second, the final output power of the signals is determined largely by the second stage pump power. The pump power of the preamplification stage cannot significantly change the final output power of the signals, but it can substantially change the SNR.

Table 3-23 clearly shows the relationship between the pump powers of each stage and output powers, SNR, MSNR. The configurations A, D and G have a similar final output power, while the others also have a similar output power. Meanwhile, the configurations A, D and G have a same pump power in the second stage. Configurations B, E and H have a same total pump power in the

Table 3-23 Comparison of final output powers, SNR and MSNR for each case. The fiber length of first stage for each case are different. The fiber lengths are shown in Table 3-22.

Case No.	First stage pump power (mW)	Second stage pump power (W)	Maximum final output power (W)	SNR	MSNR
A	50	2.109	0.619	55.52	99.73
B	50	2.109+2.109	1.331	60.23	101.22
C	50	4.218	1.353	56.14	98.69
D	50+50	2.109	0.637	71.17	100.39
E	50+50	2.109+2.109	1.359	75.29	102.14
F	50+50	4.218	1.379	72.77	101.32
G	100	2.109	0.645	72.07	93.48
H	100	2.109+2.109	1.368	74.96	94.70
I	100	4.218	1.388	73.44	94.26

second stage as configurations C, F and I, although their pumping methods are different. These results show that the final output power of signals is largely determined by the second stage pump power. However, the first stage pump power is related to the final SNR. The configurations A, B and C have a similar SNR while the others have another similar value.

The physical principles of the relationship between the first stage and the second stage are still under investigation. However, some speculations are discussed in chapter 5.

3.4 Nonlinear Effects

As it was discussed in Chapter 2.5, the nonlinear effects which occur in optical fibers can be classified into two categories. The first category includes stimulated Raman scattering (SRS) and stimulated Brillouin scattering (SBS), both of which are nonlinear inelastic scattering process. In this section, the threshold power of SRS and SBS will be discussed. The second category includes self-phase modulation (SPM), cross-phase modulation (XPM) and four-wave mixing (FWM). The maximum phase shift of pulses due to SPM and XPM, and the powers of the new frequencies generated by FWM will be calculated in this section. To estimate the value of each effect, the values of all the parameters used in the following sections are only approximate values within a reasonable order of magnitude.

3.4.1 Threshold of Stimulated Raman Scattering (SRS)

In a typical dual-wavelength fiber amplifier system, the fiber length L is assumed to be around 6 m and the background attenuation coefficient α used in the numerical model is 9×10^{-3} m^{-1}. Therefore, according to Equation (2-15), the effective length of this fiber is

$$\begin{aligned} L_{eff} &= [1-\exp(-\alpha L)]/\alpha \\ &= [1-\exp(-9\times10^{-3}\ m^{-1}\times 6\ m)]/(9\times10^{-3}\ m^{-1}) = 5.84\ m \end{aligned} \tag{3-1}$$

The Raman-gain coefficient g_R is about 1×10^{-13} m/W for silica fibers near 1 μm and the effective mode area A_{eff} is around 50 μm^2 [26] [27]. Thus, according to Equation (2-14), the threshold power for SRS is about

$$P_{th(SRS)} \approx \frac{16A_{eff}}{g_R L_{eff}} = \frac{16\times(50\times10^{-12}m^2)}{1\times10^{-13}m/W\times5.84m} = 1370\,W \tag{3-2}$$

Therefore, the SRS effect can be neglected in the dual-wavelength fiber amplifier system in this thesis.

3.4.2 Threshold of Stimulated Brillouin Scattering (SBS)

The Brillouin-gain coefficient g_B is about 4×10^{-11} m/W for silica fibers [15]. Thus, according to Equation (2-14), the threshold power for SBS is about

$$P_{th(SBS)} \approx \frac{21A_{eff}}{g_B L_{eff}} = \frac{21\times(50\times10^{-12}m^2)}{4\times10^{-11}m/W\times5.84m} = 4.5\,W \tag{3-3}$$

Therefore, SBS could limit the launched power due to its low threshold which has a same order as the powers in the prototype model. However, the threshold power can be increased considerably by increasing the gain bandwidth through phase modulation, since the Brillouin-gain spectrum for silica fibers is quite narrow [26].

3.4.3 The Maximum Phase Shift due to Self-phase Modulation (SPM) and Cross-phase Modulation (XPM)

In the prototype model, the powers of signals are amplified to about 0.5 W each, and the nonlinear parameter γ for Yb-doped fibers is about 5.8×10^{-3} W^{-1}/m [44] [45]. Therefore, according to Equation (2-19), the maximum phase shift for a single signal due to SPM is

$$\begin{aligned}\phi_{\max(SPM)} &= \gamma P_0 L_{eff} \\ &= 5.8\times10^{-3}\,W^{-1}/m\times0.5\,W\times5.84\,m \\ &= 0.017\end{aligned} \tag{3-4}$$

According to Equation (2-21), the maximum phase shift for a single signal due to SPM and XPM together is

$$\begin{aligned}\phi_{\max(SPM\,\&\,XPM)} &= \gamma L_{eff}(P_1+2P_2) \\ &= 5.8\times10^{-3}\,W^{-1}/m\times5.84\,m\times(0.5\,W+2\times0.5\,W) \\ &= 0.051\end{aligned} \tag{3-5}$$

The maximum phase shift due to SPM and XPM increases with the output powers. Therefore, the maximum output powers in some applications could be constrained by SPM and XPM.

3.4.4 New Frequencies Generated by FWM

The two signal wavelengths used in the prototype are 1040 nm and 1079 nm. Therefore, according to section 2.5.4, the new frequencies generated due to FWM are at

$$\begin{aligned} \nu_3 &= 2\nu_1 - \nu_2 = 2\frac{c}{\lambda_1} - \frac{c}{\lambda_2} \\ &= 2\times\frac{3\times10^8\ m/s}{1040\times10^{-9}\ m} - \frac{3\times10^8\ m/s}{1079\times10^{-9}\ m} = 2.99\times10^{14}\ Hz \end{aligned} \tag{3-6}$$

and

$$\begin{aligned} \nu_4 &= 2\nu_2 - \nu_1 = 2\frac{c}{\lambda_2} - \frac{c}{\lambda_1} \\ &= 2\times\frac{3\times10^8\ m/s}{1079\times10^{-9}\ m} - \frac{3\times10^8\ m/s}{1040\times10^{-9}\ m} = 2.68\times10^{14}\ Hz \end{aligned} \tag{3-7}$$

The wavelengths of these new generated waves are

$$\lambda_3 = \frac{c}{\nu_3} = \frac{3\times10^8\ m/s}{2.99\times10^{14}\ Hz} = 1003\, nm \tag{3-8}$$

and

$$\lambda_4 = \frac{c}{\nu_4} = \frac{3\times10^8\ m/s}{2.68\times10^{14}\ Hz} = 1119\, nm \tag{3-9}$$

The channel spacing (39 nm) in frequency of two original signals is

$$\begin{aligned}\Delta\nu &= \nu_1 - \nu_2 = \frac{c}{\lambda_1} - \frac{c}{\lambda_2} \\ &= \frac{3\times10^8\ m/s}{1040\times10^{-9}\ m} - \frac{3\times10^8\ m/s}{1079\times10^{-9}\ m} = 1.04\times10^{13}\ Hz = 10400\,GHz\end{aligned} \tag{3-10}$$

According to Figure 12-33 in [15] and Equation 6 in [46], the four-wave mixing efficiency η is nearly 0 when the channel spacing is 10400 GHz. Therefore, according to Equation (2-26), the powers of these new generated waves are nearly zero.

Chapter 4 Electron Microscopy Study of Single Ytterbium Atoms in Doped Optical Fibers

As introduced in chapter 1 and described further in this chapter, the distribution of ytterbium (Yb) atoms is being investigated in a range of double-clad Yb-doped fibers. Using a scanning transmission electron microscope (STEM), single Yb atoms are expected to be observed directly from the TEM samples prepared from Yb-doped optical fibers.

The STEM technique has been proved to be the most efficient method to study single atoms on the surface and in the bulk [47-50]. The first successful application of the High Angle Annular Dark Field (HAADF) technique on heavy atoms (U and Th) lying on the carbon film was reported by Crewe in 1970 [47]. The more challenging work of detecting single atoms inside the bulk (highly Sb-doped Si) was achieved with the same technique by P. M. Voyles *et al.* [48] . Recently, K.V. Benthem *et al.* have used an atomic resolution STEM to obtain detailed information about both nanoscale Pd catalyst particles and single Pd atoms in activated carbon fibers (ACFs) [49]. At the Canadian Centre for Electron Microscopy, McMaster University, M. Couillard *et. al* observed single Ce atoms in Si [50].

The main challenge of detecting single atoms in the present project is the sample preparation. The normal preparation methods require a specimen with the dimension of roughly $1\times1\times1$ mm^3. However, the original materials used in this thesis are optical fibers with diameters about 125 μm. Additionally, the thin area observed in TEM must be located within the core area, which is usually only a few micrometers in diameter. In this chapter, challenges related to sample preparation and the interpretation of images will be discussed, in addition to that, the approach shows great potential to investigate the doping behaviors down to the atomic scale in the fibers. The work is expected to help elucidate mechanisms affecting the performance of doped fibers, such as photodarkening, which is due possibly to clustering effects.

4.1 In Situ Lift-out Using a FIB-SEM System

4.1.1 Fiber#1

The first fiber prepared by the in situ lift-out method is named Fiber#1. The main parameters of Fiber#1 are shown in Table 4-1. The fiber was provided by CorActive High-Tech Inc. TEM specimens were made from both photodarkened and pristine pieces of Fiber#1.

Table 4-1 Parameters of Fiber#1

Double clad optical fiber	
Core diameter	3.67 μm
Cladding diameter	125 μm
Ytterbium concentration	2.09×10^{26} ions/m^3
core absorption @ 915 nm	509 dB/m
core absorption @ 974 nm	1568 dB/m
numerical aperture (NA)	0.17
background loss	16 dB/km

(a) Darkened Fiber#1

The first TEM specimen was made from a piece of photodarkened Fiber#1. The thin slice shown in Figure 4-1 is the sample processed by the focused ion beam (FIB). The white part in the figure indicated by a red arrow is the thin slice. The

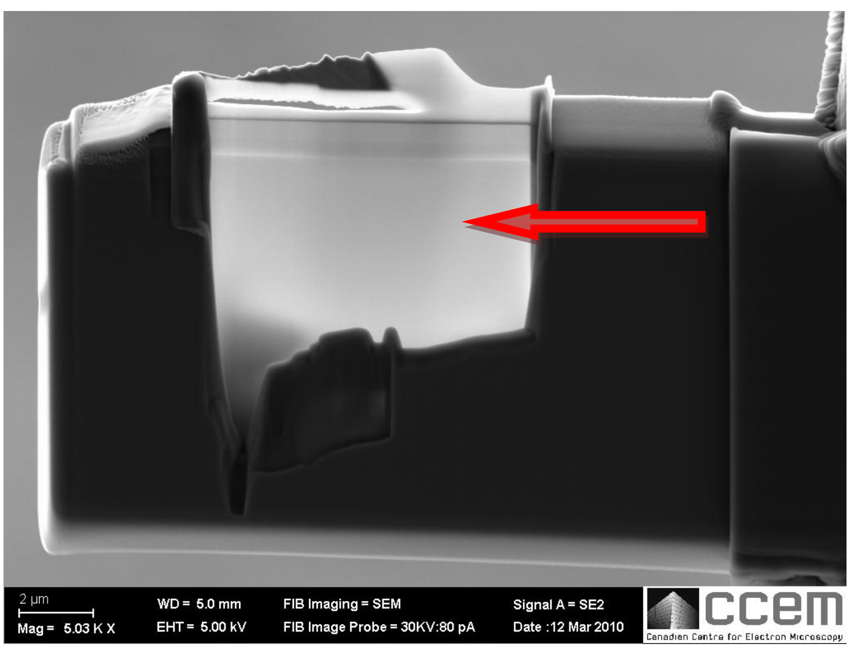

Figure 4-1 Darkened Fiber#1 TEM specimen made by in situ lift-out method

color difference between the slice (white) and the other part (black) reflects the difference in the thickness. This figure is also a side sectional view of Figure 2-9 (c) and (d).

This thin slice was put on a TEM grid which is specially made to hold TEM samples fabricated via the in situ lift-out method. The thickness of TEM sample is estimated to be about 60 nm.

Figure 4-2 shows the EDS spectrum of the fiber used above. The black line shows the EDS spectrum of the fiber core area while the red line indicates that of the cladding area. The Si and O signals come from the fiber host, SiO_2. The Cu signals come from the copper grid holder supporting the TEM specimen of the fiber. The Ga signal is introduced by the Ga^{3+} ion beam (the ion source in the FIB system) during ion milling to prepare the TEM specimen. The only difference in the two spectra is the detectable signal from Yb elements within the core area, which will result from the dominating contrast in STEM-HAADF image on account of its larger atomic number, *Z*.

Figure 4-3 shows the STEM-HAADF (Z contrast image) micrograph for the sample prepared from photodarkened Fiber#1. According to the "Z contrast" imaging theory, the brightness of each dot on the STEM-HAADF image roughly scales as the atomic number $Z^{1.7}$ [41]. Under the reasonable assumption of a flat observed area within the field of view at such high magnitude, a conclusion can be made that the bright spots on the micrographs represent Yb atoms because the

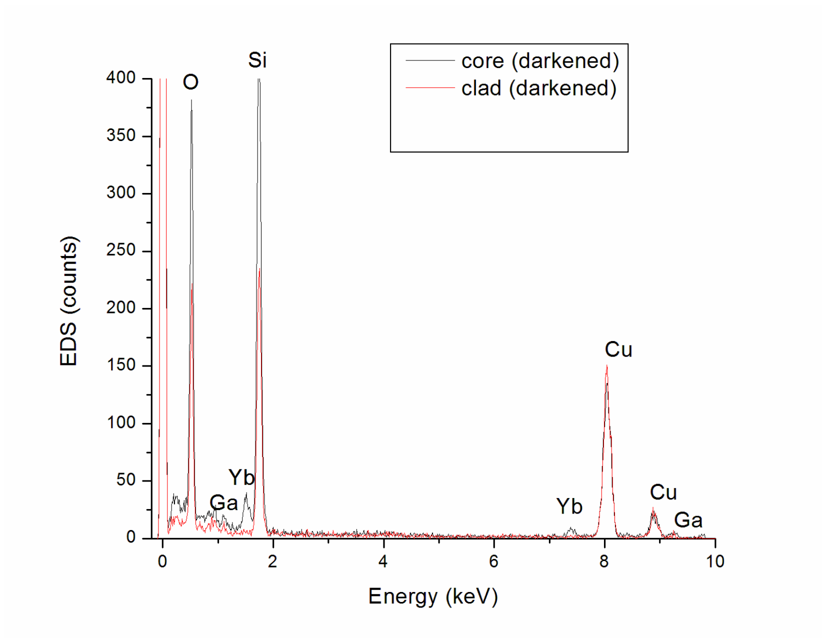

Figure 4-2 EDS spectra for specimen prepared with photodarkened Fiber#1

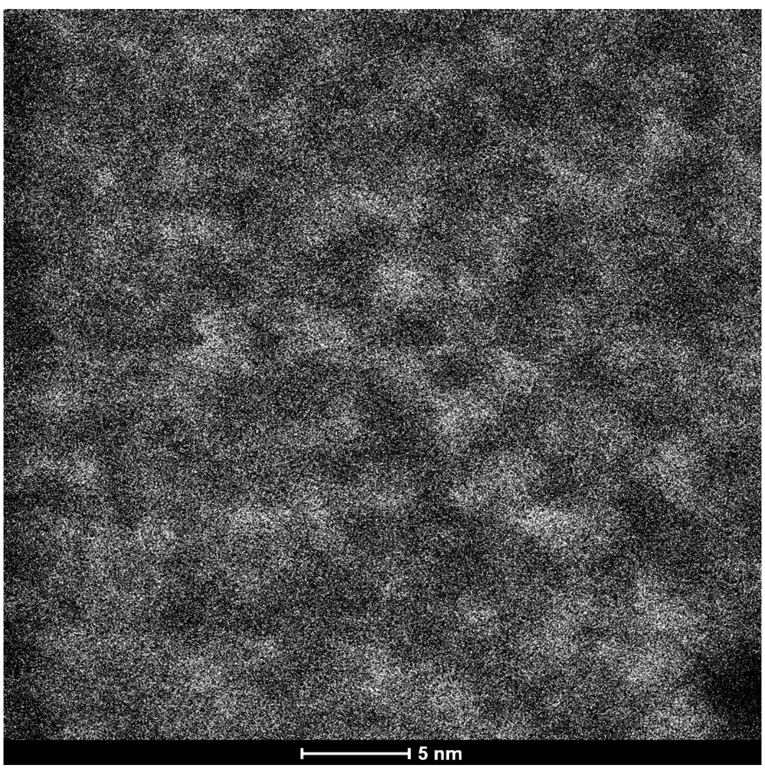

Figure 4-3 STEM micrographs for specimen prepared with photodarkened Fiber#1

Yb atom species is the only heavy atom in the core (the atomic numbers of other elements are much less than Yb). Figure 4-3 shows that the Yb atoms are distributed nonuniformly in the observation area. Some atoms tend to cluster together while some are randomly distributed throughout the core.

The estimated thickness of a TEM sample made by the focused ion beam in situ lift-out method is about 60 nm. The theoretical number of Yb atoms in Figure 4-3 is shown in Table 4-2.

Table 4-2 The calculated results of Figure 4-3

estimated thickness	60 nm
observation area	1272 nm^2
entire volume	76,320 nm^3
doping density	2.09×10^{26} ions/m^3
theoretical Yb atom number	16,000 ions

(b) Pristine Fiber#1

Figure 4-4 shows the second sample of Fiber#1 made from a piece of pristine fiber. The thickness is also estimated to be 60 nm. The EDS spectrum for this sample is similar to that of the last one, Figure 4-2.

Figure 4-5 shows the STEM-HAADF micrograph for the sample prepared from the pristine Fiber#1. The bright spots on the figure represent the heavy Yb atoms in the observation area. The theoretical numbers of Yb atoms in Figure 4-5 are shown in Table 4-3.

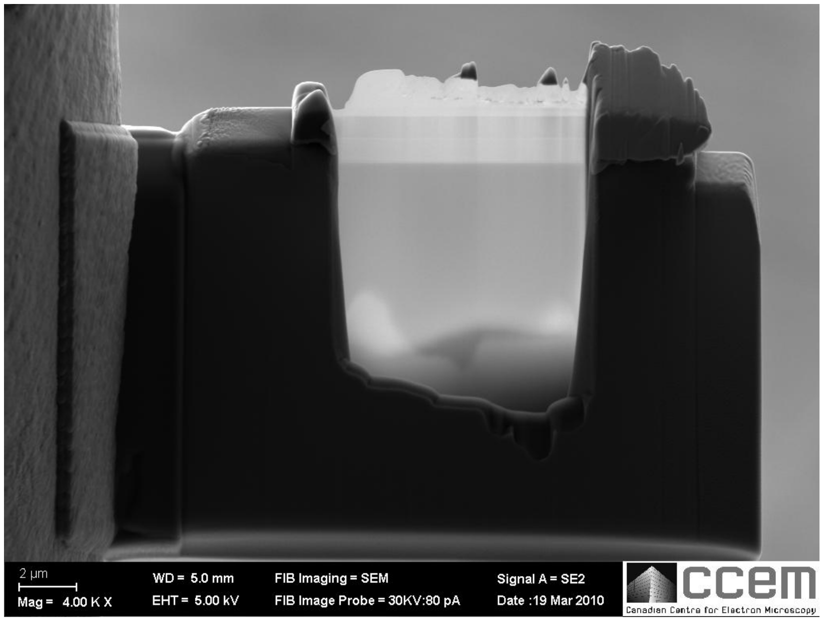

Figure 4-4 Pristine Fiber#1 TEM specimen made by in situ lift-out method

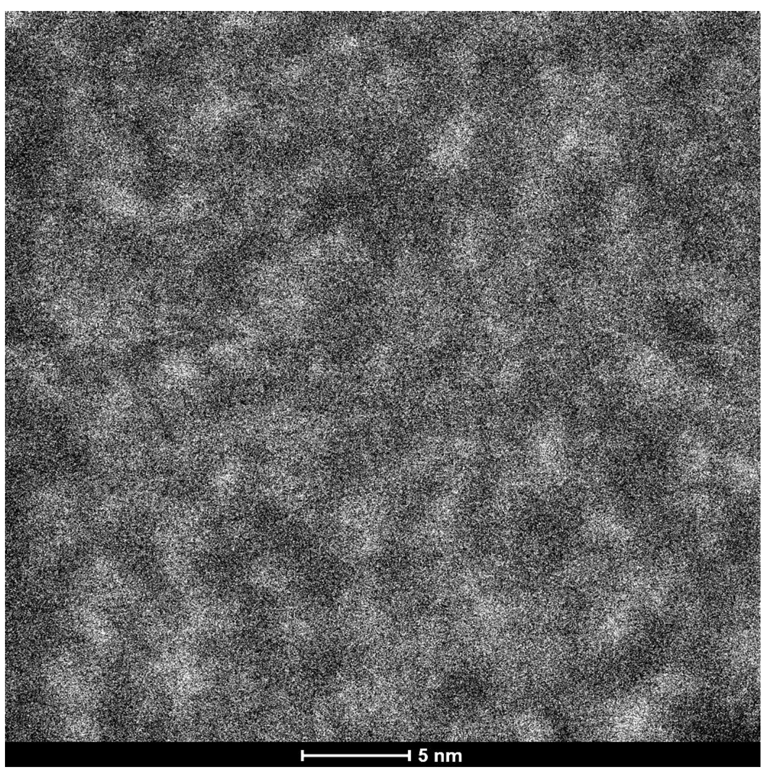

Figure 4-5 STEM micrographs for specimen prepared with pristine Fiber#1

Table 4-3 The calculated results of Figure 4-5

estimated thickness	60 nm
observation area	1272 nm^2
entire volume	76,320 nm^3
doping density	2.09×10^{26} $ions/m^3$
theoretical Yb atom number	16,000 ions

Comparing Figure 4-5, the pristine fiber sample, with Figure 4-3, the photodarkened fiber sample, the distribution of Yb atoms is similar, with some atoms having a tendency to cluster. There is no significant difference observed between micrographs of the pristine fiber and the photodarkened fiber.

Figure 4-6 shows the bright field (BF) STEM micrographs of pristine Fiber#1. STEM-BF micrographs are more sensitive to the periodic structure of the specimens. The principle of STEM-BF was introduced in section 2.7.4. The STEM-BF images are usually used as the compensative images for STEM-HAADF images, which implies that the black dots in BF have a high possibility to be the bright dots in HAADF. However, some clustered black spots on Figure 4-6 which usually cannot be observed in STEM-BF micrographs are regularly organized and the image seems to contain some information about the sample. The BF STEM micrographs with clustered black spots are shown here as a historical record of our work for potential future interpretation.

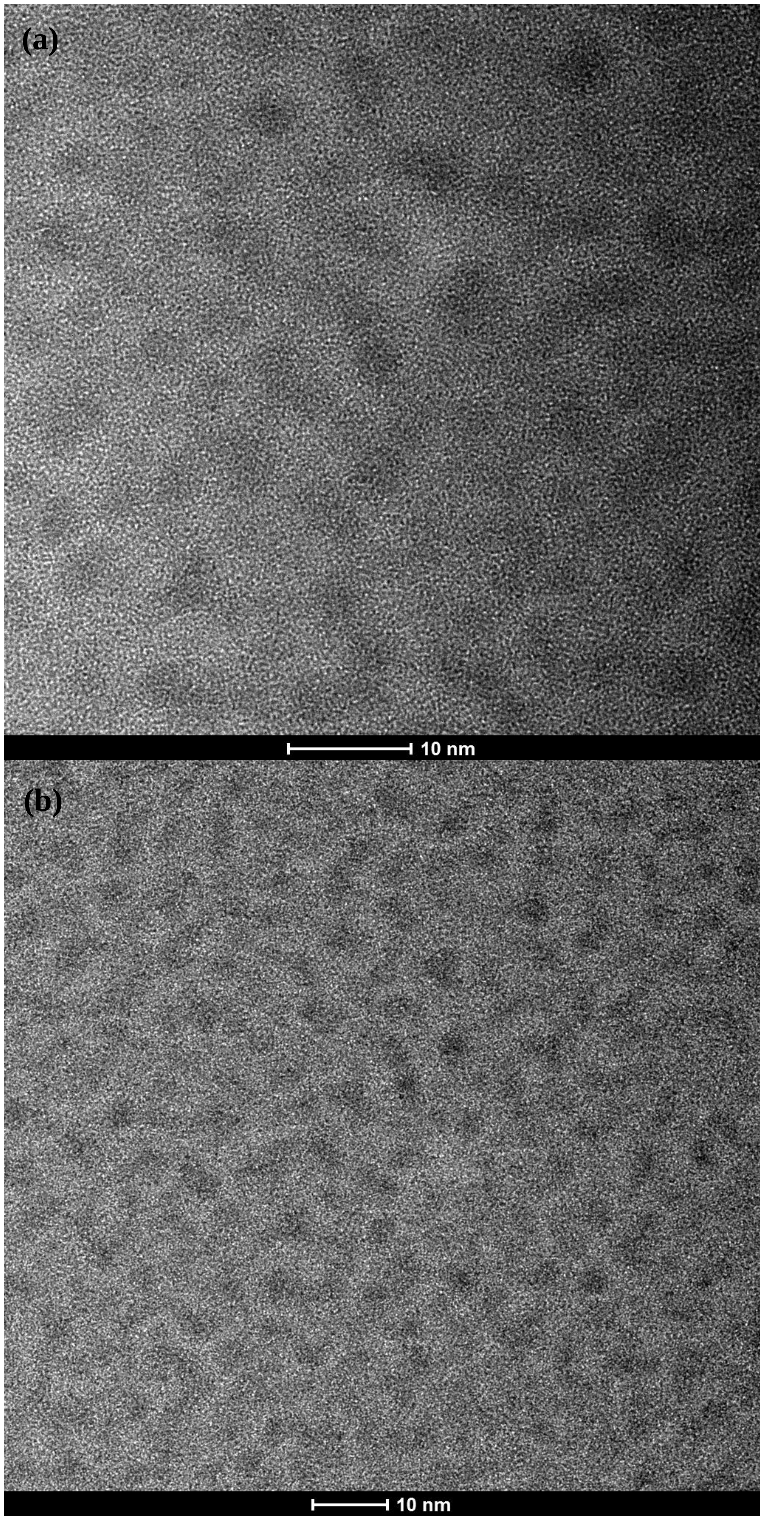

Figure 4-6 (a) and (b) BF STEM micrographs for specimen prepared with pristine Fiber#1

(c) Thinner Pristine Fiber#1

A problem encountered in both of the above micrographs is the resolution. Higher resolution micrographs are required to obtain more details about the distribution of single Yb atoms. Since all TEM micrographs are the 2D projections of 3D objects, the thin specimens are required in order to avoid the vertical distribution issue (Yb distribution along the beam direction). The sample made by a piece of pristine Fiber#1 was put into a FIB system again in order to obtain a thinner thickness.

As shown in Figure 4-7, the red arrow indicates a hole in the sample which was created by further milling with the ion beam. Theoretically, the thickness of the edge of the hole should be much less than 60 nm, although it is difficult to accurately assess the thickness of the observation area.

Figure 4-8 shows the STEM-HAADF micrograph for the thinner pristine specimen in the core (a) and cladding (b). In the region of the red circle, Yb atoms are evident from the bright spot. The micrograph shows that the Yb atoms are not distributed uniformly over the cross-section as some of them tend to cluster together. There is no evident bright spot on (b). To our best knowledge, it is the first time that single Yb atoms have been observed in doped fibers by electron microscopy.

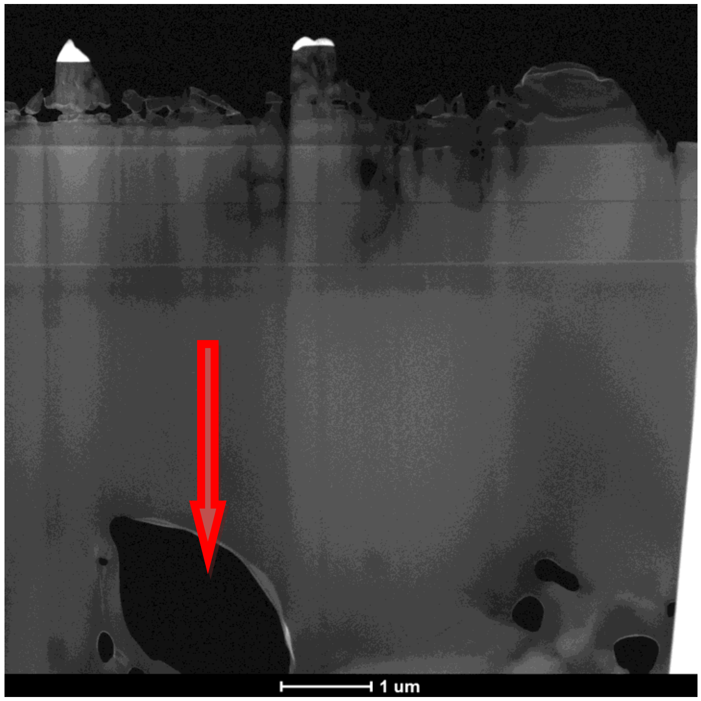

Figure 4-7 Thinner pristine Fiber#1 TEM specimen

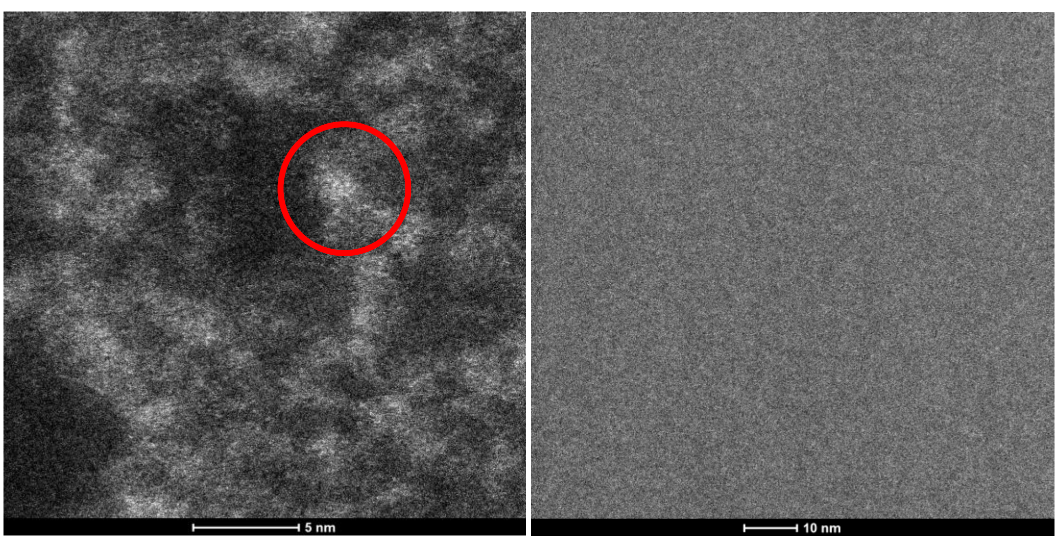

Figure 4-8 STEM micrographs for thinner pristine fiber specimen in (a) core, and (b) cladding

The theoretical Yb atoms numbers are shown in Table 4-4.

Table 4-4 The calculated results of Figure 4-8

estimated thickness	0 ~ 60 nm
observation area	620 nm^2
entire volume	0 ~ 37,200 nm^3
doping density	2.09×10^{26} $ions/m^3$
theoretical Yb atom number	0 ~ 7,775 ions

4.1.2 Fiber#2

Fiber#2 is a type of phosphorous co-doped fiber with a medium concentration of Yb atoms and is photodarkening free. It is provided by CorActive High-Tech Inc and its product number is Yb-17-05. A photodarkening free doped fiber indicates a doped fiber which does not photodarken significantly on the time frames of interest. The main parameters of Fiber#2 are shown in Table 4-5.

According to the results of observations on Fiber#1, a thinner TEM sample made by the FIB method has a greater potential to provide high resolution images of single Yb atoms than a normal TEM sample. Therefore, a further milling process was applied on the sample made from Fiber#2. The red arrow on Figure 4-9 indicates the area which was thinned by the ion beam. It is clearly shown on the figure that the thinned area is located at the bottom part of the slice. The EDS spectra of the Fiber#2 sample are similar to that of Fiber#1 (Figure 4-2).

Table 4-5 Parameters of Fiber#2

Double clad optical fiber	
Core diameter	4-6 μm
Cladding diameter	124.5-125.5 μm
Ytterbium concentration	2.48×10^{26} ions/m^3
core absorption @ 915 nm	180-240 dB/m
core absorption @ 974 nm	900 dB/m
numerical aperture (NA)	0.16-1.18

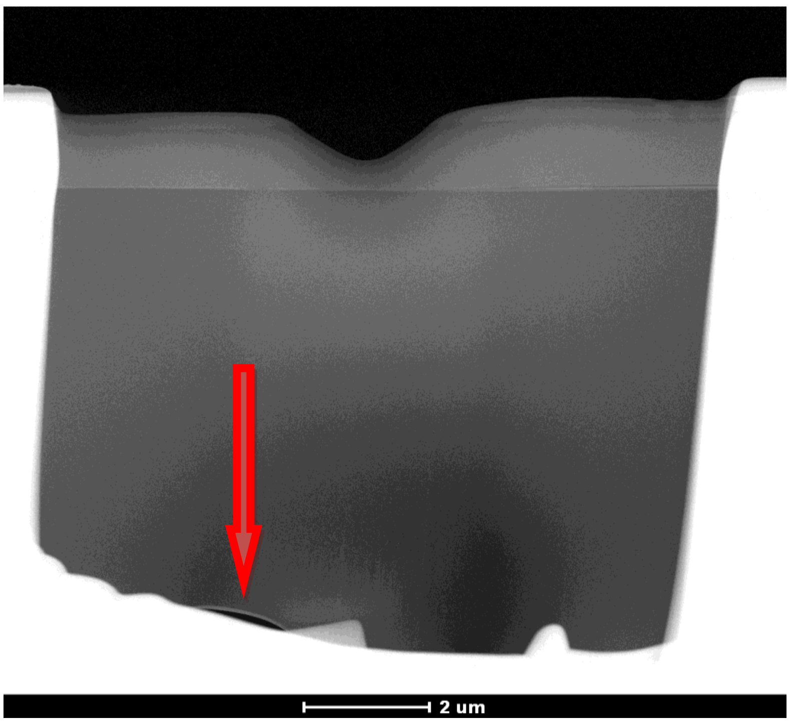

Figure 4-9 Thinner pristine Fiber#2 TEM specimen

Figure 4-10 (a) and (b) are the STEM-HAADF micrographs of the sample made by Fiber#2 with different scales. Numerous Yb atoms can be observed in Figure 4-10 (a). The Yb atoms also tend to be clustered together in the very bright areas. In the view of Figure 4-10 (b) with a higher resolution, many more Yb atoms and a few clustering areas can be distinguished.

The thickness of the observational area is between 0 nm and 60 nm. The theoretical Yb atoms numbers for Figure 4-10 (a) and (b) are shown in Table 4-6.

Table 4-6 The calculated results of Figure 4-10

	Figure 4-10 (a)	Figure 4-10 (b)
estimated thickness	0 ~ 60 nm	0 ~ 60 nm
observation area	620 nm^2	318 nm^2
entire volume	0 ~ 37,200 nm^3	0 ~ 19,080 nm^3
doping density	2.48×10^{26} $ions/m^3$	2.48×10^{26} $ions/m^3$
theoretical Yb atom number	0 ~ 9,226 ions	0 ~ 4,732 ions

From all of the observations above, one can conclude that in situ lift-out using a FIB system is an effective way to observe single Yb atoms in doped optical fibers. However, one important disadvantage of this method must be taken into account. A high energy (30 KeV) ion beam hitting the sample may cause some damage on the surface of the sample, although a much lower ion energy is used in a cleaning process (a 5 KeV ion beam is used in the first cleaning process, and a 1 KeV ion beam is used in the second cleaning process) [51]. Therefore, some other methods to prepare TEM samples without high energy beams (i.e. microtome and tripod polishing) have been developed.

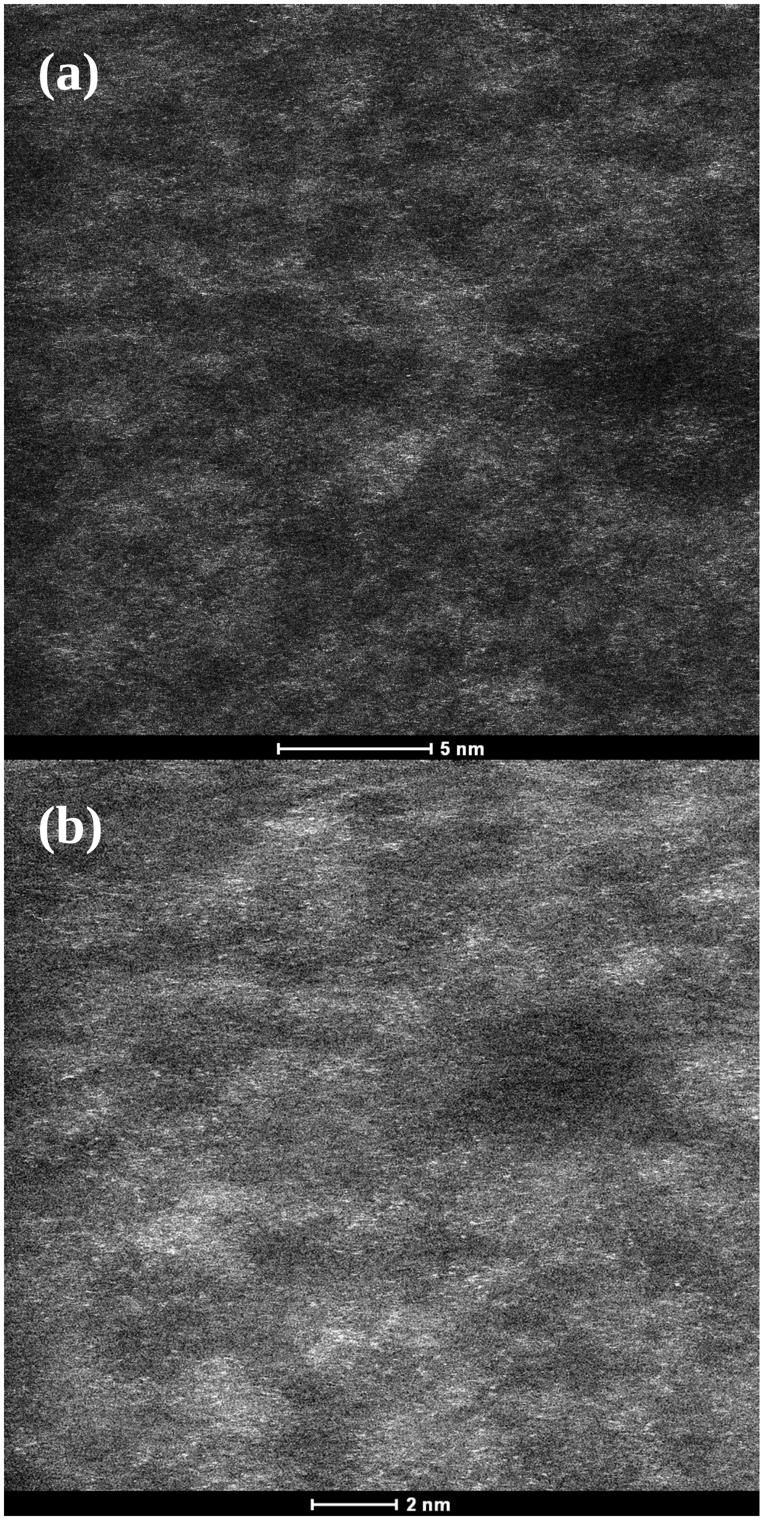

Figure 4-10 (a) and (b) STEM micrographs for Fiber#2 in the core

4.2 Ultramicrotomy

To avoid the damage resulting from high energy ion beams in the FIB system, the ultramicrotomy method was tried to produce a TEM specimen. The fiber used in this method is referred to as Fiber#3, which is provided by CorActive High-Tech Inc with product number Yb-13-06-02. The main parameters of Fiber#3 are shown in Table 4-7. Fiber#3 is a type of aluminum co-doped fiber with low concentration of Yb and is free of photodarkening effects.

Table 4-7 Parameters of Fiber#3

Double clad optical fiber	
Core diameter	5.5-6.5 μm
Cladding diameter	124.5-125.5 μm
Ytterbium concentration	1.15×10^{25} ions/m^3
core absorption @ 915 nm	20-30 dB/m
numerical aperture (NA)	0.12-1.14

The pieces of fiber should be surrounded by polymer (in this case, epon and spurr are used, respectively) to form a bulk piece which can then be cut by the microtome (see Figure 4-11 (b)). On the first try, the fiber with a cladding diameter of about 125 μm was put into the polymer directly (left hand of Figure 4-11 (b)). This resulted in the thin pieces cut by the microtome being cracked. This is attributed to the unbalanced ratio between the thickness of the slice and the diameter of the fiber. The thicknesses of the slices cut by the microtome were 70 nm or less while the diameter of the fiber was about 125 µm. Therefore, it appears that a solution is that one should reduce the diameter of the fiber first and then take slices from the specimen. Hydrogen Fluoride (HF) with a concentration of 40% was used to etch the fiber. The fibers were dipped into the HF. Through a 40-minute etching process, the diameter of the fiber was reduced to 3-5 µm (Figure 4-11).

However, it turned out that the polymer could not hold the thinner fiber either. Figure 4-12 shows that only a hole was left in the slice. Epon epoxy was used in Figure 4-12 (a) and Spurr epoxy was used in Figure 4-12 (b). Epon epoxy is the most commonly used embedding media and Spurr epoxy, which has a lower viscosity than Epon epoxy, is sometimes used as an alternative for Epon epoxy [52]. Fragments of the optical fiber are observed to be remaining around the hole. The reason for the failure is still attributed to the ratio between the diameter of the fiber and the thickness of the slices. Although the diameter of the fiber was reduced to 3-5 µm, much smaller than the original 125 µm, it was still at least some tens of times greater than the thickness of the slices.

It is hard to etch the fiber to a thinner diameter. When the diameter reaches about 5 µm, the fiber is so tiny that it can hardly be observed by human eyes directly. The fiber, which can even float in stationary air, also becomes very fragile. So 5 µm is the limitation which can be manipulated in this case. If a smaller diameter is required, the etching process should be re-designed in the future.

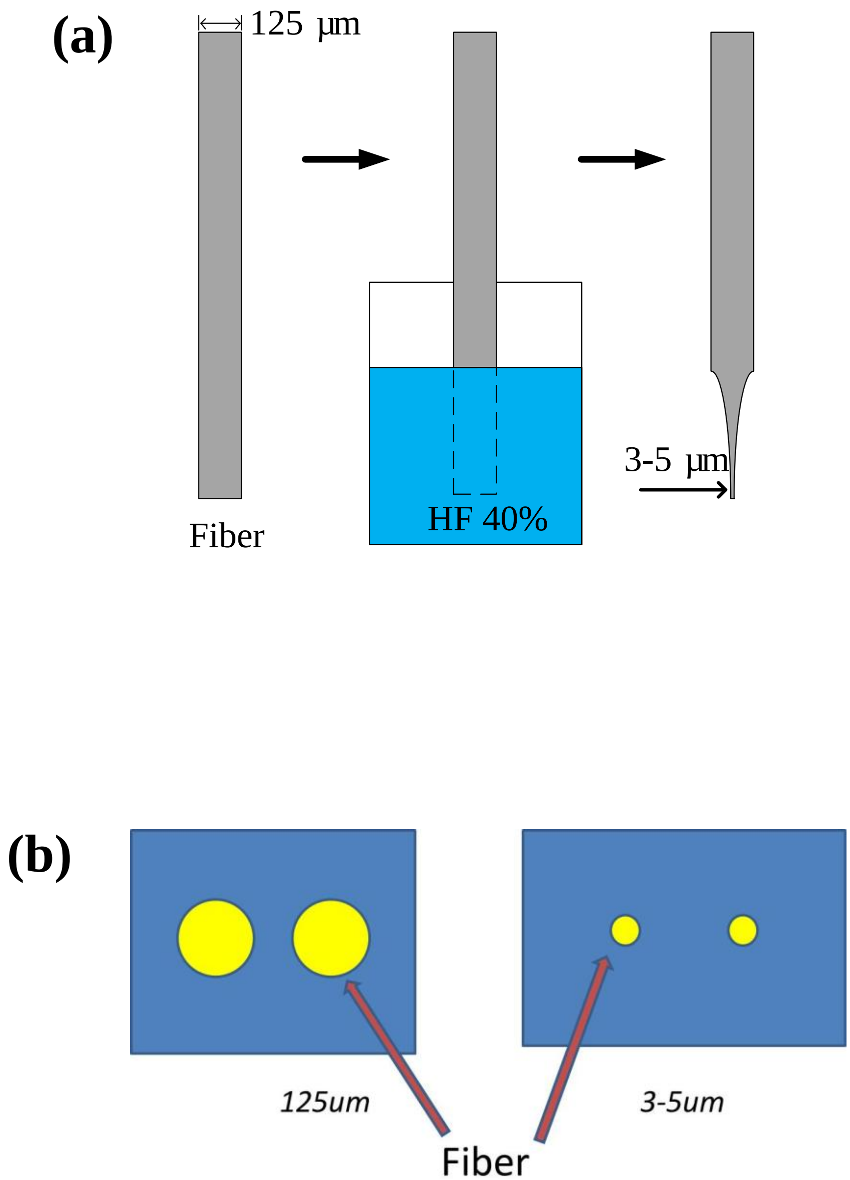

Figure 4-11 (a) The HF etching process. The fiber samples before and after HF etching. (b) The cross-section of fiber sample surrounded by polymer. The left one is the fiber before HF etching and the right one is after etching.

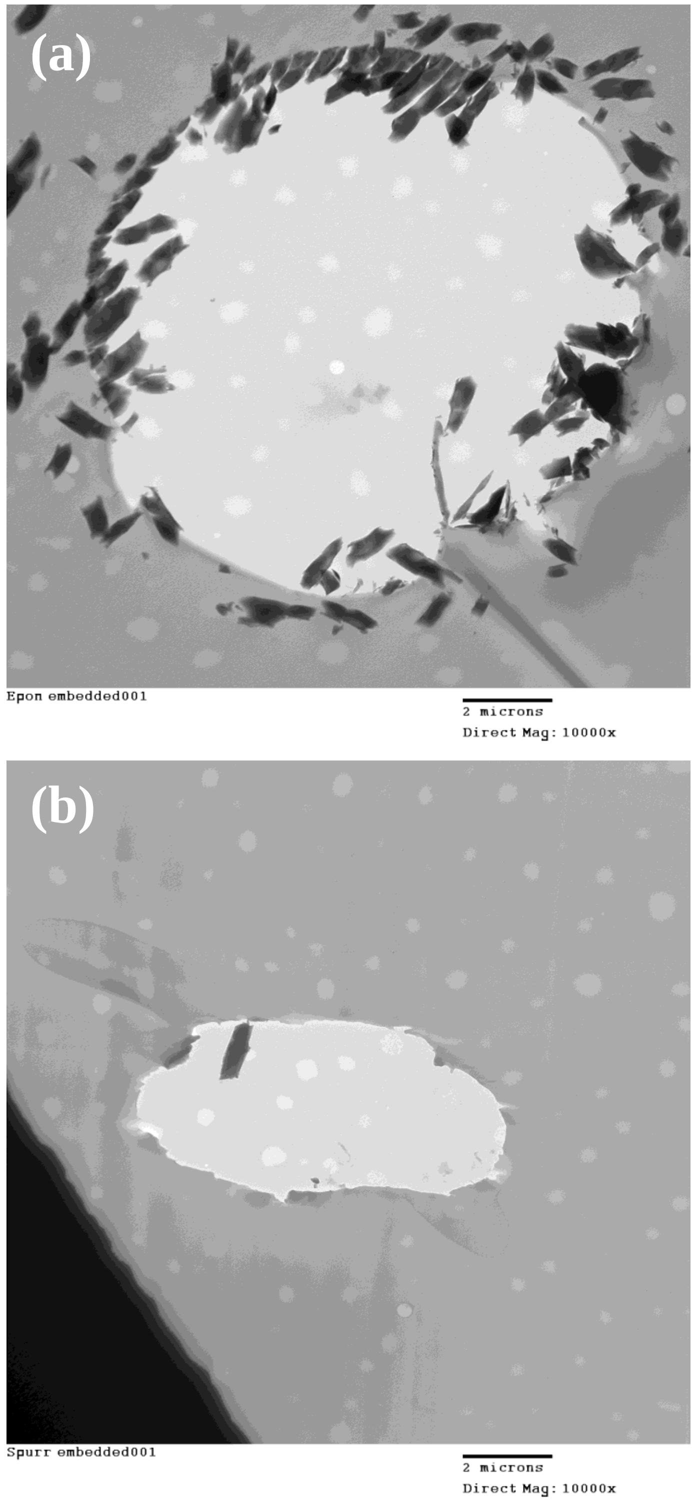

Figure 4-12 Etched fiber surrounded by (a) Epon epoxy (b) Spur epoxy

4.3 Tripod Polishing and Ion Milling

A popular method, tripod polishing and ion milling, was used to prepare the next TEM sample. The fiber used in this case is referred to as Fiber#4. Fiber#4 is a type of phosphorous co-doped fiber with a high Yb concentration and very low darkening. It is provided by CorActive High-Tech Inc and the product number is Yb-19-04. The main parameters of Fiber#4 are shown in Table 4-8.

Table 4-8 Parameters of Fiber#4

Double clad optical fiber	
Core diameter	3-5 μm
Cladding diameter	124-126 μm
Ytterbium concentration	6.23×10^{26} ions/m^3
core absorption @ 915 nm	450-650 dB/m
core absorption @ 974 nm	2000 dB/m
numerical aperture (NA)	0.19

The tripod polishing method can only deal with bulk material (1 mm ×1 mm× 1.5 mm at least). So the first step is to make the fiber into a bulk-like material. Figure 4-13 shows the schematic of this process. Two slices of silicon (thickness of 500 μm each) and one piece of microscope cover glass (thickness of 150 μm) were used to secure the fiber samples with EPOXY 353ND. Figure 4-13 (a) shows a 3D view of this assembly sample. The fiber is lined parallel to the silicon wafer and the glass. Figure 4-13 (b) shows a 2D lateral view and (c) shows a top view of the sample. The dimensions are indicated on the figures.

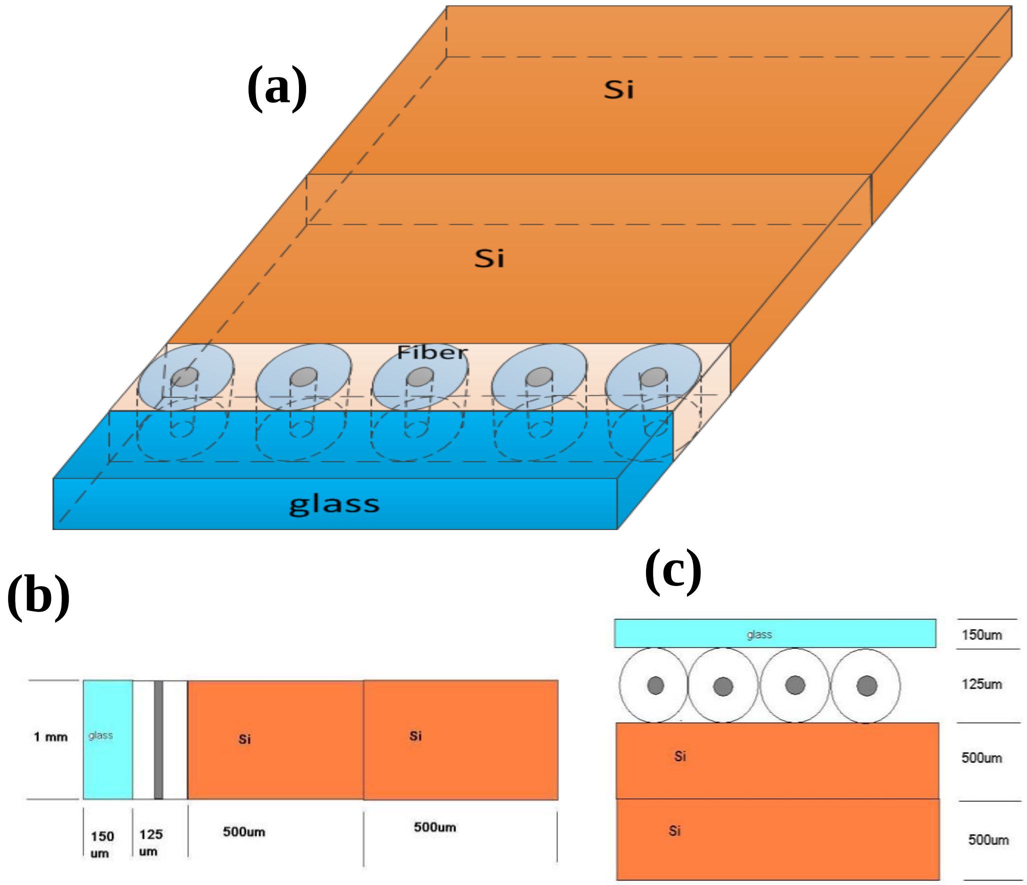

Figure 4-13 A schematic of sample preparation with tripod polishing method (a) 3D (b) and (c) 2D

Then mechanical polishing can be used on this assembly as it is on traditional bulk samples. The assembly is usually polished to a wedge shape with a 4° angle, as shown in Figure 4-14. However, the most challenging part in this process is that the tip of the wedge must be just at the core of the fiber (see Figure 4-15). Mechanical polishing is used firstly for coarse shaping and fine polishing is then carried out with ion milling.

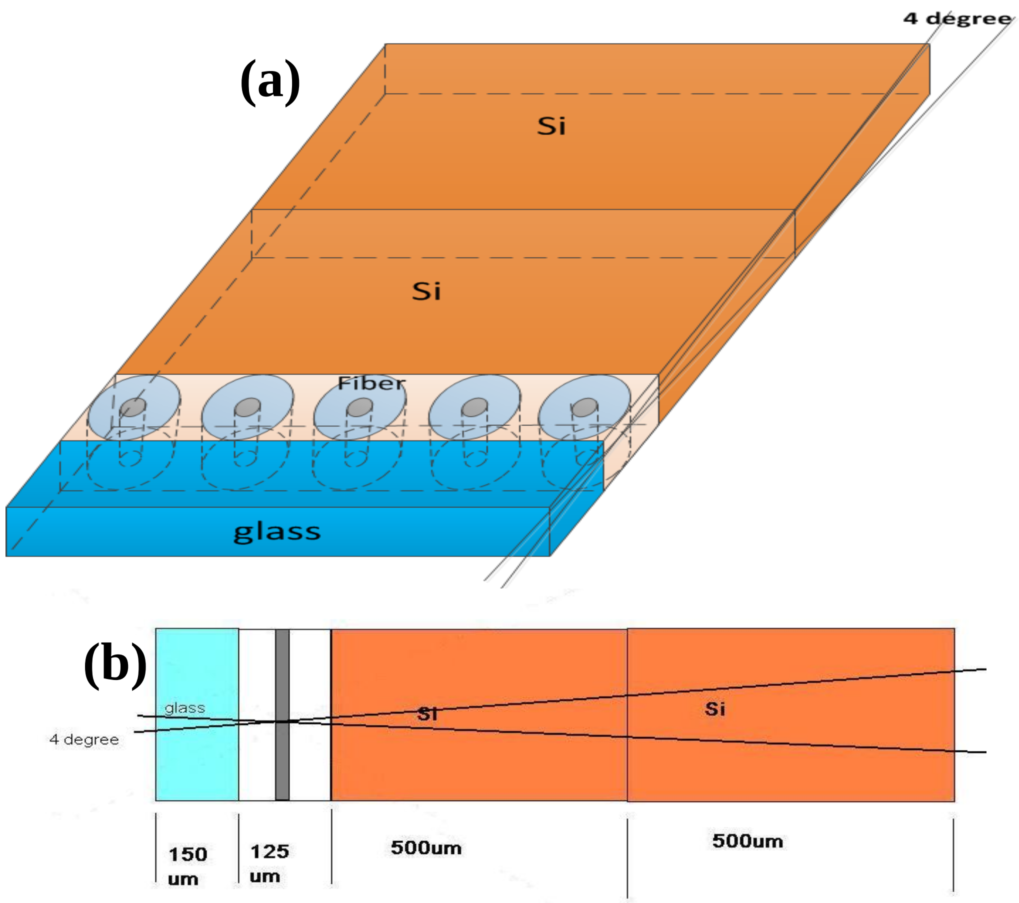

Figure 4-14 (a) 3D (b) 2D schematic for polishing

The difficulties come from the small core diameter. In the mechanical polishing process, the sample should be observed under a common optical microscope to judge whether the tip has reached the core area or not. However, since the refractive index and the thickness of the core and the cladding are similar, the difference between the core and the cladding is not clear even when viewed under an optical microscope. A margin can be left in this step (one does not have to reach the core) to ensure that the core is well preserved after all thinning procedures. In the ion milling process, one can utilize the monitor of the ion polishing system to measure the dimensions of the fiber. Figure 4-15 shows the ideal final sample using this method. The glass cover at the head of the assembly is totally polished away and only half of each fiber is left at the top of the wedge shape. The core of the fiber exactly sits at the tip of the wedge.

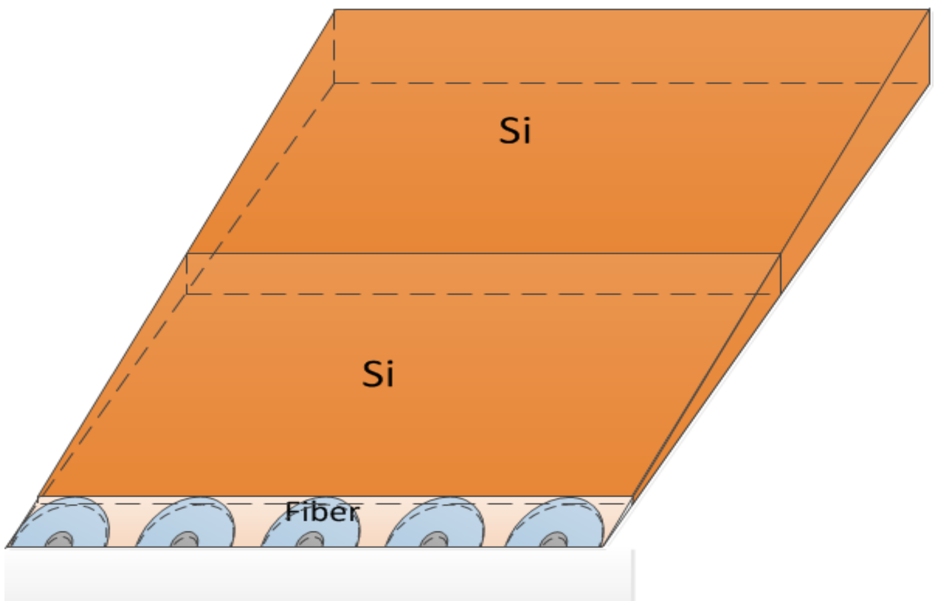

Figure 4-15 The wedge shape sample after polishing

Figure 4-16 is the actual view of the sample. Figure 4-16 (a) shows an overview of the entire sample. Some of the fibers are broken. This could be caused by mechanical cutting or polishing. Some of the fibers are still unabridged while the target one (indicated by the blue arrow) only half remains. Figure 4-16 (b) shows the view of the target fiber. Some ripples occurring at the top of the semicircle indicate that the thickness of that region is thin enough for TEM observation.

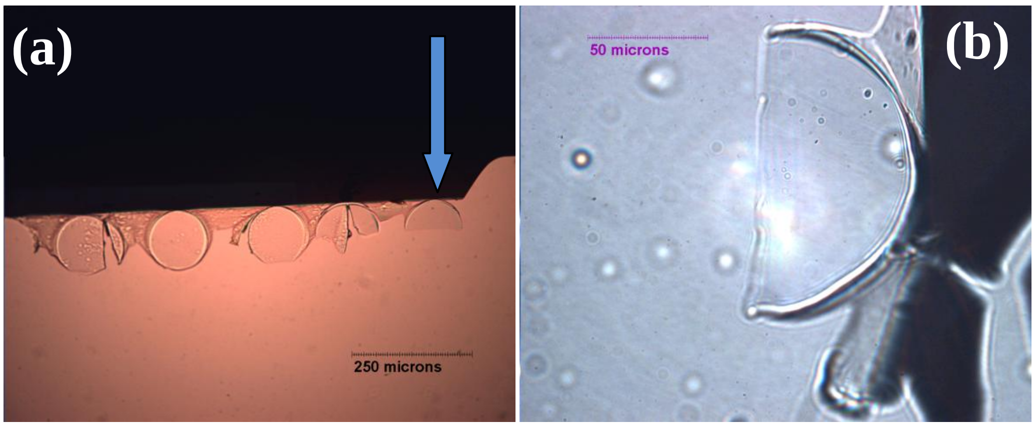

Figure 4-16 (a) and (b) the image of sample under optical microscope

Figure 4-17 shows the target fiber observed under a microscope in micro-scale. The projecting (indicated by a red circle) area in the micrograph is the core of the fiber. It is formed in the ion milling process. An argon (Ar) beam was used for ion milling, the atoms of which are heavier than Si and O atoms but lighter than Yb atoms. Thus it is easy to remove the host material, SiO_2, but a little more difficult to remove the dopant atom, Yb. This could possibly lead to an increased concentration of Yb.

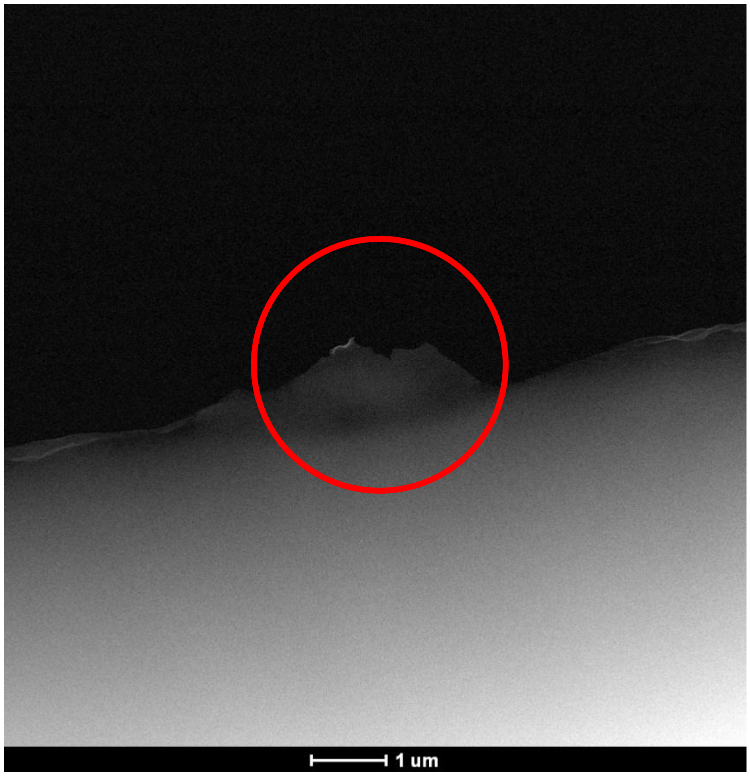

Figure 4-17 The core of the fiber under STEM

Figure 4-18 (a) shows the EDS spectrum for the part of Figure 4-17 projecting outwards from the sample, while (b) shows the EDS spectrum within the sample. The first spectrum clearly indicates the dopant element Yb and the co-dopant element P. The second shows that only Si and O were detected. The EDS spectra figures are direct evidence proving the location of the core area.

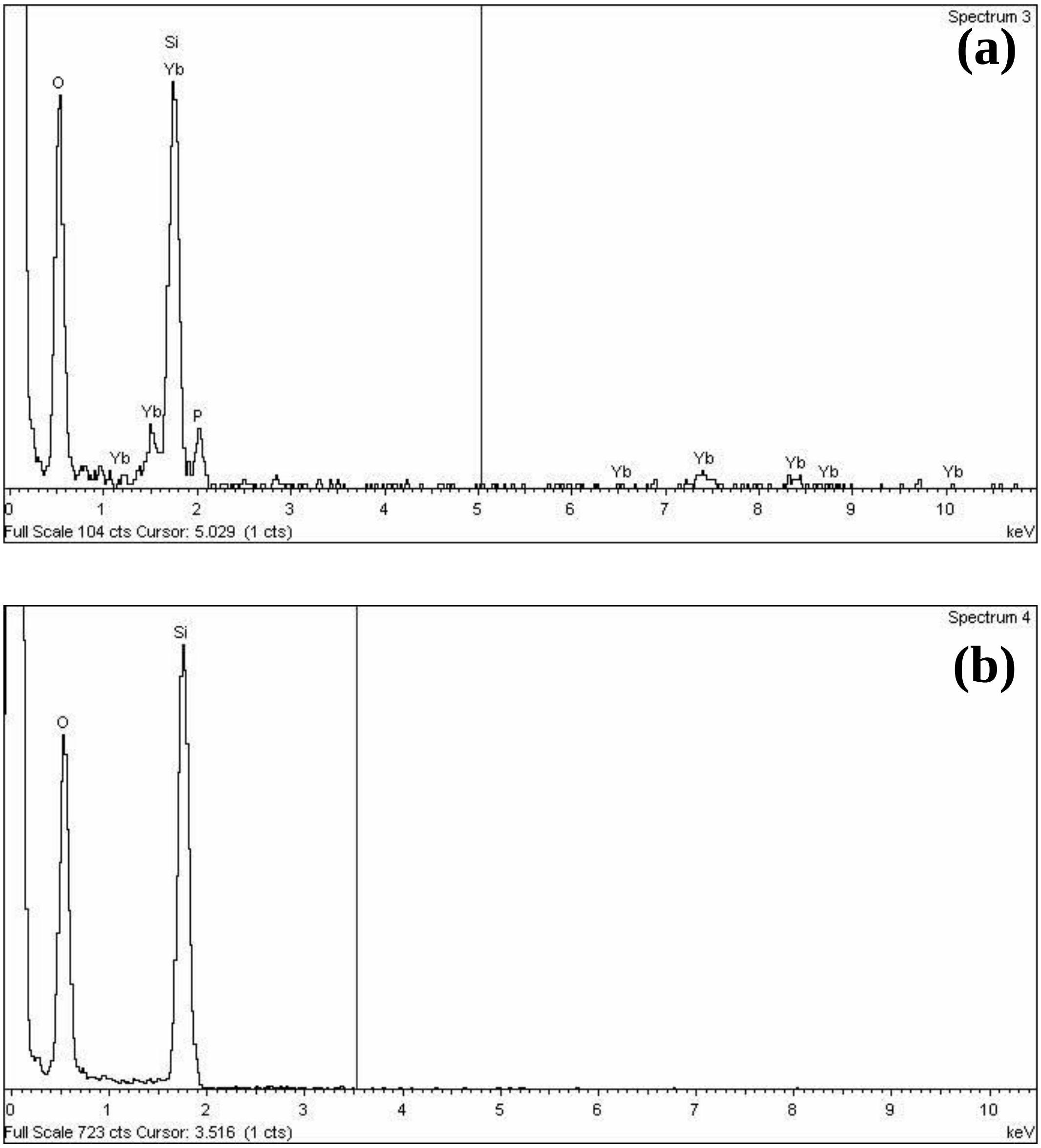

Figure 4-18 EDS spectra for Fiber#4 in (a) core, and (b) cladding

Figure 4-19 (a) and (b) are the STEM-HAADF micrographs of the sample made from Fiber#4 with different scales. In Figure 4-19 (a), Yb atoms can be observed. In the red circle area, the Yb atoms are clustered together intensively and this has never been observed before. The intensive clustering may be due to the high doping density of Fiber#4. Figure 4-19 (b), which is located at a different area from (a), has a higher resolution than (a). Numerous Yb atoms and a few of clustering areas can be distinguished in the figure.

The thickness of the observation area is between 20 and 40 nm. The theoretical Yb atom numbers for Figure 4-19 are shown in Table 4-9.

Table 4-9 The calculated results of Figure 4-19

	Figure 4-19 (a)	Figure 4-19 (b)
estimated thickness	20 ~ 40 nm	20 ~ 40 nm
observation area	753 nm^2	378 nm^2
entire volume	15,060 ~ 30,120 nm^3	7,560 ~ 15,120 nm^3
doping density	6.23×10^{26} ions/m^3	6.23×10^{26} ions/m^3
theoretical Yb atom number	9,382 ~ 18,765 ions	4,710 ~ 9,420 ions

Using the tripod polishing method to prepare the TEM sample avoids the concern that the high energy ion beam utilized in the FIB system could damage the sample. However, the ion milling process also involves Ar beams polishing the sample, although the energy (2 KeV) is much smaller than that of the FIB system (30 KeV). As mentioned above, when the Ar beam is polishing the sample, the Si and O atoms are easier to remove than Yb atoms. This may increase the doping density in the core area by removing relatively more Si and O atoms. Some suggestions to improve the accuracy will be discussed in chapter 5.

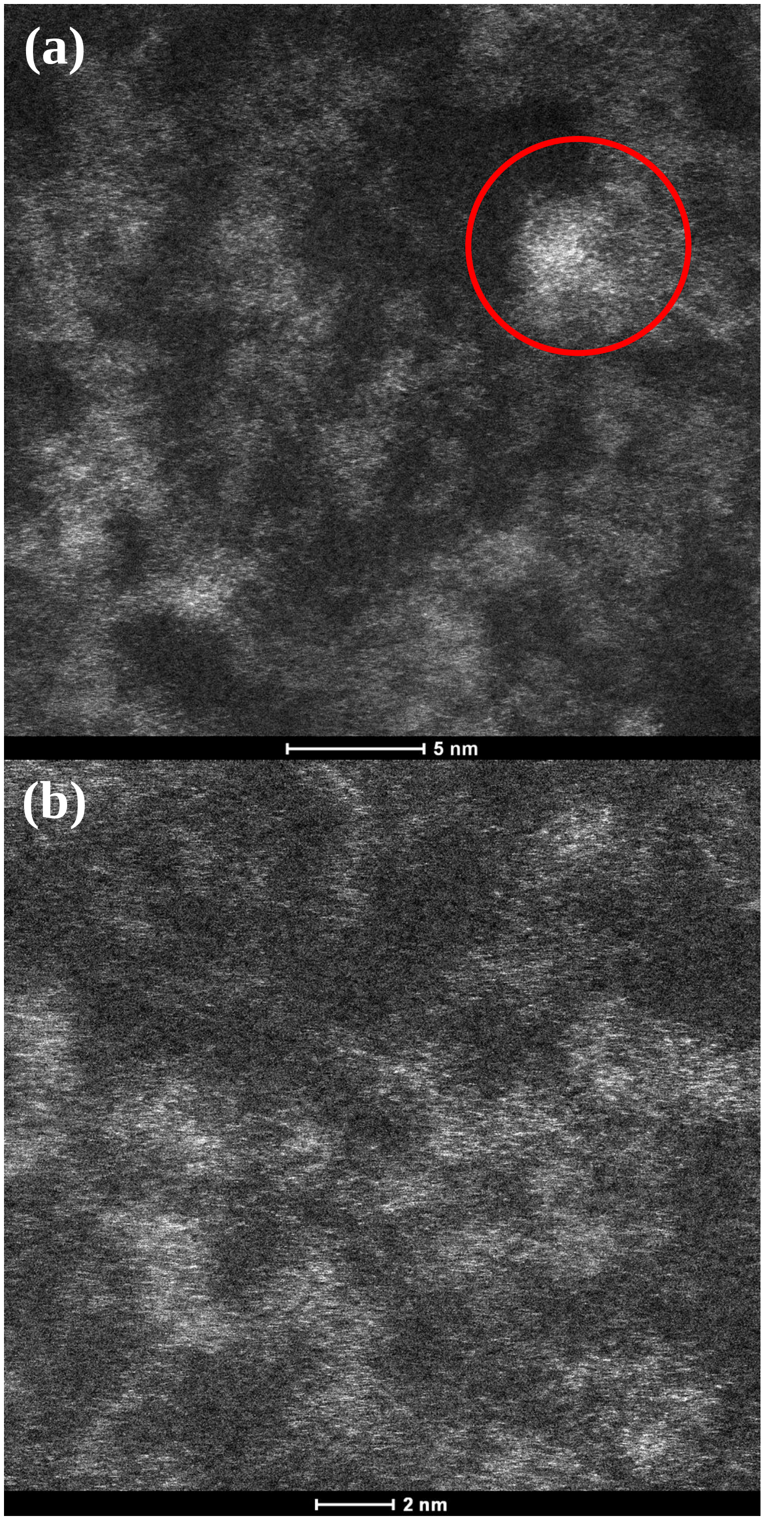

Figure 4-19 (a) and (b) STEM micrographs for Fiber#4

Since the concentration of Yb atoms is too high in Figure 4-19, a fiber with a lower Yb doping density may provide a micrograph in which the single atoms can be distinguished more easily. Therefore, Fiber#2, which has a lower doping density than Fiber#4, is used to make the sample. Gentle milling with an energy of 0.2 KeV is applied to replace the standard ion milling which usually utilizes an energy of 2 KeV. However, no material was removed after a couple of hours of gentle milling.

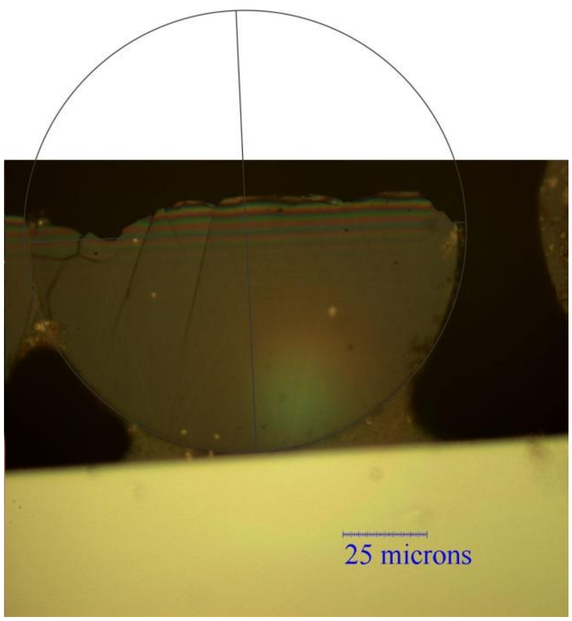

Figure 4-20 The TEM sample made with Fiber#2 by tripod polishing and ion milling method

Figure 4-20 shows the shape of the sample observed under optical microscopy. The edge of sample has not reached the core yet. This is the most up-to-date record and this particular work has not been finished yet.

4.4 Numerical Modeling

A numerical model was developed to count the number of Yb atoms in the micrographs. The algorithm is shown in Figure 4-21. Assume that a micrograph has a 2048×2048 resolution, which includes 2048×2048 pixels. The number *i* indicates the *i*th column while the number *j* indicates the *j*th row. The size of one Yb atom is assumed to be 9 pixels (the circled area by red line in Figure 4-21). The center pixel of the 9-pixel-square is referred to as (i, j), so the other eight pixels can be referred to as (i-1, j-1), (i-1, j), (i-1, j+1), (i, j-1), (i, j+1), (i+1, j-1), (i+1, j), (i+1, j+1), respectively. A grey value can be defined such that, if all these nine pixels are above the grey value, the 9-pixel-square can be considered as a Yb atom, otherwise it will be considered noise. This value is called the threshold value. When the first square is scanned, the square moves to the next one with the central pixel moving to (i+1, j) or (i, j+1). Then the central pixel and the other eight pixels around it will be scanned for the grey value. In the 2048×2048 micrograph, the values of *i* and *j* are from 2 to 2047 to avoid the pixels at the boundary. If the resolution of a micrograph changes to 1024×1024, the values of *i* and *j* change to between 2 and 1023. The assumptions on the size of the atom are also flexible. If the size of an atom changes to 25 pixels, i-2, i+2 columns and j-2, j+2 rows could be introduced.

However, some difficulties are encountered with this algorithm. First, it is dificult to determine the size of a single Yb atom in the figure. Some groups reported about the size of single atoms [48]-[50]. They depend on analyzing the profile of single-atom spots appearing in the micrographs (e.g. the full width at half maximum). However, single atoms in this thesis are difficult to distinguish and can appear as different sizes in the micrographs (some atoms may be in a better focus than others). Secondly, the appropriate threshold grey value is difficult to determine. The contrast is arbitrary for each micrograph. For example,

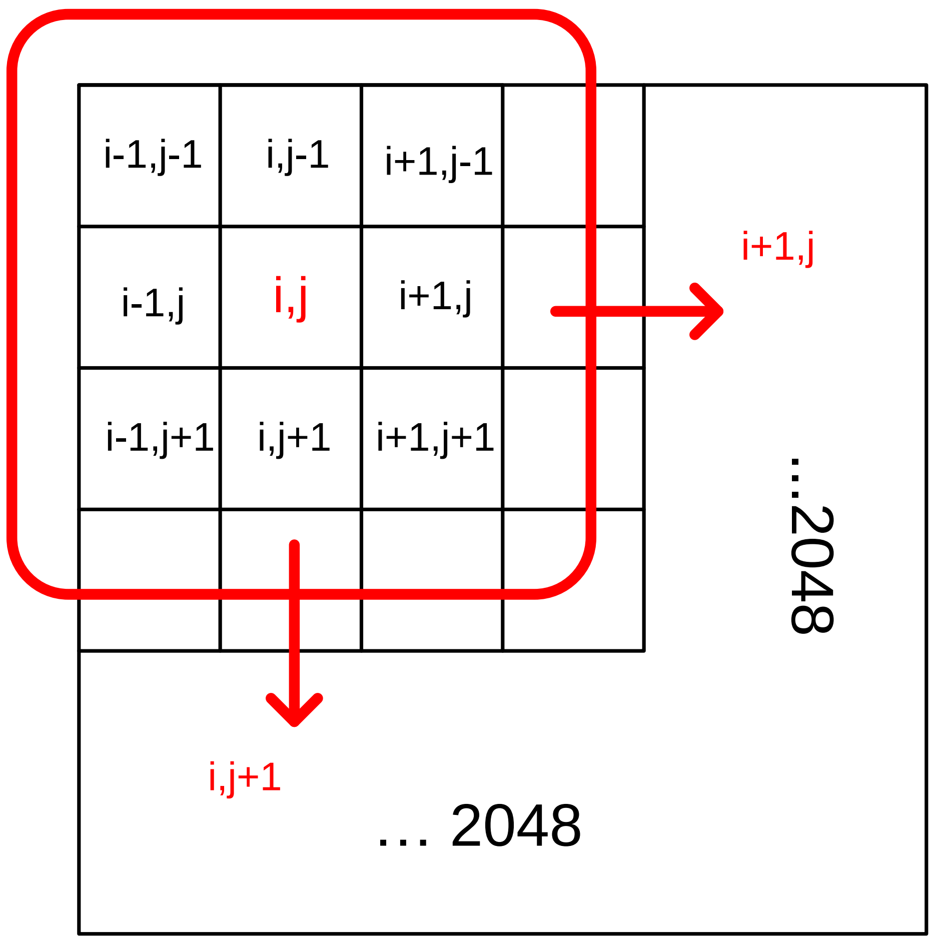

Figure 4-21 Illustration of the algorithm for counting the Yb atoms

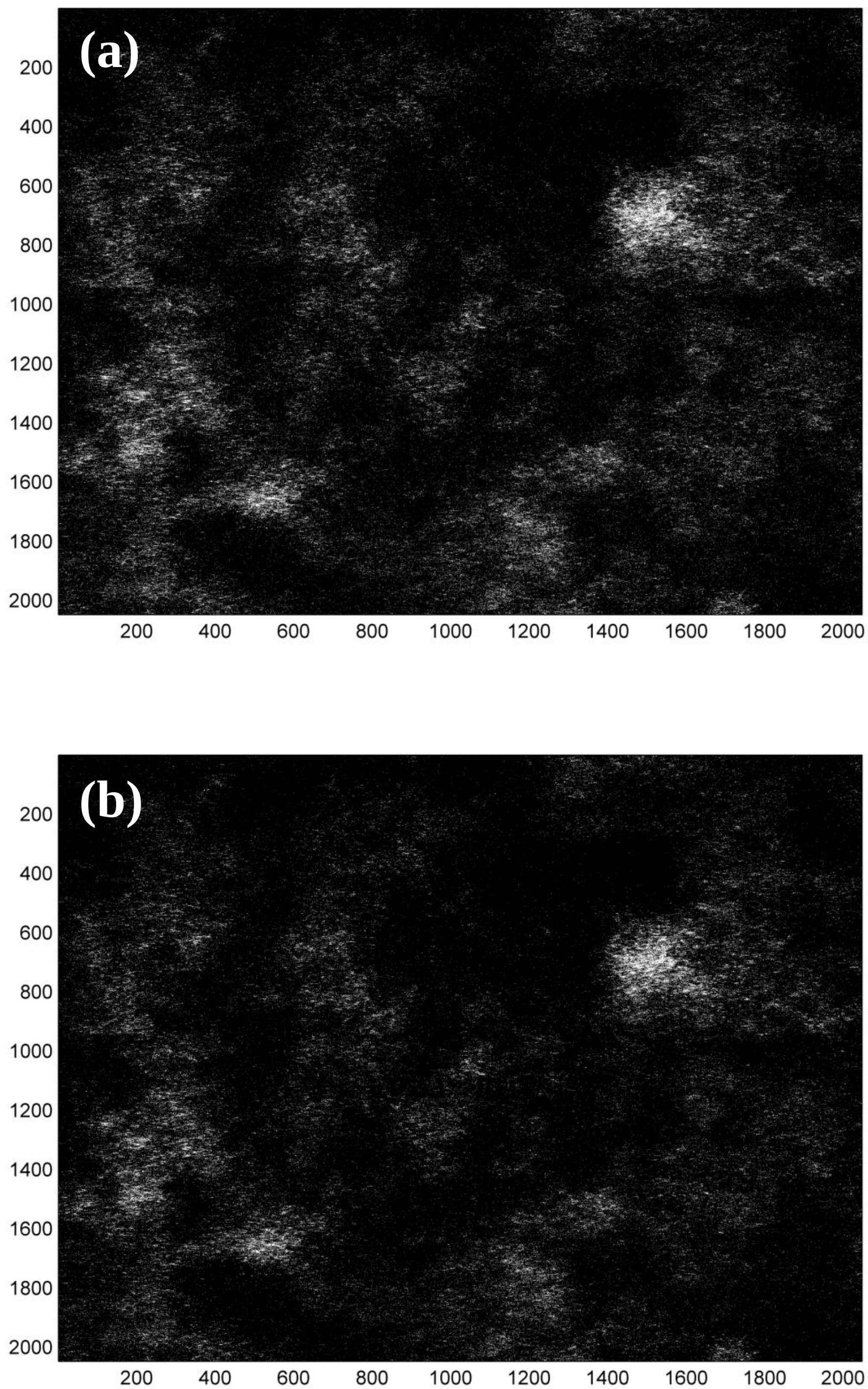

Figure 4-22 The processed figures of Figure 20 (a). The threshold value is 140 for (a) and 150 for (b)

Figure 4-22 (a) and (b) show the processed figures of Figure 4-19 (a). The threshold for each figure is 140 and 150, respectively. However, one can hardly tell the difference between the two figures while the calculation results are very different. Thirdly, one bright spot on the figure could be formed by several Yb atoms overlapping each other. Although several layers (the specimen is divided into several layers in the thickness direction) can be introduced into this algorithm, it hard to decide how many layers should be considered and what kind of bright spot can be considered as atoms overlapping each other. Thus, in order to account for the individual atoms in the numerical model, it is useful to greatly reduce the Yb doping density. In other words, the numerical model will provide more reliable results if the Yb doping concentration in the fibre is relatively low.

4.5 Summary

In the previous sections, some STEM-HAADF micrographs showed single Yb atoms in the core of the fiber. The in situ lift-out method and tripod polishing method have both proven to be effective. However, some questions still need to be discussed.

Firstly, comparing with other groups [48]-[50], the single Yb atoms are not clearly separated from each other. This may result from the high doping density of the fiber which makes the Yb atoms likely to cluster and overlap even in very thin regions of the sample. Samples made by lower Yb doping density fibers may help to identify single Yb atoms. The micrographs in which single Yb atoms are separated from each other would also make the numerical model introduced in section 4.4 more effective.

Secondly, a nonuniform distribution of Yb atoms is observed in the micrographs. However, the reason for the nonuniformity may be due to various effects, besides the original distribution in the fiber. Whether the ion milling or focused ion beam leads to Yb atom migration is still uncertain. Therefore, a sample made by gentle milling should be applied to minimize the influence of high energy ion beam. The standard ion beam energy used in gentle milling is 0.2 KeV. However, this energy is proved too low to remove any material away. Thus, a greater energy maybe used in the future. The nonuniform thickness of the sample could also lead to an observed nonuniformity. Thus, the effect of the nonuniform thickness on the observations still need to be further explored.

Thirdly, all the thicknesses of the samples were estimated by the experts in Canadian Centre of Electron Microscopy (CCEM). A more accurate way to calibrate the thickness would be very helpful in estimating the number of Yb atoms in the micrographs. Furthermore, the “depth of field”, which refers to the extent of the region of focus, still needs to be better determined.

Chapter 5 Summary and Future Work

5.1 Summary

In this thesis, two sub-projects associated with ytterbium-doped fiber amplifier technology have been presented.

In the first research activity, numerical simulations to model high-repetition rate ultrafast Yb-doped fibers are developed. For a single-fiber amplifier system, a single double-clad Yb-doped fiber is adopted. Models incorporating a range of different parameters are introduced. The relationship between the output power, ASE and the fiber length is discussed. The optimal fiber length for each scenario, which can make the powers of two output seed beams equal, is determined.

For the two-fiber amplifier system, two seed beams are amplified in separated fibers. Comparing with the single-fiber amplifier system, the two-fiber amplifier system has no advantage in either the power of the output seed beams, the signal to noise ratio (SNR) or the intensity product of the two seed beams, but has the flexibility to provide arbitrary equal output powers under the maximum value.

For the two-stage amplification system, a single-clad fiber is used in the preamplification stage (first stage) and a double-clad fiber amplifier is used in the second stage. The results show that the final output power of the signal is determined largely by the second stage pump power, while the SNR is more sensitive to the first stage pump power.

In the second research activity, to investigate the mechanism of photodarkening, the distribution of single Yb atoms is observed in a range of double-clad Yb-doped fibers. In order to prepare TEM specimens suitable for STEM with atomic resolution, three preparation methods are attempted. The in situ lift-out and tripod polishing methods have proven to be effective while the ultramicrotomy method needs further improvement. According to the STEM micrographs, the Yb atoms are distributed in the observation area nonuniformly. A numerical simulator is developed to count the number of Yb atoms in the micrographs, but further work is required in order to obtain reliable results on the numbers of Yb atoms in the samples.

5.2 Future Work

Some ideas for future research have been alluded to in the earlier chapters, but they will be summarized in this section, while new work will also be suggested to continue the pursuit of the thesis topics.

5.2.1 Power Ratio of the Two Input Seed Beams

As mentioned briefly in section 3.3.3, in a two-stage amplification system, the ASE and SNR are largely determined by the pump power of the first stage pump. The reason of this observation may be related to the power ratio of the two seed beams when they are injected into the second stage amplifier. If the two seed beams, which have a certain total power, are injected into the fiber amplifier with different power ratios, the ASE and SNR could be different. This may be the reason why the SNR is sensitive to the pump power in the first stage. There should be an optimal ratio of the two input seed powers to obtain an optimal output portfolio (including the output signal powers and SNR).

In our present work, a single-clad fiber is used as the first stage amplifier in the two-stage amplification system. One can only obtain certain power ratios of the two signal beams from the first stage amplification (see Figure 3-26). To investigate the relationship between the input power ratios at second stage and the final output results, a system which can provide arbitrary output power ratios of the two signal beams is required for the first stage amplification. The two-fiber amplifier system, which is introduced in section 3.2, could be a good choice. In this new two-stage amplification model, one can use the two-fiber amplifier system to generate different output power ratios of the two signal beams by changing the fiber amplifier length or the pump power of each signal. Some additional devices, such as notch filters which can eliminate some ASE but preserve the signal, could also be applied to improve the overall efficiency. The optimal design may improve the system efficiency or the SNR significantly.

5.2.2 Nonlinear Effects

Although the threshold powers and maximum phase shifts of some nonlinear effects are discussed in section 3.4, all of the calculations are based on continuous-wave (CW) simulation. However, development of pulsed simulation, which could involve calculations on the nonlinearities, such as SPM, SRS and SBS, for individual ultrashort pulses, would be more interesting for researchers. Future modeling work on the dual-wavelength system could be based on pulsed simulation.

The algorithm of pulsed simulation should be very different from that of CW simulation. In the CW model, the rate equations are based on steady state of the population inversion. However, in pulsed simulation, the population inversion could be varying with the propagating pulse. Furthermore, the spectral channels are static and fixed in the CW simulation, while the nonlinearities would generate new spectral channels as the pulse propagates in a pulsed simulation.

The present numerical model has already been proven to be effective to the CW model. It is expected that the future development involving the nonlinearities could provide useful predictions for intense short-pulse amplification systems.

5.2.3 New TEM Samples

As discussed in chapter 4, a high energy ion beam used to mill the samples may cause undesirable changes to the material. Therefore, gentle milling, in which the standard energy of ion beam is 0.2 KeV, is introduced in the sample preparation process. The experiment based on this idea has already started. The preliminary result is shown in Figure 4-20. However, the result showed that the low energy ion beam used in gentle milling could hardly remove any material even after a few hours of processing. A higher energy ion beam may be required in future work (but should be still much smaller than the standard energy used in ion milling, 2 KeV). Furthermore, it was reported that ion milling or gentle milling process is not necessary in the sample preparation process [48]. The mechanical polishing machine can also ensure that the samples are thin enough to be observed under a TEM without the ion milling process [39]. However, the most challenging part is still to ensure that the core of the fiber is located just at the tip of the wedge-shaped specimen. With a much faster "milling speed" than the ion milling process and without a camera to monitor the instant progress of the polishing, the only use of mechanical polishing would be much more difficult than using the ion milling process to obtain an ideal sample.

To distinguish single atoms clearly, low doping density fibers are also required to avoid the atoms overlapping in the electron micrographs. In the future work, the TEM samples should be made from fibers with different doping densities. The doping density of the fiber used in Figure 4-20 (Fiber#2) is about 40% of that of Fiber#4. In the future work, Fiber#3, the doping density of which is only 2% of that of Fiber#4, could also be investigated.

5.2.4 Possible Further Analysis of the TEM Micrographs

Besides the *Z* contrast theory, it would be desirable to find an experimental method could verify that the bright dots on the STEM-HAADF micrographs represent Yb atoms.

In the figures such as Figure 4-10 and Figure 4-19, which have high resolution, the bright dots in the area of apparent Yb-atom clustering cannot be detected by the EDS separately due to the limitation of the instrument in the mode that was utilized. However, one can compare the intensities of EDS signals for the different areas, which are chosen from a low resolution micrograph, in a high resolution characterization. For example, Figure 5-1 shows a STEM-HAADF micrograph of the core area of Fiber#4 in low resolution. There are some bright regions with diameters of about 10 nm on the figure. One can choose one bright area and one dark area under the STEM and magnify those areas to the same resolution level as in Figure 4-10 or 4-19. If the Yb signal in the EDS spectrum of the bright area would turn out to be much stronger than that in the dark area, it would be strong evidence that the bright dots indeed represent Yb atoms.

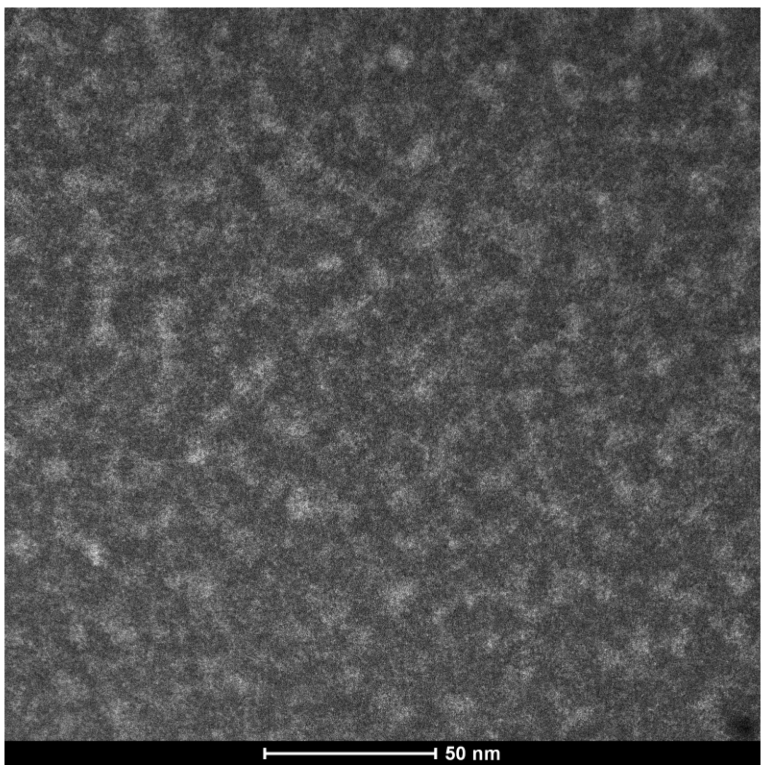

Figure 5-1 STEM-HAADF micrographs of Fiber#4 in the core area

References

1. Hajialamdari, M., A.M. Alkadry, and D. Strickland, *Modeling of a two-color, two-stage, ultrafast Yb-doped fiber amplifier.* Optics Communications, 2011. **284**(12): p. 2843-2848.

2. Al-Kadry, A.M. and D. Strickland, *Generation of 400 µW at 17.5 µm using a two-color Yb fiber chirped pulse amplifier*. Opt. Lett., 2011. **36**(7): p. 1080-1082.

3. Goldberg, L., et al., *Mid-infrared difference-frequency generation source pumped by a 1.1-1.5 µm dual-wavelength fiber amplifier for trace-gas detection.* Opt. Lett., 1998. **23**(19): p. 1517-1519.

4. Pan, L., I. Utkin, and R. Fedosejevs, *Two-wavelength passively Q-switched ytterbium doped fiber laser.* Opt. Express, 2008. **16**(16): p. 11858-11870.

5. Romero-Alvarez, R., et al., *Two-color fiber amplifier for short-pulse, mid-infrared generation.* Opt. Lett., 2008. **33**(10): p. 1065-1067.

6. Creeden, D., et al., *Compact Fiber-Pumped Terahertz Source Based on Difference Frequency Mixing in ZGP.* Selected Topics in Quantum Electronics, IEEE Journal of, 2007. **13**(3): p. 732-737.

7. Budz, A.J., et al., *Short-Pulse Dual-Wavelength System Based on Mode-Locked Diode Lasers With a Single Polarization-Maintaining Yb:Fiber Amplifier.* J. Lightwave Technol., 2009. **27**(16): p. 3416-3424.

8. Paschotta, R., *Encyclopedia of Laser Physics and Technology*. 1 ed. 2008: Wiley-VCH.

9. Engholm, M. and L. Norin, *Preventing photodarkening in ytterbium-doped high power fiber lasers;correlation to the UV-transparency of the core glass.* Opt. Express, 2008. **16**(2): p. 1260-1268.

10. Koponen, J., et al., *Photodarkening rate in Yb-doped silica fibers.* Appl. Opt., 2008. **47**(9): p. 1247-1256.

11. Yoo, S., et al., *Photodarkening in Yb-doped aluminosilicate fibers induced by 488 nm irradiation.* Opt. Lett., 2007. **32**(12): p. 1626-1628.

12. Jayesh, J., et al. *Effect of Heat and H2 Gas on the Photo-Darkening of Yb^{+3} Fibers*. 2006: Optical Society of America.

13. Paschotta, R., et al., *Ytterbium-doped fiber amplifiers.* Quantum Electronics, IEEE Journal of, 1997. **33**(7): p. 1049-1056.

14. Islam, M.N., *Raman Amplifiers for Telecommunications 1: Physical Principles*. 1 ed. 2003: Springer.

15. Keiser, G., *Optical Fiber Communications*. 3 ed. 2000: McGraw-Hill.

16. Desurvire, E., *Erbium-Doped Fiber Amplifiers: Principles and Applications*. 1 ed. 1994: Wiley-Interscience.

17. Pask, H.M., et al., *Ytterbium-doped silica fiber lasers: versatile sources for the 1-1.2 μm region.* Selected Topics in Quantum Electronics, IEEE Journal of, 1995. **1**(1): p. 2-13.

18. Zou, X. and H. Toratani, *Evaluation of spectroscopic properties of Yb^{3+} -doped glasses.* Physical Review B, 1995. **52**(22): p. 15889.

19. Takebe, H., T. Murata, and K. Morinaga, *Compositional Dependence of Absorption and Fluorescence of Yb^{3+} in Oxide Glasses.* Journal of the American Ceramic Society, 1996. **79**(3): p. 681-687.

20. Paschotta, R., et al., *Lifetime quenching in Yb-doped fibres.* Optics Communications, 1997. **136**(5-6): p. 375-378.

21. Nilsson, J., et al., *Evaluation of parasitic upconversion mechanisms in Er^{3+}-doped silica-glass fibers by analysis of fluorescence at 980 nm.* Lightwave Technology, Journal of, 1995. **13**(3): p. 341-349.

22. Budz, A.J., *Ultrashort-Pulse Laser System Based on External-Cavity Mode-Locked InGaAs-GaAs Semiconductor Oscillators and Semiconductor or Yb:Fibre Amplifiers*, in *Engineering Physics*. 2008, McMaster University: Hamilton.

23. Jaunart, E. and P. Crahay, *Accurate EDFA modelling using a simple method.* Optical and Quantum Electronics, 1995. **27**(10): p. 881-886.

24. Kazovsky, L., S. Benedetto, and A. Willner, *Optical Fiber Communication Systems*. 1 ed. 1999: Artech House Publishers.

25. Headley, C. and G. Agrawal, *Raman Amplification in Fiber Optical Communication Systems*. 1 ed. 2004: Academic Press.

26. Agrawal, G.P., *Fiber-Optics Communication Systems*. 2 ed. 1997: Wiley-Interscience.

27. Agrawal, G.P., *Nonlinear Fiber Optics*. 4 ed. 2007: Academic Press.

28. Iannone, E., et al., *Nonlinear Optical Communication Networks*. 1 ed. 1998: Wiley-Interscience.

29. Arai, T., et al., *Photodarkening Phenomenon in Yb-Doped Fibers.* Fujikura Technical Review, 2009(38): p. 6-11.

30. Engholm, M., L. Norin, and D. Åberg, *Strong UV absorption and visible luminescence in ytterbium-doped aluminosilicate glass under UV excitation.* Opt. Lett., 2007. **32**(22): p. 3352-3354.

31. Koponen, J.J., et al., *Photodarkening in ytterbium-doped silica fibers*, in *Storage and Retrieval for Image and Video Databases*. 2005.

32. Shubin, A.V., et al. *Photodarkening of alumosilicate and phosphosilicate Yb-doped fibers*. in *Lasers and Electro-Optics, 2007 and the International Quantum Electronics Conference. CLEOE-IQEC 2007. European Conference on*. 2007.

33. Sławomir, M.K. and et al., *Optical study of Yb^{3+}/Yb^{2+} conversion in CaF 2 crystals.* Journal of Physics: Condensed Matter, 2005. **17**(25): p. 3771.

34. Laperle, P., et al., *Relations between phosphorus/aluminum concentration ratio and photodarkening rate and loss in Yb-doped silica fibers.* Proc. SPIE, 2010. **7580**.

35. Yao, N., *Focused Ion Beam Systems: Basics and Applications*. 2011: Cambridge University Press.

36. Sugiyama, M. and G. Sigesato, *A review of focused ion beam technology and its applications in transmission electron microscopy.* Journal of Electron Microscopy, 2004. **53**(5): p. 527-536.

37. Langford, R.M. and C. Clinton, *In situ lift-out using a FIB-SEM system.* Micron, 2004. **35**(7): p. 607-611.

38. Leica-microsystems. *http://www.leica-microsystems.com/*.

39. AlliedHighTech, *http://www.alliedhightech.com/grinding/polishsystem/*.

40. Williams, D.B. and C.B. Carter, *Transmission Electron Microscopy: A Textbook for Materials Science* 1ed. 2004: Springer.

41. Muller, D.A., *Structure and bonding at the atomic scale by scanning transmission electron microscopy.* Nat Mater, 2009. **8**(4): p. 263-270.

42. *Private Communication from M. Hajialamdari: Dept. of Physics and Astronomy, Guelph-Waterloo Physics Institute, University of Waterloo*.

43. Pan, L., I. Utkin, and R. Fedosejevs, *Two-wavelength ytterbium-doped fiber laser with sustained relaxation oscillation.* Appl. Opt., 2009. **48**(29): p. 5484-5489.

44. Fermann, M.E., et al., *Self-Similar Propagation and Amplification of Parabolic Pulses in Optical Fibers.* Physical Review Letters, 2000. **84**(26): p. 6010.

45. Fermann, M.E., et al., *Ultrawide tunable Er soliton fiber laser amplified in Yb-doped fiber.* Opt. Lett., 1999. **24**(20): p. 1428-1430.

46. Shibata, N., R. Braun, and R. Waarts, *Phase-mismatch dependence of efficiency of wave generation through four-wave mixing in a single-mode optical fiber.* Quantum Electronics, IEEE Journal of, 1987. **23**(7): p. 1205-1210.

47. Crewe, A.V., J. Wall, and J. Langmore, *Visibility of Single Atoms.* Science, 1970. **168**(3937): p. 1338-1340.

48. Voyles, P.M., et al., *Atomic-scale imaging of individual dopant atoms and clusters in highly n-type bulk Si.* Nature, 2002. **416**(6883): p. 826-829.

49. van Benthem, K., et al., *STEM imaging of single Pd atoms in activated carbon fibers considered for hydrogen storage.* Carbon, 2011. **49**(12): p. 4059-4063.

50. *Private Communication from Dr. M. Couillard, Dept. of Materials Science and Engineering, McMaster University*.

51. *Private Communication from Julia Huang: The Canadian Centre for Electron Microscopy, McMaster University*.

52. Bozzola, J.J. and L.D. Russell, *Electron Microscopy: Principles and Techniques for Biologists*. 1 ed. 1992: Jones & Bartlett Pub.

Appendix A

List of abbreviations in the thesis

ADF	annular dark-field
ASE	amplified spontaneous emission
BF	bright field
CCD	charge-coupled device
CCEM	Canadian Centre of Electron Microscopy
CIPI	Canadian Institute for Photonics Innovations
CT	charge-transfer
CW	continuous-wave
DFA	doped fiber amplifier
DF	dark field
DFM	difference-frequency mixing
EDFA	Erbium-doped fiber amplifier
EDS	energy-dispersive X-ray spectroscopy
ETU	energy transfer upconversion
FIB	focused ion beam
FWM	four-wave mixing
HAADF	high angle annular dark-field
HF	hydrogen fluoride
LMA	large mode area
MASE	modified amplified spontaneous emission
MIR	mid-infrared radiation
MSNR	modified signal to noise ratio
ODC	oxygen deficiency centers
PIPS	precision ion polishing system
POHC	phosphorus oxygen hole center
RE	rare earth
SBS	stimulated Brillouin scattering
SEM	scanning electron microscope
SNR	signal to noise ratio
SPM	self-phase modulation
SRS	stimulated Raman scattering
STEM	scanning transmission electron microscopy
TEM	transmission electron microscopy
XPM	cross-phase modulation
YDFA	Ytterbium-doped fiber amplifier

List of symbols in the thesis

$g(v)$	lineshape function
n	refractive index
τ	the excited state life time
σ_e	the absorption cross-section
σ_e	the emission cross section
A_{21}	the rate of spontaneous decay
N_1	the ground state populations
N_2	the excited state populations
A_{core}	the area of the fiber core
$A_{inner\ cladding}$	the area of inner cladding
N_T	ytterbium doping density in the fiber
$P_p(\lambda_j^p)$	the pump power of the *j*th pump channel
$P_s^+(\lambda_k^s)$	the signal power of *k*th signal channel propagating forward
$P_s^-(\lambda_k^s)$	the signal power of *k*th signal channel propagating backward
c	the speed of light in vacuum
α	the background attenuation coefficient of the fiber
τ	the fluorescence lifetime of the upper laser level
A	the doped effective area of the fiber
D	confinement factor of the pump beams in the doped area
Γ	confinement factor of the signal beams in the doped area
$P^+_{ASE}(\lambda_l^{ASE})$	the forward ASE power of the *l*th ASE channel
$P^-_{ASE}(\lambda_l^{ASE})$	the backward ASE power of the *l*th ASE channel
$\Delta\lambda$	the wavelength spacing between two ASE channels
L	the length of the entire fiber
h	Planck's constant
g_R	the Raman-gain coefficient
$P_{th(SRS)}$	the threshold power of Raman-gain
A_{eff}	the effective mode area
L_{eff}	the effective interaction length
g_B	the Brillouin gain coefficient
$P_{th(SBS)}$	the threshold power of Brillouin gain
n_0	the ordinary refractive index of the material
n_2	the nonlinear index coefficient
I	the optical intensity
P_0	the peak power of the incident pulse
γ	the nonlinear parameter for SPM and XPM
Φ	phase shift for SPM and XPM
η	the efficiency of the four-wave mixing
κ	the nonlinear interaction constant for FWM
χ_{1111}	the third-order nonlinear susceptibility
α_E	the photo-induced excess loss coefficient

β	the stretch-exponent
b	the power of the signal beam
L1	the length of the preamplifier
L2	the length of the second stage amplifier

Appendix B

Summary of benchmarks (validation) of the calculation

- **Single-fiber Amplifier System (double-clad fiber)**

❖ One-sided pumping

- This model is benchmarked with the simulation results from A. Budz [7]. The simulator used by A. Budz is verified by his experimental results. The results from two simulators are essentially identical which is expected as the codes follow the same algorithm and use the same cross section values. The relevant pages in this thesis are pp. 47-51.

- This software is also benchmarked with the simulator which is developed by M. Hajialamdari and verified by his experiments at the University of Waterloo [42]. The simulation results from the two simulators agree well within reasonable errors. The relevant pages in this thesis are pp. 56-57.

❖ Two-sided pumping

- The first verification method is to decrease one of the pump beams systematically to zero. The results are exactly the same as those obtained from the one-sided pumping model. The relevant page in this thesis is p. 65.

- This simulator is also benchmarked with the simulator developed by M. Hajialamdari [42]. The simulation results from two simulators agree well within reasonable errors. The relevant page in this thesis is p. 65.

- **Two-fiber Amplifier System**

  - The first verification method is to decrease one of the signal beams systematically to zero. The results are exactly the same as those in the one-sided pumping model. The relevant pages in this thesis are pp. 70-71.

  - The second method is to benchmark with the results which are from the simulator developed by M. Hajialamdari [42]. The simulation results from two simulators agree well within reasonable errors. The relevant page in this thesis is p. 71.

- **Two-stage Amplifier System**

- **Single-clad fiber**

  - This software is benchmarked with the simulation results from M. Hajialamdari, which are published in Ref. [1]. The simulation results from two simulators agree well within reasonable errors. The relevant pages in this thesis are pp. 78-79.

- **Two-stage system**

  - The performance of the simulator of two-stage system is verified by the simulation results published in Ref. [1] by M. Hajialamdari. The simulation results from two simulators with the same input parameters agree well within reasonable errors. The relevant pages in this thesis are pp. 78-79.

Appendix C

Conference and Meeting Contributions

Ran An, Hao Liu, Martin Couillard, Gianluigi Botton, Harold Haugen, "Ytterbium-doped fibre amplifiers: Computer modeling of amplifier systems and a preliminary electron microscopy study of single ytterbium atoms in doped optical fibres", *Canadian Institute for Photonics Innovations (CIPI) Annual Meeting*, Ottawa, Canada, May 2011

Hao Liu, Ran An, Martin Couillard, Gianluigi Botton, Harold Haugen, "Ytterbium-doped fibre amplifiers: Computer modeling of amplifier systems and a preliminary electron microscopy study of single ytterbium atoms in doped optical fibres", *7th International Workshop on Fibre Optics and Passive Components* , Montreal, Canada, June 2011